Chapter III.   Production, Structure and Decay of Light p-Shell Λ-Hypernuclei

Toshio MOTOBA, Hiroharu BANDŌ,* Kiyomi IKEDA**
and Taiichi YAMADA***

*Laboratory of Physics, Osaka Electro-Communication University
Neyagawa, Osaka 572*
**Division of Mathematical Physics, Fukui University, Fukui 910*
***Department of Physics, Niigata University, Niigata 950-21*
****Department of Applied Mathematics, Osaka University
Toyonaka, Osaka 560*

Contents

§ 1. Introduction

Recently structures of light hypernuclei attract particular interests, because the strangeness-exchange (K^-, π) reactions have been providing important information on excited states of Λ and Σ hypernuclei. In fact the (K^-, π) reaction experiments done at CERN,[1]~[7] Brookhaven[8]~[10] and KEK[11] offer new data such as excited state energies, production intensities and level widths for a number of hypernuclei. In a few cases even the hypernuclear γ-rays[7],[10] and pion angular distributions[9] have been observed. These experiments, in addition to the previous emulsion studies[12] giving the ground state energies, opened a gate to the 'hypernuclear spectroscopy' which is expected to disclose dynamical aspects of the hypernuclear structure.[5],[13]~[25] Accordingly the theoretical investigations are required to be leveled up, so that predictions of various physical quantities as well as explanations of the existing data can be made in neccessary details.

In this chapter we present the results of a systematic study of the light hypernuclei enclosed by the hatched boundary on the chart, Fig. 1, of the known hypernuclides. In these hypernuclei the cluster aspect is essentially important,[21]~[23] since the aspect is widely proved to be indispensable in describing the corresponding ordinary nuclei.[26],[27] From this point of view, in the previous papers,[21]~[23] we have investigated these hypernuclei by employing the *microscopic* three-cluster model. This line of our works is summarized and extended here to study the production, structure and decay of these hypernuclei.

The shell model is, of course, of fundamental importance as has been widely demon-
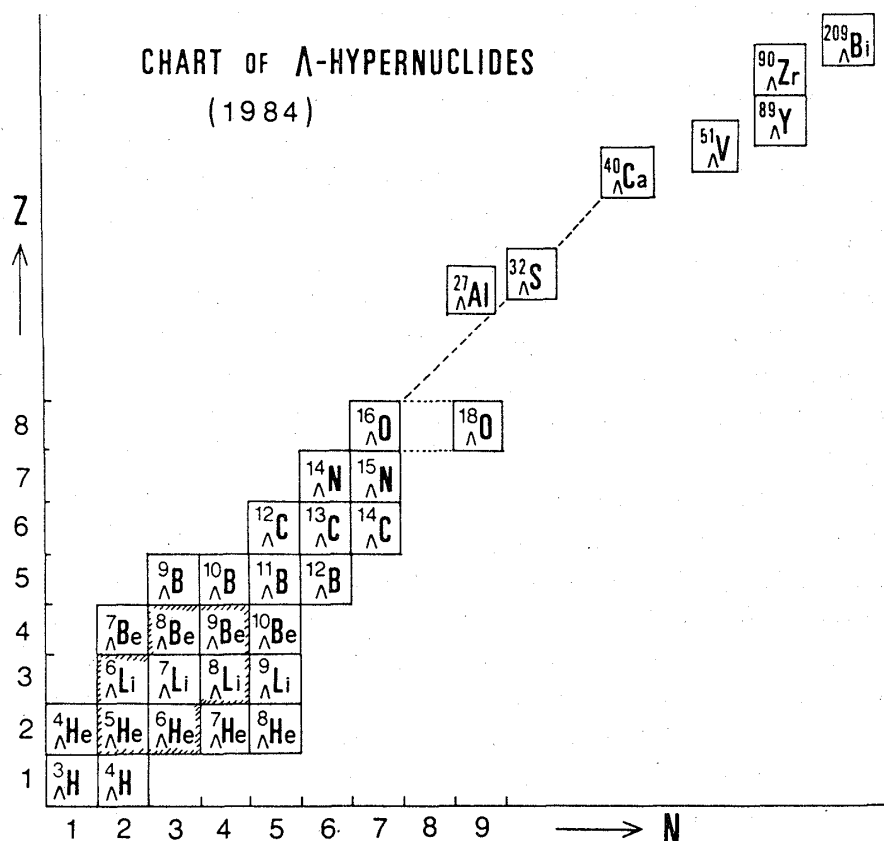

Fig. 1. Chart of the observed Λ-hypernuclides, in which those in the hatched region are concerned in this chapter. Based on the chart by Povh (1979),[6] the newly reported species have been added to complete this figure.

Table I.   Alpha and "x" clusters composing the light p-shell nuclei and Λ-hypernuclei. $S_x + S_\Lambda(1/2) = S$.

	"$\alpha + x$"	Spin(S_x)		"$\alpha + x + \Lambda$"	Spin(S)
^{5}He	$\alpha + n$	1/2	$^6_\Lambda$He	$\alpha + n + \Lambda$	0, 1
^{5}Li	$\alpha + p$	1/2	$^6_\Lambda$Li	$\alpha + p + \Lambda$	0, 1
^{6}Li	$\alpha + d$	1	$^7_\Lambda$Li	$\alpha + d + \Lambda$	1/2, 3/2
^{7}Li	$\alpha + t$	1/2	$^8_\Lambda$Li	$\alpha + t + \Lambda$	0, 1
^{7}Be	$\alpha + {}^3$He	1/2	$^8_\Lambda$Be	$\alpha + {}^3$He$+\Lambda$	0, 1
^{8}Be	$\alpha + \alpha$	0	$^9_\Lambda$Be	$\alpha + \alpha + \Lambda$	1/2
(^{9}Be	$\alpha + \alpha + n$	1/2)	($^5_\Lambda$He	$\alpha + \Lambda$	1/2)

strated in the systematic applications by Dalitz, Gal, Dover and collaborators.[14),17)~20),24),25)   An extended shell-model approach has been also applied to light hypernuclei by Žofka et al.[28),29)   Zhang et al.[30)] have performed the $SU(3)$ group classification for the $A = 9$–13 hypernuclear spectra.   On the other hand, for the ground state properties of light hypernuclei, Bodmer et al.[31)] have recently revived the cluster model[32)~34)] in which the constituents are treated as structureless particles.   The weak-coupling basis procedures are recently employed[35),36)] to treat the interplay between a Λ particle and the nuclear shell-model excitations.

We consider that the shell-model and cluster-model aspects are both crucially important to describe the light p-shell hypernuclei.[21),23)   The incorporation of the two ingredients can be achieved by the microscopic treatment for the three-cluster $(\alpha + x + \Lambda)$ systems listed in Table I ($x = n, p, d, t, {}^3$He or α).   In the present model the α and x clusters are treated to be composite and the antisymmetrization among all nucleons are properly taken into account.   The microscopic cluster model can describe both of well-developed cluster wave functions and important shell-model configurations without any spurious center-of-mass excitation.   This feature is desirable to the realistic estimates of physical quantities, since, for example, the (K^-, π^-) reaction populates the hypernuclear states up to rather high excitation energy.

With this model we make an extensive spectroscopic investigation with emphases on the structure characteristics, (K^-, π^-) production rates, electromagnetic transition rates, and the particle-decay and weak-decay properties.   We are also interested in the effect of using the realistic effective ΛN interaction based on the Nijmegen OBE model-D[37)] which is given in Chapter II.[38)]

In §2 the microscopic three-cluster model is formulated.   We treat a variety of states where the Λ particle and/or the core nucleus are allowed to be excited.   The channel-coupled secular equation is obtained and the cluster-model expressions are given for the physical observables.   In §3 the calculated results for the $^9_\Lambda$Be case are presented and discussed as a typical example among the hypernuclei concerned.   In the last part the results with the realistic ΛN interaction are compared with those of the one-range Gaussian interaction adopted throughout the chapter.   The calculated results for the other hypernuclei, $^8_\Lambda$Li($^8_\Lambda$Be), $^7_\Lambda$Li and $^6_\Lambda$He($^6_\Lambda$Li), are presented in this order in the subsections of §4.   In §5 are described the expression and the estimates of the π-mesic decay rates.   Section 6 is devoted to an advanced treatment for the resonance-peak widths in the ^{9}Be(K^-, π^-)$^9_\Lambda$Be reaction.   The channel-coupled scattering equation is solved and the mechanism of the 'high'-lying resonance is explained.   In §7 the main results of this

chapter are summarized.

§ 2.   The microscopic $\alpha + x + \Lambda$ three-cluster model

2. 1.   *Model wave function and equation of motion*

For the microscopic description of low-lying states of light p-shell nuclei, the $\alpha + x$ two-cluster model works well within the framework of the generator coordinate method (GCM).[39),40)]   The wave function (wf) with the α-x orbital angular momentum l and spin S_x is expressed by

$$\alpha + x : \quad \Psi_{lj}^{\alpha x} = |\overset{\circ}{\varPhi}_j{}^{\alpha x}(l) S_x{:}j\rangle = \sum_d f_{lj}(d)|\varPhi(l; d) S_x; j\rangle, \tag{2·1}$$

where $j = l + S_x$ and $f_{lj}(d)$ is the GCM amplitude and $\varPhi(l; d)$ the GCM basis wf,

$$\varPhi(l; d) = \frac{1}{\sqrt{1+\delta_{ax}}} \sqrt{\frac{4!x!}{(4+x)!}} \mathcal{A}'\{\phi_\alpha\phi_x\varphi_l(r; d) Y_l(\hat{r})\}, \tag{2·2}$$

$$\varphi_l(r; d) = 4\pi(\sqrt{\pi}b_r)^{-3/2}\exp[-(r^2+d^2)/2b_r^2]\mathscr{J}_l(rd/b_r^2), \tag{2·3}$$

$$b_r = \sqrt{(4+x)/4x}\, b_N, \quad b_N = \sqrt{\hbar/M_N\Omega}\,. \tag{2·4}$$

Here $\phi_\alpha(\phi_x)$ represents the internal wf of $\alpha(x)$ cluster with h.o. $(0s)^4$ $((0s)^x)$ configuration. The operator $\mathcal{A}'$ in Eq. (2·2) antisymmetrizes the nucleons belonging to different clusters. The generator coordinate d in the wave packet $\varphi_l(r; d)$ specifies the α-x distance, and the $\mathscr{J}_l(z)$ in Eq. (2·3) is the spherical Bessel function with an imaginary argument. The amplitudes $f_{lj}(d)$ in Eq. (2·1) are given as the solutions of the GCM equation

$$\sum_{d_2}\{H_{lj}^{\alpha x}(d_1, d_2) - EN_l^{\alpha x}(d_1, d_2)\}f_{lj}(d_2) = 0, \tag{2·5}$$

where the energy and normalization kernels are defined by

$$\left.\begin{array}{l} H_{lj}^{\alpha x}(d_1, d_2) \\ N_l^{\alpha x}(d_1, d_2) \end{array}\right\} = \langle[\varPhi(l; d_1)S_x];j|\left\{\begin{array}{c} H^{\alpha x} \\ 1 \end{array}\right\}|[\varPhi(l; d_2)S_x]; j\rangle. \tag{2·6}$$

Now adding a Λ particle to the $\alpha + x$ nucleus and choosing the coordinate system shown in Fig. 2(b), the model wf of the hypernucleus can be expanded as

$$\alpha + x + \Lambda : \quad \Psi_J = \sum_c \sum_{dK} w_c(d, K)|[\varPhi(l; d) \times u_{K\lambda}(\boldsymbol{R})]_L[S_x S_\Lambda]_S; J\rangle, \tag{2·7}$$

where $c = \{l, \lambda, L, S\}$ denotes a channel of the angular momentum coupling, with λ referring to the (ax)-Λ coordinate.   The relevant spins with the coupling $S_x + S_\Lambda = S$ are listed in Table I.   The relative wf between the Λ particle and the center-of-mass of $\alpha + x$ nucleus is spanned by the normalized harmonic oscillator (h.o.) basis with the size parameter b_R:

$$u_{K\lambda}(\boldsymbol{R}) = u_{K\lambda}(R) Y_\lambda(\hat{\boldsymbol{R}}), \quad K = 2\nu + \lambda, \quad (K = \text{number of h.o. quanta}) \tag{2·8}$$

$$b_R = \sqrt{\{(4+x)M_N + M_\Lambda\}/(4+x)M_\Lambda}\, b_N\,. \tag{2·9}$$

The b_r and b_R are chosen to facilitate Moshinski transformations into different Jacobi coordinates.

The total Hamiltonian of the $a+x+\Lambda$ system includes, in addition to the $(4+x)$-nucleon part H^{ax}, the ΛN interaction $V_{\Lambda N}$ and the kinetic energy T_R associated with the (ax)-Λ relative coordinate $\boldsymbol{R}$:

$$\mathcal{H} = H^{ax} + T_R + V_{\Lambda N}, \quad V_{\Lambda N} = \sum_{i=1}^{4+x} v_{\Lambda N}(\Lambda, i). \tag{2·10}$$

Starting from the Schrödinger equation $\mathcal{H}\Psi_J = E\Psi_J$, we can obtain the channel-coupled seqular equation for the coefficient $w_c(d, K)$ of Ψ_J,

$$\sum_{c_2 d_2 K_2} \left\{ \delta(l_1, l_2)\delta(K_1\lambda_1, K_2\lambda_2) \sum_{j_x j_\Lambda} \begin{bmatrix} l_1 & \lambda_1 & L_1 \\ S_x & S_\Lambda & S_1 \\ j_x & j_\Lambda & J \end{bmatrix} \begin{bmatrix} l_2 & \lambda_2 & L_2 \\ S_x & S_\Lambda & S_2 \\ j_x & j_\Lambda & J \end{bmatrix} H^{ax}_{l_1 j_x}(d_1, d_2) \right.$$

$$+ \delta(c_1, c_2)T^R_{\lambda_1}(K_1, K_2)N^{ax}_{l_1}(d_1, d_2) + \delta(L_1 S_1, L_2 S_2)U^{\Lambda N}_J(c_1 d_1 K_1, c_2 d_2 K_2)$$

$$\left. - \delta(c_1, c_2)\delta(K_1\lambda_1, K_2\lambda_2)E_J N^{ax}_{l_1}(d_1, d_2)\right\}w_{c_2}(d_2, K_2) = 0. \tag{2·11}$$

Here the matrix elements of T_R and $V_{\Lambda N}$ are defined by

$$T_\lambda^R(K_1, K_2) = \langle u_{K_1\lambda}(\boldsymbol{R})| T_R | u_{K_2\lambda}(\boldsymbol{R})\rangle \tag{2·12}$$

and

$$U_J^{\Lambda N}(c_1 d_1 K_1, c_2 d_2 K_2)$$

$$= \langle [\Phi(l_1; d_1) \times u_{K_1\lambda_1}(\boldsymbol{R})]_{L_1}[S_x S_\Lambda]_{S_1}; J | V_{\Lambda N}|[\Phi(l_2; d_2) \times u_{K_2\lambda_2}(\boldsymbol{R})]_{L_2}[S_x S_\Lambda]_{S_2}; J\rangle, \tag{2·13a}$$

$$= \delta(L_1, L_2)\delta(S_1, S_2)\langle u_{K_1\lambda_1}(R)| U_{L_1 S_1}(l_1\lambda_1 d_1, l_2\lambda_2 d_2; R)|u_{K_2\lambda_2}(R)\rangle. \tag{2·13b}$$
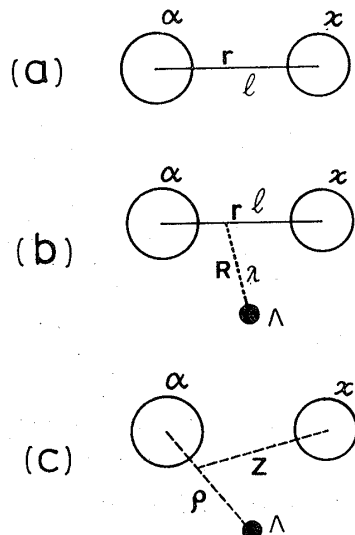
Fig. 2. Coordinate systems for (a) the nuclear two clusters and (b) the hypernuclear three-cluster system where $x = n, p, d, t,$ ^{3}He or α. (c) The coordinate used to describe the rearrangement channel leading to $^5_\Lambda$He-x decay.

In Eq. (2·11) the total orbital angular momentum L and spin S of the $a+x+\Lambda$ system are not individually conserved due to the presence of the spin-orbit potential in H^{ax}, while $j_x = l + S_x$ and $j_\Lambda = \lambda + S_\Lambda$ are also not conserved due to the ΛN spin-spin interaction.

The motion of the Λ particle is determined by a sort of the folding potential $U^{\Lambda N}$ of Eq. (2·13) supplied by the $a+x$ core nucleus. On the other hand the Λ particle plays a glue-like role to give additional couplings between a and x clusters through the ΛN interaction matrix element $U^{\Lambda N}$. The explicit expression of $U_{LS}(l_1\lambda_1 d_1, l_2\lambda_2 d_2; R)$ for the Gaussian type of ΛN interaction is given in Ref. 23).

2.2. Hamiltonian and the adopted model space

2.2.1. The orthogonality condition model for the nuclear part

For the a-x part we employ the orthogonality condition model (OCM)[40),41)] which has been proved to be a good approximation of the GCM. By the OCM approximation we can take into account the essential effect of the Pauli principle arising from the nucleon antisymmetrization. In general the GCM basis function $\Phi(l; d)$ of Eq. (2·2) can be expanded in terms of the normalized-antisymmetrized h.o. basis functions $\widehat{\Phi}^{ax}(Nl)$ of the a-x system:

$$\Phi(l; d) = \sum_N \sqrt{\mu_N} C_{Nl}(d; b_r) \widehat{\Phi}^{ax}(Nl), \tag{2·14}$$

$$\widehat{\Phi}^{ax}(Nl) = \frac{1}{\sqrt{1+\delta_{ax}}} \sqrt{\frac{4!x!}{(4+x)!}} \frac{1}{\sqrt{\mu_N}} \mathcal{A}'\{\phi_a \phi_x u_{Nl}(\boldsymbol{r})\}, \tag{2·15a}$$

$$u_{Nl}(\boldsymbol{r}) = u_{Nl}(r) Y_l(\widehat{\boldsymbol{r}}), \tag{2·15b}$$

where $u_{Nl}(r)$ is the h.o. wf with the size b_r and quanta $N = 2n+l$, and

$$C_{Nl}(d; b_r) = 4\pi(-)^n \pi^{-1/4} 2^{-3/2} \left[\Gamma\left(n+l+\frac{3}{2}\right)\Gamma(n+1)\right]^{-1/2} (d/b_r)^N e^{-(d/b_r)^2}. \tag{2·16}$$

The coefficient μ_N is the eigenvalue of the normalization kernel defined by

$$\frac{1}{1+\delta_{ax}}\langle\phi_a \phi_x|\mathcal{A}'\{\phi_a \phi_x u_{Nl}(\boldsymbol{r})\}\rangle = \mu_N u_{Nl}(\boldsymbol{r}), \tag{2·17a}$$

and is obtained as

$$\mu_N = \mu_N(x) = \frac{1}{1+\delta_{ax}}\sum_{m=0}^{x}\frac{x!}{(x-m)!m!}(-)^m\left(1-\frac{4+x}{4x}m\right)^N. \tag{2·17b}$$

The values are listed in Table II.

For the calculation of various physical quantities, it is convenient to reexpress the hypernuclear wf Ψ_J by using the a-x h.o. basis $\{\widehat{\Phi}^{ax}(Nl)\}$ given by Eq. (2·15):

Table II. Eigenvalues μ_N of normalization kernels for $a+x$ systems. See Eq. (2·17) for the definition.

$N(\hbar\omega)$	$a+n(p)$	$a+d$	$a+t(^3\text{He})$	$a+a$
$N = 0$	0	0	0	0
1	1.25	0	0	0
2	0.9375	1.125	0	0
3	1.0156	0.8438	1.1910	0
4	0.9961	1.0547	0.5955	0.75
5	1.0010	0.9668	1.1992	0
6	0.9998	1.0151	0.8064	0.9375
7	1.0001	0.9921	1.1269	0
8	0.9999	1.0039	0.8972	0.9844
9	1.0000	0.9980	1.0739	0
10	1.0000	1.0010	0.9432	0.9961
$\vdots$	$\vdots$	$\vdots$	$\vdots$	$\vdots$
	1.0	1.0	1.0	1.0

$$a+x+\Lambda(\text{h.o.}): \quad \Psi_J = \sum_{cNK} A_c(N,K) | [\hat{\Phi}^{ax}(Nl) \times u_{K\lambda}(\boldsymbol{R})]_L [S_x S_\Lambda]_S; J\rangle, \qquad (2\cdot18)$$

where the expansion coefficients $A_c(N,K)$ are related to the original $w_c(d,K)$'s by

$$A_c(N,K) = \sqrt{\mu_N} \sum_d C_{Nl}(d; b_r) w_c(d,K). \qquad (2\cdot19)$$

The GCM normalization kernel defined by Eq. (2·6) is expressed by the expansion:

$$N_l^{ax}(d_1, d_2) = \sum_N \mu_N C_{Nl}(d_1; b_r) C_{Nl}(d_2; b_r). \qquad (2\cdot20)$$

For the GCM energy kernel we make the OCM approximation[39] to put

$$\langle \hat{\Phi}^{ax}(N_1 l) S_x; j | H^{ax} | \hat{\Phi}^{ax}(N_2 l) S_x; j \rangle \to \langle u_{N_1 l} S_x; j | H_{\text{OCM}}^{ax} | u_{N_2 l} S_x; j \rangle, \qquad (2\cdot21)$$

and we get

$$H_{lj}^{ax}(d_1, d_2) = \sum_{N_1 N_2} \sqrt{\mu_{N_1} \mu_{N_2}} C_{N_1 l}(d_1, b_r) C_{N_2 l}(d_2, b_r) \langle u_{N_1 l} S_x; j | H_{\text{OCM}}^{ax} | u_{N_2 l} S_x; j \rangle. \qquad (2\cdot22)$$

Here the OCM effective Hamiltonian H_{OCM}^{ax} consists of the relative kinetic energy, central, spin-orbit and Coulomb potentials between the a and x clusters,

$$H_{\text{OCM}}^{ax} = T_r + V_{\text{C}}(r) + V_{\text{LS}}(r) + V_{\text{Coul}}(r). \qquad (2\cdot23)$$

For $V_{\text{C}}(r)$ and $V_{\text{LS}}(r)$ we employ the Gaussian type effective potentials,

$$V_{\text{C}}(r) = V_{\text{C}}^0 e^{-(r/\beta_{\text{C}})^2}, \qquad (2\cdot24)$$

$$V_{\text{LS}}(r) = V_{\text{LS}}^0 e^{-(r/\beta_{\text{LS}})^2}(\boldsymbol{l}\cdot\boldsymbol{s}), \qquad (2\cdot25)$$

of which the strengths and ranges are determined so as to reproduce the observed low-lying properties of the corresponding nucleus.[*] The used parameters are summarized in Table III. The Coulomb folding potential is given by

$$V_{\text{Coul}}(r) = \frac{Z_1 Z_2 e^2}{r^2} \text{erf}(r/\tilde{b}), \quad \tilde{b} = \sqrt{2 - \frac{4+x}{4x}} \, b_{\text{N}}, \qquad (2\cdot26)$$

where $Z_1 = 2$ for a and Z_2 is the number of protons in the x cluster and $\text{erf}(\rho)$ denotes the error function.

The nuclear wf is obtained by solving the $a+x$ two-cluster problem ($x \leq 4$) with H_{OCM}^{ax}

Table III. Parameters of the central and spin-orbit effective nuclear potentials between the alpha and x clusters. The a-a strength is from Ref. 42). ($a = 1/\beta^2$)

"a-x"	V_{C}^0	β_{C}	(a_{C})	V_{LS}^0	β_{LS}	(a_{LS})
	MeV	fm		MeV	fm	
a-$n(p)$	−43.0	2.236	(0.20)	−27.5	2.375	(0.18)
a-d	−74.0[a]	2.294	(0.19)	−0.15[b]	4.082	(0.06)
a-t	−81.0	2.500	(0.16)	−3.0	1.890	(0.28)
a-^{3}He	−81.0	2.500	(0.16)	−3.0	1.890	(0.28)
a-a	−106.2	2.236	(0.20)	—	—	—

a) $V_{\text{C}}^0 = -78.4$ MeV for the $l=2$ state.

b) For this strength see the footnote on this page.

[*] For the ^{6}Li case this form is modified as $V_{\text{LS}}(r) = \bar{V}_{\text{LS}}^0 r^2 e^{(-r/\beta_{\text{LS}})^2}(\boldsymbol{l}\cdot\boldsymbol{s})$.

Table IV. Harmonic oscillator expansion of the α-x ground state wave functions. See Eqs. (2·27) and (2·28) for the definition of the coefficient a_N and Eq. (2·15) for the di-cluster h.o. basis except for the α-Λ case. Note that $N = 2n + l$. The α-x relative energies and α-x root-mean-square distances are listed.

$l(j^\pi)$	α-$n(p)$ 1(3/2$^-$)	α-d 0(1$^+$)	α-t(^{3}He) 1(3/2$^-$)		α-α 0(0$^+$)	α-Λ 0(1/2$^+$)	
E^{exp}	0.89(1.96)	-1.47	-2.47	(-1.59)	0.09	-3.12	[MeV]
E	1.13	-1.43	-2.41	(-1.51)	0.37	-3.11	[MeV]
$\sqrt{\langle r^2 \rangle_{a-x}}$	4.12	3.80	3.51	(3.73)	4.09	2.69	[fm]
$n = 0$	0.799	*	*	(*)	*	0.917	
1	-0.369	-0.743	-0.696	(-0.682)	*	-0.251	
2	0.317	0.420	0.472	(0.474)	0.569	0.232	
3	-0.230	-0.335	-0.357	(-0.363)	-0.448	-0.132	
4	0.185	0.252	0.266	(0.273)	0.394	0.107	
5	-0.148	-0.192	-0.199	(-0.206)	-0.332	-0.075	
6	0.105	0.152	0.151	(0.159)	0.274	0.060	
7	-0.064	-0.124	-0.117	(-0.124)	-0.225	-0.045	
$\vdots$	$\vdots$	$\vdots$	$\vdots$	$\vdots$	$\vdots$	$\vdots$	

*) Forbidden states.

and can be expressed in terms of the h.o. basis of Eq. (2·15),

$$\alpha + x (\mathrm{h.o.}): \quad \Psi_{lj}^{ax} = \sum_N a_N^{(lj)} | \hat{\Phi}^{ax}(Nl) S_x; j \rangle, \tag{2·27}$$

$$a_N^{(lj)} = \sum_d f_{lj}(d) C_{Nl}(d; b_r). \tag{2·28}$$

The calculated expansion coefficients $a_N^{(lj)}$ for the $a + x$ ground states are listed in Table IV.

2.2.2. The ΛN interaction

Throughout this paper except §3.5, we employ a one-range Gaussian ΛN interaction ("ORG")

$$\mathrm{ORG}: \quad v_{\Lambda N}(r) = v_{\Lambda N}^0 e^{-(r/\beta_{\Lambda N})^2}(1 + \eta \boldsymbol{\sigma}_\Lambda \cdot \boldsymbol{\sigma}_N),$$

$$v_{\Lambda N}^0 = -38.19 \text{ MeV}, \quad \beta_{\Lambda N} = 1.034 \text{ fm}, \quad \eta = -0.1, \tag{2·29}$$

where the range $\beta_{\Lambda N}$ is equivalent to the two-pion exchange Yukawa. This strength $v_{\Lambda N}^0$ was determined[32] so as to reproduce the experimental Λ-binding energy in $^5_\Lambda$He(B_Λ^{exp} $= 3.12$ MeV)[43] by using the α-Λ folding potential obtained with $\phi_\alpha(b_N = 1.358$ fm) (cf. §3.5). The value of η is chosen by considering the suggestions in the literature.[5),16),43)] The LS interaction is not considered here because the Λ single particle spin-orbit potential has been found to be very weak.[1)]

In §3.5, we test the effect of using the realistic effective ΛN interaction "YNG(ΛN)" in the $^5_\Lambda$He and $^9_\Lambda$Be cases. This interaction derived on the basis of the Nijmegen OBE Model-D[37] simulates the G-matrices by the three-range Gaussian form with the dependence on the nuclear Fermi momentum k_F:

$$\mathrm{YNG}(\Lambda N): \quad v_{\Lambda N}^{lS\mathcal{G}}(r; k_F) = \sum_{i=1}^{3} (a_i + b_i k_F + c_i k_F^2) e^{-(r/\beta_i)^2},$$

$$\beta_i = 0.5, \ 0.9, \ 1.5 \text{ fm}. \tag{2·30}$$

The necessary parameters are given in §3.5.   See Chapter II for the details.[38]

2. 2. 3.   The adopted model space

As mentioned in §2.1, our model space is described by the channels of possible angular momentum couplings $c=\{l\lambda LS\}$, the $a\text{-}x$ generator coordinate d and the $(ax)\text{-}\Lambda$ h.o. quanta $K=2\nu+\lambda$.   In the present calculation, the inter-cluster states are restricted to the following space:

(I) the $a\text{-}x$ orbital $l=1$ and 3 for $^{6}_{\Lambda}$He, $^{6,8}_{\Lambda}$Li and $^{8}_{\Lambda}$Be;

$$l=0 \text{ and } 2 \ (0, 2 \text{ and } 4) \text{ for } ^{7}_{\Lambda}\text{Li } (^{9}_{\Lambda}\text{Be}),$$

(II) the GCM mesh points: $d=1.0$, 2.25, 3.5, 5.0 and 6.5 fm,

(III) the $(ax)\text{-}\Lambda$ h.o. quanta $K=2\nu+\lambda$ with $0\leqq\nu\leqq9$ and $0\leqq\lambda\leqq3$ (or 4).

Note that the properties of the low-lying states of the $a+x$ nuclear systems[44] can be satisfactorily described within the model space of (I) and (II), as will be shown in Figs. 5, 16, 17 and 20.   See Table IV for the $a\text{-}x$ ground state wf's.

2. 3. (K^{-}, π^{-}) reaction cross section

Within the framework of the distorted wave impulse approximation (DWIA), the (K^{-}, π^{-}) reaction cross section is related to the elementary $K^{-}n\to\Lambda\pi^{-}$ cross section as[15),16),45),46)]

$$\frac{d\sigma_{if}(\theta)}{d\Omega}\bigg|^{\text{Lab}} = N_{\text{eff}}(i\to f;\ \theta)\frac{d\sigma(\theta)}{d\Omega}\bigg|^{\text{Lab}}_{K^{-}n\to\Lambda\pi^{-}}. \tag{2.31}$$

The effective neutron number $N_{\text{eff}}\ (i\to f;\ \theta)$ is given by

$$N_{\text{eff}}(i\to f;\ \theta)=\frac{1}{[J_i]}\sum_{M_f M_i}\left|\langle f|\int d^3r\ \chi^{(-)*}_{p_\pi}(r)\chi^{(+)}_{p_K}(r)\sum_{k=1}^{A} U_{-}(k)\delta(r-r_k)|i\rangle\right|^2, \tag{2.32a}$$

$$=\frac{4\pi}{[J_i]}\sum_{\kappa\mu}\left|\langle J_f T_f \tau_f\|\sum_k U_{-}(k)\ \tilde{j}_{\kappa\mu}(p_K, p_\pi, \theta;\ r_k)\ Y_\kappa(\hat{r}_k)\|J_i T_i \tau_i\rangle\right|^2. \tag{2.32b}$$

Here the U-spin lowering operator U_{-} transforms a neutron into a Λ-particle.   The function $\tilde{j}_{\kappa\mu}(p_K, p_\pi, \theta;\ r_k)$ is related with the partial wave expansion of the distorted waves of the K^{-} and π^{-} mesons,

$$\chi^{(-)*}_{p_\pi}(r)\chi^{(+)}_{p_K}(r)=\sum_{\kappa\mu}\sqrt{4\pi[\kappa]}\ i^\kappa \tilde{j}_{\kappa\mu}(p_K, p_\pi, \theta;\ r)\ Y_{\kappa\mu}(\hat{r}), \tag{2.33}$$

where K^{-} beam direction is chosen as the z-axis.   The meson distorted waves χ are evaluated by using the eikonal approximation with the π^{-}-nucleus and K^{-}-nucleus optical potentials.

Now we derive the expression of N_{eff} for the reaction $[a+(x+1)]$ (K^{-}, π^{-}) $[a+x+\Lambda]$ on the basis of our microscopic cluster model.   As for the ground state of ^{9}Be (target nucleus for $x=4$), we use the wf calculated by Okabe et al.[47] in the framework of the microscopic $a+a+n$ three-cluster model.   The other target wf's $\Psi^{ax_1}_{L_1J_1}$ are obtained by solving the $a+x_1$ two-cluster problem$(x_1=x+1)$ and are given in the form of Eq. (2.27). With the aid of the overlap relation corresponding to the change of Jacobi coordinates, i.e.,

$$\sqrt{5+x} \left\langle [\hat{\Phi}^{\alpha x}_{T_f \tau_f}(N'l') Y_{\lambda_i}(\hat{R})]_{L_i} \left[S_x \times \frac{1}{2} \right]_{S_i} \middle| \hat{\Phi}^{\alpha x_1}_{T_i \tau_i}(N_i L_i) S_i \right\rangle$$

$$= \omega_x(T_i \tau_i S_i; T_f \tau_f S_x) \Omega_x(N_i L_i; N'l', K_i \lambda_i) u_{K_i \lambda_i}(R) \left| \frac{1}{2}, \tau_i - \tau_f \right\rangle ,$$

$$(K_i = N_i - N') \tag{2.34}$$

the $\alpha + (x+1)$ target wf in Eq. (2.32b) can be effectively expressed as

$$\Psi^{\alpha x_1}_{J_i T_i \tau_i} = \sum_{N_i} a^{(L_i J_i)}_{N_i} \sum_{N'l'K_i\lambda_i} \omega_x(T_i \tau_i S_i; T_f \tau_f S_x) \Omega_x(N_i L_i; N'l', K_i \lambda_i)$$

$$\times \left| [\hat{\Phi}^{\alpha x}_{T_f \tau_f}(N'l') \times u_{K_i \lambda_i}(R)]_{L_i} \left[S_x \times \frac{1}{2} \right]_{S_i}; J_i \right\rangle . \tag{2.35}$$

The coefficients ω_x and Ω_x are given as follows:

$$\omega_x(T_i \tau_i S_i; T_f \tau_f S_f) = \begin{cases} 1 & \text{for } x = 1 \ (^6\text{Li}; \, ^6_\Lambda\text{Li}), \\ \sqrt{3/2} & \text{for } x = 2 \ (^7\text{Li}; \, ^7_\Lambda\text{Li}), \\ 1 & \text{for } x = 4 \ (^9\text{Be}; \, ^9_\Lambda\text{Be}), \end{cases} \tag{2.36}$$

$$\Omega_x(N_i L_i; N'l', K_i \lambda_i) = \sqrt{5+x} \langle [\hat{\Phi}^{\alpha x}(N'l') \times u_{K_i \lambda_i}(R)]_{L_i} | \hat{\Phi}^{\alpha x_1}(N_i L_i) \rangle . \tag{2.37}$$

Note that the wf of ^{9}Be target is provided in the form of $\alpha + \alpha + n$. Using the target nuclear wf, Eq. (2.35), and the final state hypernuclear wf given by Eq. (2.18), we can get the cluster-model expression for N_{eff}:

$$N_{\text{eff}}(J_i T_i \tau_i \to J_f T_f \tau_f; \theta) = \frac{1}{[J_i]} \omega_x(T_i \tau_i S_i; T_f \tau_f S_x)^2 \sum_{\kappa\mu} |\mathcal{M}_{\kappa\mu}(J_i, J_f)|^2, \tag{2.38}$$

$$\mathcal{M}_{\kappa\mu}(J_i, J_f) = \sum_{C_f N_f K_f C_i N_i K_i} A_{c_f}(N_f, K_f) a^{(L_i J_i)}_{N_i} \delta(S_f, S_x) \sqrt{[J_f][J_i][L_f][L_i][\lambda_i][x]}$$

$$\times W(L_f S_f \kappa J_i; J_f L_i) W(l_f \lambda_i L_f \kappa; L_i \lambda_f)(\lambda_i 0 x 0 | \lambda_f 0) \Omega(N_i L_i; N_f l_f, K_i \lambda_i)$$

$$\times \langle u_{K_f \lambda_f}(R) \| \tilde{j}_{\kappa\mu} \left(p_K, p_\pi, \theta; \frac{4+x}{5+x} R \right) \| u_{K_i \lambda_i}(R) \rangle , \tag{2.39}$$

$$K_i = N_i - N_f . \quad (N_i = 2n_i + L_i, \ N_f = 2n_f + l_f, \ K_i = 2\nu_i + \lambda_i)$$

The total effective neutron number $N^{\text{tot}}_{\text{eff}}(\theta = 0^\circ)$ is defined by a sum of all final hypernuclear state contributions, while it is simply derived from Eq.(2.32a) under the closure approximation as

$$N^{\text{tot}}_{\text{eff}}(\theta = 0^\circ) = \int \rho_n(r) A(r) 4\pi r^2 dr , \tag{2.40a}$$

$$A(r) = \frac{1}{4\pi} \int |\chi^{(-)*}_{p_\pi}(r) \chi^{(+)}_{p_K}(r)|^2 d\Omega , \tag{2.40b}$$

where $\rho_n(r)$ is the neutron density of the target nucleus and is calculated with our cluster model wf. Figure 3 shows the calculated $\rho_n(r)$ and $A(r)$ for the considered nuclei.

As the differential cross section for the free space $K^- n \to \Lambda \pi^-$ process in Eq. (2.31), the empirical values taken from the analysis by Gopal et al.[48] are used in the actual evaluation of the (K^-, π^-) reaction cross sections.

2.4. *Electromagnetic transition operators*

In the formulae given in this subsection, $a(x)$ cluster is generally represented as the mass number $A_1(A_2)$ nucleus with $Z_1(Z_2)$ protons ($A_1=4$, $Z_1=2$, $A_2=x$).

——Electric quadrupole and dipole transitions——

For the nuclei in which the spatial wf within a cluster is symmetrical under any exchange of the constituent protons and neutrons, the electric quadrupole operator can be effectively expressed as ($e_p=e$, $e_n=0$):

$$\mathcal{M}(E2) = \sum_{protons} e\hat{q}(r_i)$$

$$= \frac{Z_1 e}{A_1} \sum_{i=1}^{A_1} \hat{q}(r_i) + \frac{Z_2 e}{A_2} \sum_{i=A_1+1}^{A_1+A_2} \hat{q}(r_i)$$

$$= \mathcal{M}(E2)_A + \mathcal{M}(E2)_c + X , \qquad (2\cdot41a)$$

$$\mathcal{M}(E2)_A = (Z_1 + Z_2) e\xi^2 \hat{q}(R), \qquad (2\cdot41b)$$

$$\mathcal{M}(E2)_c = \frac{Z_1 A_2{}^2 + Z_2 A_1{}^2}{(A_1+A_2)^2} e\hat{q}(r)$$

$$+ e\hat{Q}_{A_1}^{(int)} + e\hat{Q}_{A_2}^{(int)}, \qquad (2\cdot41c)$$

Fig. 3. Calculated neutron densities $\rho_n(r)$ and the radial dependence of the function $A(r)$ of Eq. (2·40b) which represents meson absorption.

where $\hat{q}(r) = r^2 Y_2(\hat{r})$ is the mass quadrupole operator and $\hat{Q}_A^{(int)}$ is the quadrupole operator for the internal coordinates of a cluster. See Fig. 2(b) for the coordinates R and r. The X term in Eq.(2·41a) contains a factor proportional to $R\cdot r$, which has no contribution within the present model space. The factor ξ in Eq. (2·41b) originates from the condition of the center-of-mass rest of the total three-cluster system ($A_1+A_2+\Lambda$) and is given by

$$\xi = M_\Lambda / \{(A_1+A_2)M_N + M_\Lambda\}. \qquad (2\cdot42)$$

Under the similar condition the electric dipole operator can be written as

$$\mathcal{M}(E1) = \sum_{protons} e\hat{m}(r_i) = \mathcal{M}(E1)_A + \mathcal{M}(E1)_c , \qquad (2\cdot43a)$$

$$\mathcal{M}(E1)_A = -(Z_1 + Z_2) e\xi \hat{m}(R), \qquad (2\cdot43b)$$

$$\mathcal{M}(E1)_c = -\frac{Z_1 A_2 - Z_2 A_1}{A_1 + A_2} e\hat{m}(r), \qquad (2\cdot43c)$$

where $\hat{m}(r) = r Y_1(\hat{r})$ is the dipole operator. One can recognize from Eqs.(2·42) and (2·43b) that in the E1 transition the Λ particle behaves as if it carries an effective charge

$$\tilde{e}_\Lambda^{(E1)} = -(Z_1 + Z_2) M_\Lambda e / \{(A_1+A_2)M_N + M_\Lambda\}. \qquad (2\cdot44)$$

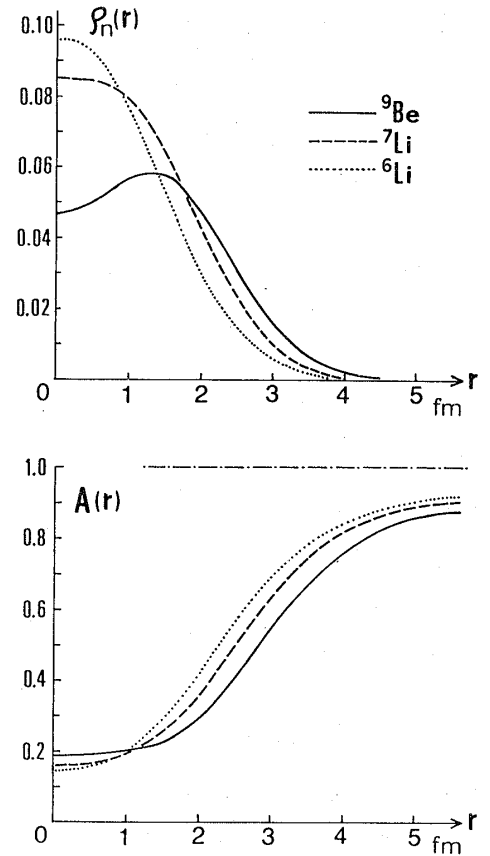This is due to the recoil of the core nucleus and the situation is similar to the case of the

neutron E1 effective charge $\tilde{e}_n{}^{(E1)} = -Ze/A$. The $\mathscr{M}(E2)_A$ of Eq.(2·41b) is similarly interpreted. If the relation $Z_1/A_1 = Z_2/A_2$ holds, then the core nucleus part $\mathscr{M}(E1)_c$ given by Eq. (2·43c) vanishes as a natural consequence.

The reduced E$\mathscr{L}$($\mathscr{L}=2$ or 1) transition probability can be obtained in the standard way by using the initial and final state wf's expressed by Eq. (2·18):

$$B(E\mathscr{L}; J_i \to J_f) = \frac{1}{[J_i]}|\langle \Psi_{J_f}\|\mathscr{M}(E\mathscr{L})\|\Psi_{J_i}\rangle|^2, \quad [J] \equiv 2J+1. \tag{2·45}$$

—— Magnetic dipole transitions and moments ——

The magnetic dipole operator consists of the orbital and spin parts:

$$\mathscr{M}(M1) = \sum_{i=1}^{5+x}\sqrt{\frac{3}{4\pi}}(g_l{}^{(i)}\boldsymbol{l}_i + g_s{}^{(i)}\boldsymbol{s}_i) = \sum_i^{4+x}\sqrt{\frac{3}{4\pi}}g_l{}^{(i)}\boldsymbol{l}_i + \mathscr{M}(M1)_s^{qx} + \mathscr{M}(M1)_s^A, \tag{2·46}$$

where the sum runs over all the constituent particles and g's are relevant g-factors. The standard (bare) values of g-factors are employed here (nm=nuclear magneton):

$$g_l{}^{(i)} = \begin{cases} 1 \text{ nm}, \\ 0 \quad, \\ 0 \quad, \end{cases} \qquad g_s{}^{(i)} = \begin{cases} 5.586 \text{ nm}, & (i=p) \\ -3.826 \quad, & (\quad n) \\ -1.228 \quad. & (\quad \Lambda) \end{cases} \tag{2·47}$$

The spin part is easy to handle with and especially its matrix element for the spin$=0$ cluster (α) vanishes.

The orbital part should be expressed in terms of the relative and internal coordinates of the clusters. Under the condition that the spatial wf of a cluster is symmetric for the constituent protons and neutrons, we can rewrite the operator by using the relative $\boldsymbol{l}$ and $\boldsymbol{\lambda}$ and the internal $\bar{\boldsymbol{L}}_{A_1}^{(\text{int})}$ and $\bar{\boldsymbol{L}}_{A_2}^{(\text{int})}$,

$$\sum_{i=1}^{A_1+A_2+A} g_l{}^{(i)}\boldsymbol{l}_i = \frac{Z_1 g_l{}^{(p)} + N_1 g_l{}^{(n)}}{A_1}\sum_{i=1}^{A_1}(\boldsymbol{r}_i \times \boldsymbol{p}_i)$$

$$+ \frac{Z_2 g_l{}^{(p)} + N_2 g_l{}^{(n)}}{A_2}\sum_{i=A_1+1}^{A_1+A_2}(\boldsymbol{r}_i \times \boldsymbol{p}_i) + g_l{}^{(\Lambda)}(\boldsymbol{r}_\Lambda \times \boldsymbol{p}_\Lambda)$$

$$= \mathscr{M}(M1)_l^{qx} + \mathscr{M}(M1)_\lambda^A + \frac{Z_1 g_l{}^{(p)}}{A_1}\bar{\boldsymbol{L}}_{A_1}^{(\text{int})} + \frac{Z_2 g_l{}^{(p)}}{A_2}\bar{\boldsymbol{L}}_{A_2}^{(\text{int})} + Y, \tag{2·48a}$$

$$\mathscr{M}(M1)_l^{qx} = \frac{Z_1 A_2{}^2 + Z_2 A_1{}^2}{A_1 A_2(A_1+A_2)}\boldsymbol{l}, \tag{2·48b}$$

$$\mathscr{M}(M1)_\lambda^A = \frac{Z_1 + Z_2}{A_1 + A_2}\xi\boldsymbol{\lambda}, \tag{2·48c}$$

where the Y term contains the mixed products of the coordinate and non-conjugate momentum such as $\boldsymbol{R} \times \boldsymbol{p}_r$ and $\boldsymbol{r} \times \boldsymbol{P}_R$, and this doubly parity-changing term is inactive within the model space adopted in the present calculation. Furthermore the two $\bar{\boldsymbol{L}}^{(\text{int})}$ - terms have no contributions for the s-shell clusters as in the present case.

From the above consideration we regard the operator $\mathscr{M}(M1)$ for the $\alpha + x + \Lambda$ system as consisting of four parts: $\mathscr{M}(M1)_l^{qx}$, $\mathscr{M}(M1)_\lambda^A$, $\mathscr{M}(M1)_s^{qx}$ and $\mathscr{M}(M1)_s^A$ for which the notations should be self-evident. Then the reduced M1 transition probability and moment can be obtained straightforwardly.

2. 5. *Particle-decay rates based on reduced width amplitudes*

Widths of resonance levels in the hypernuclei under consideration are attributed largely to particle-decays into two clusters. On the basis of the separation energy method,[49] the partial decay width Γ_c of a state is related to the relevant reduced width amplitude (RWA), $\mathcal{Y}_L$, with L being the channel angular momentum:

$$\Gamma_c = 2P_L(a)\,\theta_L{}^2(a)\,\gamma_W{}^2(a), \tag{2·49a}$$

$$\theta_L{}^2(a) = \frac{a}{3}\mathcal{Y}_L{}^2(a), \quad \gamma_W{}^2(a) = \frac{3\hbar^2}{2\mu a^2}, \tag{2·49b}$$

where the penetration factor P_L and the reduced width $\theta_L{}^2$ in units of the Wigner limit $\gamma_W{}^2$ are evaluated at an appropriate channel radius a. The behavior of RWA itself is an important quantity reflecting the characteristics of wf. Here we consider two kinds of RWA's leading to the i) (ax)-Λ and ii) $^5_\Lambda$He-x channels. The former corresponds to the separation process and the latter the break-up one. The a-$(x\Lambda)$ type RWA will be also calculated for the $^8_\Lambda$Li $\rightarrow a + ^4_\Lambda$H channel.

—— (ax)-Λ channel ——

The RWA for this channel is defined and expressed by

$$\mathcal{Y}^{ax\text{-}\Lambda}_{lj_x\text{-}\lambda j_\Lambda}(R) \equiv R\langle[\mathring{\varPhi}_{j_x}(l)S_x]_{j_x}[Y_\lambda(\hat{\boldsymbol{R}})S_\Lambda]_{j_\Lambda};J\,|\,\varPsi_J\rangle, \tag{2·50a}$$

$$= \sum_N a_N{}^{(lj_x)} \sum_{LSK} \begin{bmatrix} l & S_x & j_x \\ \lambda & S_\Lambda & j_\Lambda \\ L & S & J \end{bmatrix} A_c(N,K)\,u_{K\lambda}(R;b_R), \tag{2·50b}$$

where the square bracket is the normalized 9-j symbol and $A_c(N,K)$ is given by Eq. (2·19). Recall that $u_{K\lambda}(R;b_R)$ is the h.o. wf with the size parameter b_R. The a_N's are the expansion coefficients of the free a-x wf $|\mathring{\varPhi}_{j_x}(l)S_x;j_x\rangle$ with respect to the normalized-antisymmetrized h.o. basis $|\widehat{\varPhi}^{ax}(Nl)S_x;j_x\rangle$ defined by Eqs. (2·27) and (2·28). The values of $\{a_N\}$ are listed in Table IV.

—— $^5_\Lambda$He-x channel ——

By choosing the inter-cluster Jacobi coordinates ρ and Z illustrated in Fig. 2(c), the RWA for the $^5_\Lambda$He$(1/2^+)$-x channel is defined by

$$\mathcal{Y}^{aA\text{-}x}_{Lj_x}(Z) = \sqrt{\frac{(4+x)!}{4!x!}}\,Z\langle\phi[^5_\Lambda\mathrm{He}(1/2^+)][\phi_x Y_L(\hat{\boldsymbol{Z}})S_x]_{j_x};J\,|\,\varPsi_J\rangle, \tag{2·51}*)$$

where the ground state wf of $^5_\Lambda$He is given by the s-state a-Λ wf $\xi_0(\rho)$ as

$$\phi[^5_\Lambda\mathrm{He}(1/2^+{}_{\mathrm{g.s.}})] = \phi_a\xi_0(\rho)[Y_0(\hat{\boldsymbol{\rho}})S_\Lambda]_{1/2}. \tag{2·52}$$

We expand the $\xi_0(\rho)$ in terms of the h.o. wf $u_{N0}(\rho;b_\rho)$ with the appropriate size parameter b_ρ which assures the common oscillator constant $(\mu_\rho b_\rho{}^2 = M_N b_N{}^2 = \hbar/\Omega)$,

$$\xi_0(\rho) = \sum_N \tilde{a}_N u_{N0}(\rho;b_\rho), \quad b_\rho = \sqrt{(4M_N + M_\Lambda)/4M_\Lambda}\,b_N. \tag{2·53}$$

The coefficients $\tilde{a}_N$ are listed in the 6-th column of Table IV. Note that they are obtained by solving the a-Λ problem with the ΛN interaction described in §2.2.2. With the j_x-j_Λ

---

*) For the decay $^9_\Lambda$Be $\rightarrow ^5_\Lambda$He $+ a$, the normalization is corrected from that of Eq. (3·25) in Ref. 23).

to L-S recoupling and the transformation of the three-particle Jacobi coordinates, the RWA can be expressed in terms of the h.o. wf pertinent to the ${}^5_\Lambda$He-x relative coordinate Z. The spectroscopic factor is defined by the norm of the corresponding RWA as

$$S^2 = \int_0^\infty \mathcal{Y}^2(R)\, dR \,. \tag{2·54}$$

§ 3. Results and discussion on ${}^9_\Lambda$Be as a typical example

3.1. *Energy spectra and structure characteristics*

The calculated energy spectra of ${}^9_\Lambda$Be and dominant components of their wf's are shown in Figs. 4 and 5 where the calculated ^{8}Be spectrum is also displayed. Here the energy levels are labeled by the orbital angular momentum L^π instead of the degenerate doublet $J = L \pm 1/2$. Note that the $\sigma_\Lambda \cdot \sigma_N$ part of the ΛN interaction is inactive in this system with spin-saturated $\alpha + \alpha$ core, and each level is degenerate for the Λ-spin up and down. The energy levels are found to be classified into three characteristic bands according to the underlying intrinsic structures. The positive parity states constitute the ground state rotational band:

$$L^\pi = 0^+, 2^+ \text{ and } 4^+, \quad (J = L \pm 1/2; \quad K^\pi = 0^+, \text{ “ }{}^8\text{Be-analog”})$$
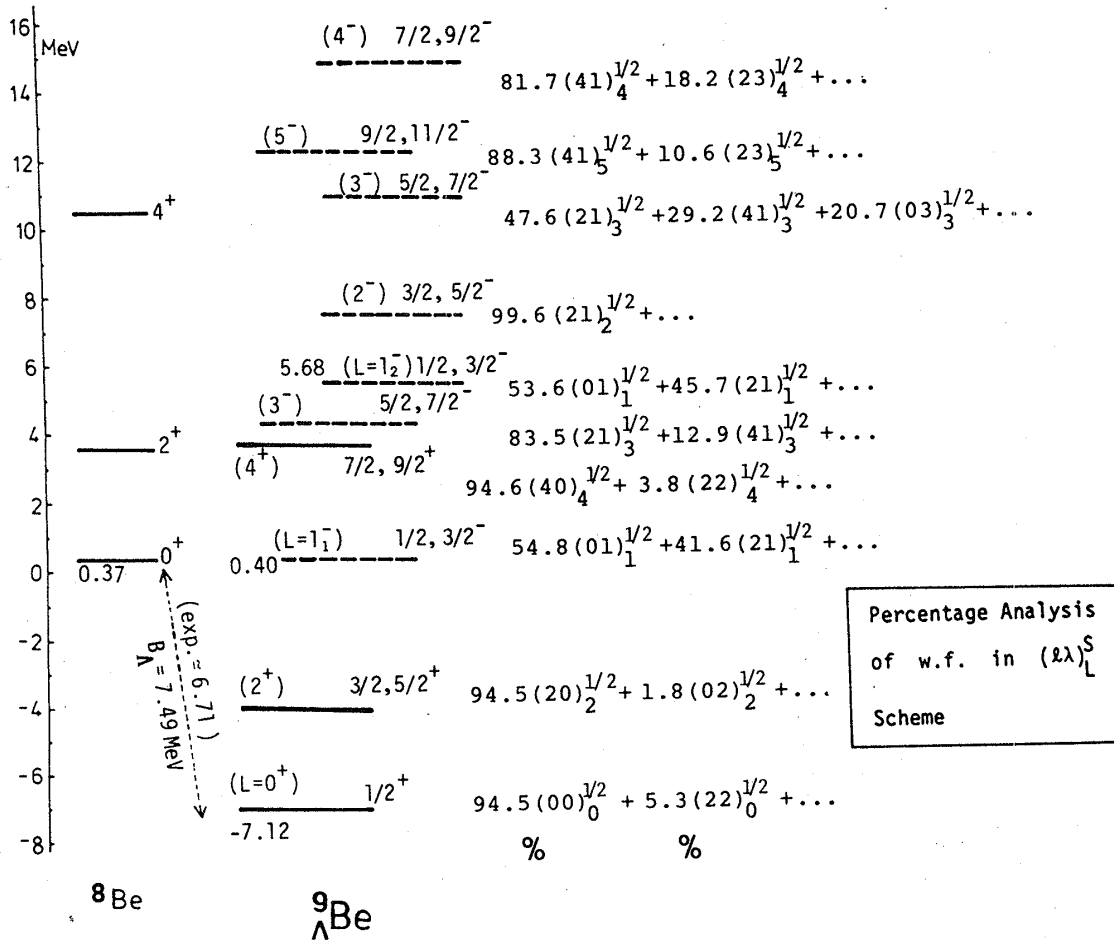

Fig. 4. Calculated energy spectra of ^{8}Be and ${}^9_\Lambda$Be. The energy scale is the relative binding energy among the constituent clusters. The dominant components of the L-S coupling ${}^9_\Lambda$Be wave functions are given in %.

to which we can naturally assign the intrinsic orbital quantum number $K^\pi = 0^+$. This band is quite analogous to the rotational band of ^{8}Be as seen in Fig. 5. So we call this band as "^{8}Be-analog band". In fact this feature can be clearly seen in the obtained wf's expressed in the L-S coupling (cf. Fig. 4):

$$|1/2^+(L=0 \text{ g.s.})\rangle = 94.5\,\%\,(l=0, \lambda=0)_{L=0}^{S=1/2} + 5.3\,\%\,(2,2)_0^{1/2} + \cdots, \tag{3.1}$$

$$|3/2^+, 5/2^+(L=2)\rangle = 94.5\,\%\,(l=2, \lambda=0)_{L=2}^{S=1/2} + 1.8\,\%\,(0,2)_2^{1/2} + \cdots, \tag{3.2}$$

$$|7/2^+, 9/2^+(L=4)\rangle = 94.6\,\%\,(l=4, \lambda=0)_{L=4}^{S=1/2} + 3.8\,\%\,(2,2)_4^{1/2} + \cdots. \tag{3.3}$$

Thus each rotational member can be well described with a single configuration

$$[(\alpha\alpha)_l \times s_{1/2}^\Lambda], \quad l = 0^+, 2^+ \text{ and } 4^+,$$
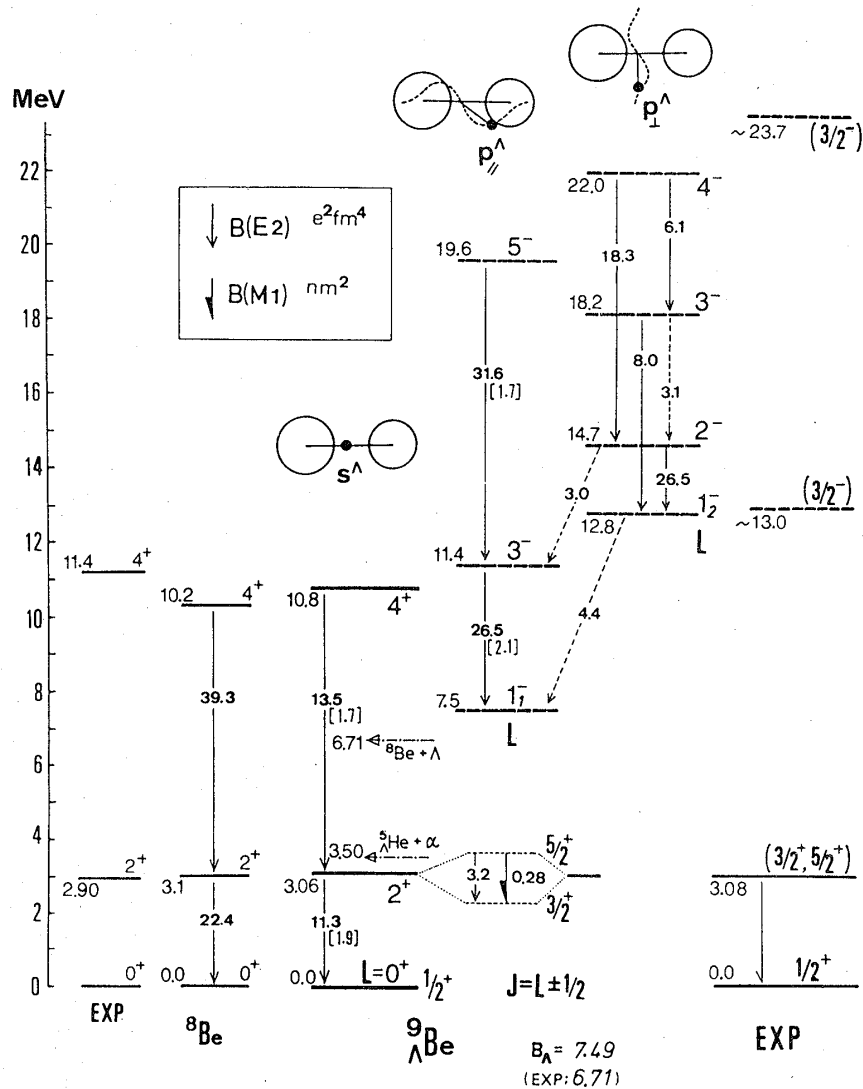
Fig. 5. Reduced E2 and M1 transition probabilities calculated for ^{8}Be and $^9_\Lambda$Be. The levels of $^9_\Lambda$Be are assigned orbital angular momentum L^π instead of the degenerate $J = L \pm 1/2$, hence the $B(\text{E2}; L \to L')$ are listed in this figure except the case $5/2^+ \to 3/2^+$. The $B(\text{E2})$ values less than the Weisskopf estimate($1.1\,e^2/\text{fm}^4$) are not shown. In the square brackets are the shell-model limit values described in the text. The experimental threshold energies are indicated in the $^9_\Lambda$Be spectrum. The observed energies of ^{8}Be are from Ref. 44) and those of $^9_\Lambda$Be from Refs. 4), 10) and 43).

Table V. Harmonic oscillator expansions of the Λ-particle wave functions $\chi_\lambda{}^\Lambda(R)$ in the dominant channel of some typical states. The channel is expressed by $(l\lambda)_L{}^S$ with its occupancy (%) in the total hypernuclear wf. Entries are $a_{K\lambda}^2$ of $\chi_\lambda{}^\Lambda(R)=\Sigma_K a_{K\lambda} u_{K\lambda}(R)$ where $K=2\nu+\lambda$ and $0\leq\nu\leq9$. Negligibly small numbers are represented by dots.

	${}^9_\Lambda\text{Be}$			${}^8_\Lambda\text{Li}({}^8_\Lambda\text{Be})$		${}^7_\Lambda\text{Li}$		${}^6_\Lambda\text{He}({}^6_\Lambda\text{Li})$	
J^π	$1/2^+$	$3/2_1^-$	$3/2_2^-$	1^-	0^+	$1/2^+$	$3/2^-$	1^-	0^+
E[MeV]	-7.12	0.40	5.68	-9.18	-2.27	-7.09	1.88	-2.84	4.95
$(l\lambda)_L{}^S$	$(00)_0^{1/2}$	$(01)_1^{1/2}$	$(01)_1^{1/2}$	$(10)_1^0$	$(11)_0^0$	$(00)_0^{1/2}$	$(01)_1^{1/2}$	$(10)_1^0$	$(11)_0^0$
[%]	94.5	54.9	53.6	88.9	97.9	98.5	84.9	68.8	75.9
χ^Λ	s^Λ	p^Λ	p^Λ	s^Λ	p^Λ	s^Λ	p^Λ	s^Λ	p^Λ
$\nu=0$	.838	.547	.085	.861	.588	.870	.331	.854	.277
1	.113	.226	.145	.091	.203	.076	.198	.073	.189
2	.031	.102	.185	.030	.009	.034	.156	.044	.167
3	:	.057	.179	:	.053	:	.116	:	.130
4	:	.033	.153	:	.030	:	.088	:	.097
5	:	:	.114	:	:	:	.055	:	.066

where the Λ particle occupies the s-state ($\lambda=0$) with respect to the center of ^{8}Be. Correspondingly the cluster-model illustration for the intrinsic structure is shown above the band in Fig. 5.

It is noted that, for example, the Λ particle wf normalized within the ground state dominant channel has the following h.o. components with the size parameter b_R defined by Eq. (2·9):

$$|s^\Lambda\rangle = 83.8\,\%\,|u_{0s}\rangle + 11.3\,\%\,|u_{1s}\rangle + 3.1\,\%\,|u_{2s}\rangle + \cdots. \qquad (3\cdot4)$$

In Table V one can see the similar expressions of the typical Λ wf's.

On the other hand, the negative parity states in which the Λ particle occupies mainly the p-state ($\lambda=1$) split into two bands,

(i) $L=1^-, 3^-$ and 5^- $(J=L\pm1/2: K^\pi=0^-$ band $(p_{/\!/}))$,

(ii) $L=1^-, 2^-, 3^-$ and 4^- $(J=L\pm1/2: K^\pi=1^-$ band$(p_\perp)$,"^{9}Be-analog").

The weak coupling basis function $[(\alpha\alpha)_l \times \Lambda]$ are largely distributed into these two band states. As shown in Fig. 4, for example, the two 1^- wf's are obtained as

$$|1/2^-, 3/2^-(L=1_1^-)\rangle = 54.8\,\%\,(l=0, \lambda=1)_{L=1}^{S=1/2} + 41.6\,\%\,(2,1)_1^{1/2} + \cdots, \qquad (3\cdot5)$$

$$|1/2^-, 3/2^-(L=1_2^-)\rangle = 53.6\,\%\,(l=0, \lambda=1)_{L=1}^{S=1/2} + 45.7\,\%\,(2,1)_1^{1/2} + \cdots. \qquad (3\cdot6)$$

Note here that the relative sign between the first two configurations in Eq. (3·6) is opposite to that of Eq. (3·5), although only the squared amplitudes are listed to show our GCM wf's. This feature allows one to take the strong coupling picture for these negative parity states. This picture is further confirmed by comparing these wf's with the following shell model correspondents of the ideal strong coupling limit in which they are labeled by the $SU(3)$ classification $(\lambda\mu)=(50)$ and (31), respectively.

$$|(50)^{SU(3)}; L=1^-\rangle = \sqrt{7/15}(l=0, \lambda=1)_{L=1} + \sqrt{8/15}(2,1)_1, \qquad (3\cdot7)$$

$$|(31)^{SU(3)}; L=1^-\rangle = -\sqrt{8/15}(l=0, \lambda=1)_{L=1} + \sqrt{7/15}(2,1)_1. \qquad (3\cdot8)$$
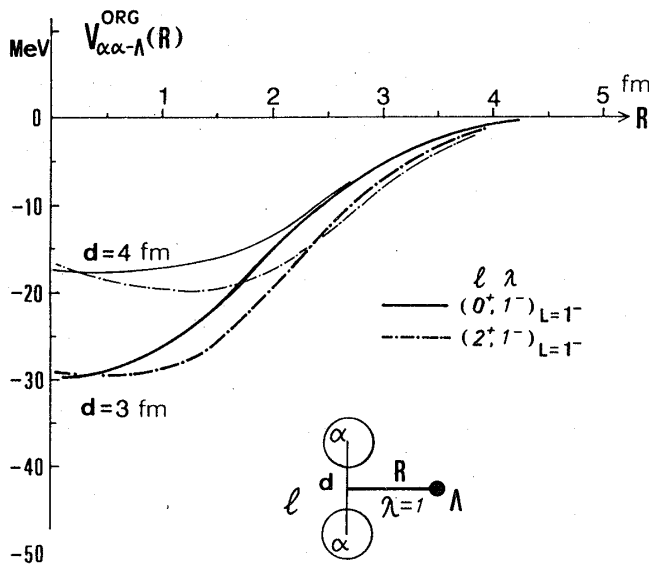
Fig. 6. Examples of the folding potentials $U_{LS}(l_1\lambda_1 d_1, l_2\lambda_2 d_2; R)$ between $^8\mathrm{Be}(l) = \alpha + \alpha$ and the Λ particle are shown as a function of the relative distance R. For the definition see Eq. (2·13b) where for $L=1$ $(S=1/2)$ we adopt $(l_1, \lambda_1) = (l_2, \lambda_2) = (0, 1)$ and $(2, 1)$ cases with the appropriate α-α distance parameter $d_1 = d_2 = 3.0$ and 4.0 fm.

In the present case the large stable deformation (prolate) due to the α-α clustering in $^8\mathrm{Be}$ enhances the realization of the picture. The two band structures are also confirmed by the strong intra-band and weak inter-band $B(\mathrm{E2})$ values estimated with the obtained wf's (cf. Fig. 5).

Correspondingly to the two negative parity bands, the cluster-model illustrations of their intrinsic structures are depicted above the respective bands. They are characterized by the two Λ particle p-states($\lambda=1$) which are parallel($p_{/\!/}$) and perpendicular $(p_\perp)$ to the deformation axis, respectively. It is noted that our $K = 1^-$ band having the $p_\perp$-structure closely resembles the ground band of $^9\mathrm{Be}$, except the sizable spin-orbit splittings in the latter.[44] Thus this band may be called as the "$^9\mathrm{Be}$-analog band". The $3/2^-$ member of this band can be reached by a simple substitution of the Λ particle for the last odd neutron in $^9\mathrm{Be}(3/2^-_{\mathrm{g.s.}})$. The big peak observed at $B_\Lambda{}^{\mathrm{exp}} = -6.3$ MeV[4] is, therefore, identified as our $3/2_2{}^-(L=1_2{}^-)$ level ($B_\Lambda = -5.31$ MeV) as will be discussed in §3.2.

The $K = 0^-$ band has the $p_{/\!/}$-type intrinsic structure in which the Λ particle occupies the same orbital space as that of the maximum symmetric nucleons in the α cluster. It is interesting to note that this band has no correspondent in ordinary nuclei and is "genuinely hypernuclear" because the $p_{/\!/}$-orbit is allowed for Λ but not for a nucleon due to the Pauli exclusion principle. In the shell-model limit our $K=0^-$ wf tends to the configuration with an $SU(3)$ classification[30] $[f](\lambda\mu) = [54](50)$ which was called "supersymmetric" by Dalitz and Gal.[19]

Although there is no bound state in the $^8\mathrm{Be}$ nucleus, we get three particle-stable bound states, $J = 1/2^+(\mathrm{g.s.})$, $3/2^+$-$5/2^+(3.06$ MeV$)$, due to the participation of a Λ particle. The calculated binding energy of the Λ in the ground state of $^9_\Lambda\mathrm{Be}$ is a little overestimated in comparison with the observed one:

$$^9_\Lambda\mathrm{Be}(1/2^+_{\mathrm{g.s.}}): \quad B_\Lambda{}^{\mathrm{cal}} = 7.49 \text{ MeV} \quad \text{vs.} \quad B_\Lambda{}^{\mathrm{exp}} = 6.71 \text{ MeV.}[43]$$

The present result showing the $3/2^+$-$5/2^+$ degeneracy is different from the shell model prediction by Dalitz and Gal.[18] New data of γ-rays in $^9_\Lambda\mathrm{Be}$ observed recently by May et al.[10b] supports our prediction:[23]

$$3/2^+\text{-}5/2^+ \quad \text{at} \quad E^{\mathrm{cal}} = 3.06 \text{ MeV} \quad \text{vs.} \quad E_\gamma{}^{\mathrm{exp}} = 3.079 \pm 0.040 \text{ MeV.}[10b]$$

Table V lists the h.o. expansion of the typical Λ particle wf's in each dominant angular momentum channel. One can see that the s-state Λ-particle wf generally concentrates on the lowest two h.o. states, while the p-state wf is scattered over several h.o. states

with the components depending on the level energy.

3.2. *Production rates through the* (K^-, π^-) *reaction*

Table VI lists the calculated effective neutron numbers $N_{eff}(\theta=0°)$ for the $^9Be(K^-, \pi^-)^9_\Lambda Be$ reactions with $p_K=720$ MeV/c.[1)~5)] Based on the empirical cross section $d\sigma(0°)/d\Omega \simeq 3.7$ mb/sr[48)] for the elementary process $K^-n \to \Lambda\pi^-$, the excitation spectra $d\sigma(\theta)/d\Omega$ of the production reaction are estimated at several scattering angles. The observed feature of the ground state small peak and two big peaks ($B_\Lambda^{exp}=-6.3$ MeV and -17 MeV)[4)] are well explained with our $L=0^+$ and $L=1^-$ spectra ($\theta=0°$) in Fig. 7. Thus the $K=1^-$ band head 1_2^- ($J=3/2^-$) state obtained at 12.8 MeV excitation (experimentally

Table VI. Calculated effective neutron numbers $N_{eff}(\theta=0°)$ for the (K^-, π^-) reactions with $p_K=720$ MeV/c. Pure imaginary optical potentials for K^- and π^- are used with $\sigma_{KN}=\sigma_{\pi N}=30$ mb.

$^9_\Lambda Be$		$^7_\Lambda Li$		$^6_\Lambda Li$	
$L^\pi(J)$	$N_{eff}(0°)$	J^π	$N_{eff}(0°)$	J^π	$N_{eff}(0°)$
$0^+(1/2^+)$	0.002	$1/2^+$	0.01	1^-	0.002
2^+	0.002	$3/2^+$	0.000	2^-	0.01
1_1^-	0.01	$5/2^+$	0.01	1^-	0.004
3^-	0.002	$3/2_1^-$ *	0.89	0^-	0.001
$1_2^-(3/2_2^-)$ *	0.35	$1/2^-$	0.004	1_1^+ *	0.41
2^-	0.07	$3/2_2^-$	0.01	2^+	0.001
				3^+	0.01
$(3/2^-)$ *	1.24[a)]	$(3/2^-)$ *	0.58[a)]	(1^+) *	0.65[a)]
$N_{eff}^{total}(0°)$	2.18		1.75		1.41

The levels marked by asterisks correspond to the observed big peaks.[3),4)] a) Estimates with the molecular orbital model.[50)]
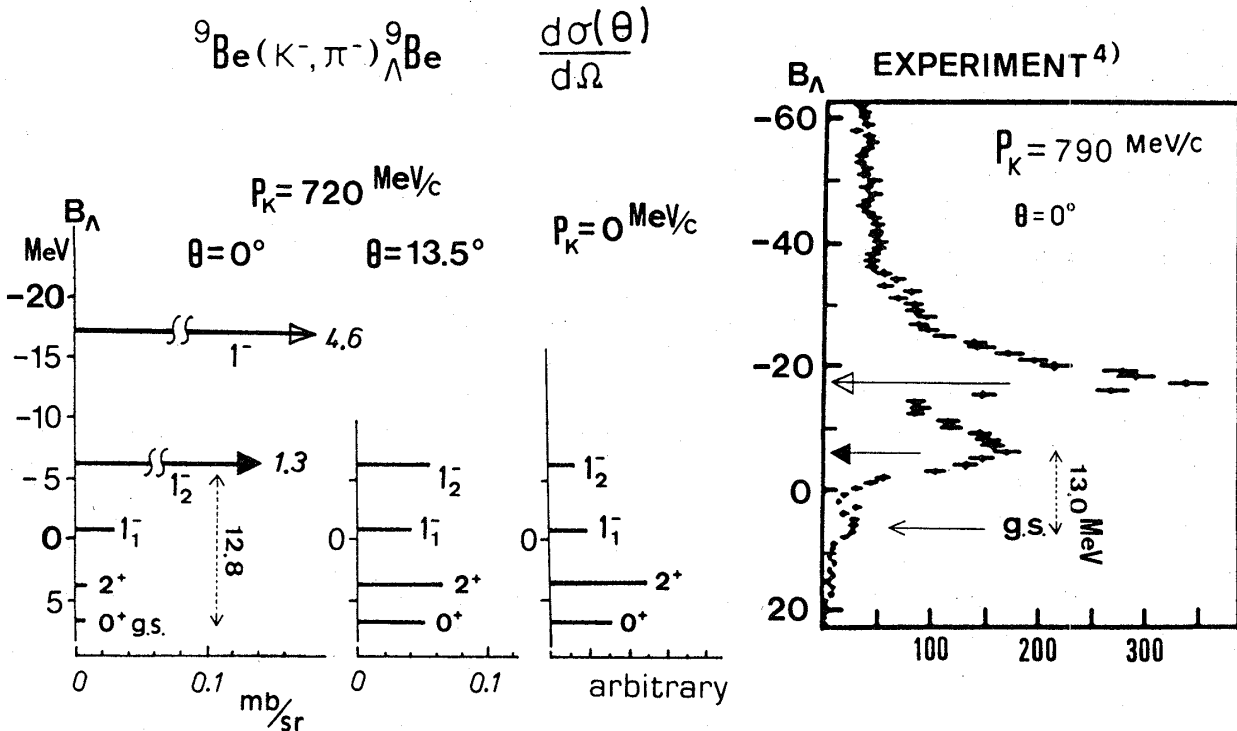

Fig. 7. Calculated excitation spectra $d\sigma(\theta)/d\Omega$ of the $^9Be(K^-, \pi^-)^9_\Lambda Be$ reactions with $p_K=720$ MeV/c ($\theta=0°$ & 13.5°) and $p_K=0$. The final states are assigned with $L^\pi(J=L\pm1/2)$. The $\theta=0°$ observed spectrum[4)] is compared.

$$\frac{d\sigma(\theta)}{d\Omega}$$

$^{9}\text{Be}(\text{K}^{-}, \pi^{-})^{9}_{\Lambda}\text{Be}$
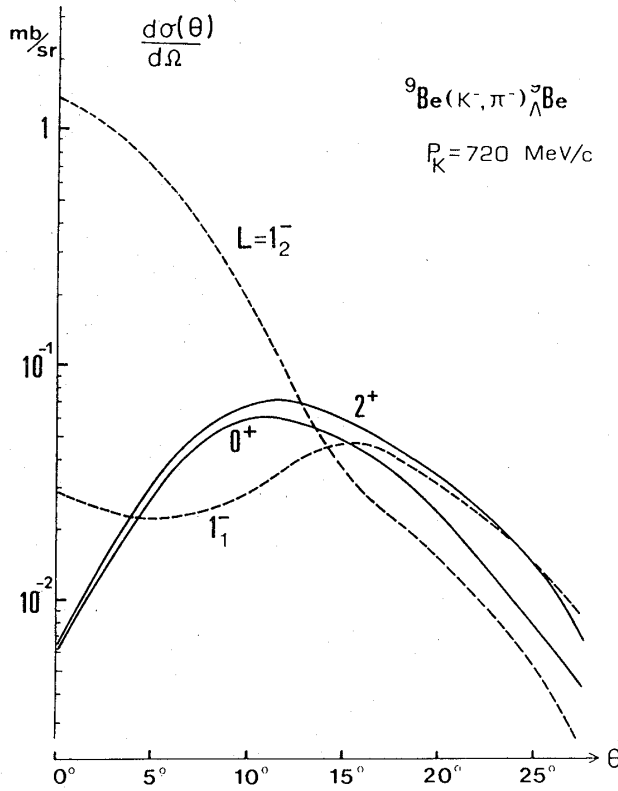
$P_{K} = 720$ MeV/c

Fig. 8. Calculated angular distributions $d\sigma(\theta)/d\Omega$ (in Lab.) of the pion from the (K^{-}, π^{-}) reaction on ^{9}Be. The final $^{9}_{\Lambda}\text{Be}$ states are assigned with $L^{\pi}(J = L \pm 1/2)$.

13.0 MeV)[4] is confirmed as the substitutional state of the last odd neutron of the target $^{9}\text{Be}(3/2^{-}_{\text{g.s.}})$.

The $K^{\pi} = 0^{-}$ band head 1_{1}^{-} state obtained at $B_{\Lambda} = -0.03$ MeV (7.5 MeV excitation) has not been observed yet as a peak. As shown by Eqs. (3·5) and (3·6), the wf of the 1_{1}^{-} state mainly consists of the linear combination of $[^{8}\text{Be}(0^{+}) \times \Lambda(1^{-})]$ and $[^{8}\text{Be}(2^{+}) \times \Lambda(1^{-})]$ configurations similarly to that of the 1_{2}^{-} state except the relative sign. However the wf of the ^{9}Be target resembles the 1_{2}^{-} wf in its structure but not the 1_{1}^{-} wf. Thus, in our calculation, the significant cancellation occurs to weakly populate the 1_{1}^{-} state. A few MeV α-decay width (See §6) and the tail of the big 1_{2}^{-} peak seem to make the observation more difficult.

To another strong peak observed at $B_{\Lambda}^{\text{exp}} = -17$ MeV we naturally assign the "neutron-hole configuration" in the ^{8}Be core, which is generated by the recoilless conversion of a deeper $p_{/\!/}$-orbit (and/or s-orbit) neutron to Λ. In other words this configuration may be obtained from the 1_{1}^{-} state, $^{8}\text{Be} \times (p_{/\!/})_{\Lambda}$, by exciting a $p_{/\!/}$-neutron to the upper $p_{\perp}$-orbit. The energy spacing between the two p-orbits for nucleon is known experimentally to be about 17 MeV,[44] hence the observation of the strong peak at $B_{\Lambda}^{\text{exp}} = -17$ MeV is consistent with our prediction of the 1_{1}^{-} level at $B_{\Lambda} = -0.03$ MeV. As the neutron-hole configuration itself is not within the $\alpha + \alpha + \Lambda$ model space, we give an additional evaluation of the forward cross section (4.6 mb /sr) leading to the second big peak by using the molecular orbital model.[50] The peak is regarded to contain the states generated from the intrinsic configurations,

$$(g^{4}u^{3}p_{\perp})_{\text{N}}(u)_{\Lambda} \quad \text{and} \quad (g^{3}u^{4}p_{\perp})_{\text{N}}(g)_{\Lambda},$$

where the gerade(g) and ungerade(u) orbitals are the molecular-orbital model analogs to the s and $p_{/\!/}$ states in the shell model convention. The N_{eff} is evaluated by assuming the substitutions $(u)_{\text{N}} \rightarrow (u)_{\Lambda}$ and $(g)_{\text{N}} \rightarrow (g)_{\Lambda}$ in the ^{9}Be ground state $((g^{4}u^{4}p_{\perp})_{\text{N}})$ and making an angle-average approximation instead of the exact angular momentum projection for the wf's.

The calculated (K^{-}, π^{-}) production rates leading to the ground state peak and the two big peaks are thus compared:

$$^{9}_{\Lambda}\text{Be}: \quad \frac{d\sigma}{d\Omega}(0°) = \begin{cases} 0.007 \text{ mb/sr} & (1/2^{+}_{\text{g.s.}}; \quad B_{\Lambda}^{\text{exp}} = 6.71 \text{ MeV}), \\ 1.3 \quad \text{mb/sr} & (3/2_{2}^{-}(L = 1_{2}^{-}); \quad -6.3 \quad \text{MeV}), \\ 4.6 \quad \text{mb/sr} & ((3/2^{-}); \quad -17.0 \quad \text{MeV}). \end{cases}$$

Table VII. Calculated E2 and M1 transition rates T and the energies. For the B(E2) and B(M1) values, see the corresponding figures for the energy level schemes.

	$i \rightarrow f$	T(E2) [sec^{-1}]	T(M1) [sec^{-1}]	E^{cal}[MeV]	E^{exp}[MeV]
$^9_\Lambda$Be	$5/2^+ \rightarrow 1/2^+$	3.9×10^{12}	—	3.06	3.079 ± 0.040[a]
	$3/2^+ \rightarrow 1/2^+$	3.9×10^{12}	—	3.06	
$^8_\Lambda$Be	$1_2^- \rightarrow 1_1^-$	1.1×10^{10}	1.2×10^{13}	1.20	
	$2^- \rightarrow 1_1^-$	1.0×10^8	2.4×10^{12}	0.65	
	$1_2^- \rightarrow 2^-$	8.6×10^8	2.3×10^{11}	0.55	
$^8_\Lambda$Li	$1_2^- \rightarrow 1_1^-$	6.6×10^9	4.0×10^{10}	1.22	1.22 ± 0.04[b]
	$2^- \rightarrow 1_1^-$	1.5×10^8	3.7×10^{11}	0.66	
	$1_2^- \rightarrow 2^-$	6.7×10^8	1.3×10^{12}	0.56	
$^7_\Lambda$Li	$3/2^+ \rightarrow 1/2^+$	0.000	8.2×10^{12}	1.10	
	$5/2^+ \rightarrow 1/2^+$	9.5×10^{10}	—	1.99	2.034 ± 0.023[c]
	$\rightarrow 3/2^+$	2.7×10^8	0.000	0.89	
	$7/2^+ \rightarrow 3/2^+$		—	1.82	
	$\rightarrow 5/2^+$		5.2×10^{12}	0.93	

a) Ref. 10b), b) Ref. 7), c) Ref. 10a).

The calculation predicts the biggest cross section to the third peak, and its ratio to the second peak (about 3.5) seems to be consistent with the observed feature.[4]

Figure 7 shows the calculated excitation spectra at $\theta = 13.5°$ ($p_K = 720$ MeV/c) and also that for $p_K = 0$ MeV/c, the latter of which may correspond to the stopped K^- absorption from the atomic s-orbit. It is noted that the $L = 2^+$ and $L = 1_1^-$ states should newly come into observation by choosing such experimental conditions. Possible observation of the genuinely hypernuclear states among rich energy levels are particularly interesting.

In Fig. 8 are displayed the calculated angular distributions of pions from the ^{9}Be(K^-, π^-)$^9_\Lambda$Be(L^π) reaction with $p_K = 720$ MeV/c. They may be classified into three types which are also applicable to the cases other than $^9_\Lambda$Be:

(1) the forward-peaked type indicating the $\Delta l = 0$ production,
(2) the $\Delta l \neq 0$ mountain type with the maximum at $\theta = 10° - 15°$,
(3) the type with quite flat dependence on θ.

The last type is typically seen in the 1_1^- case here and indicates some cancellation as mentioned above.

3.3. *Electromagnetic properties*

Three pioneering observations of the hypernuclear γ-rays have been reported in this region of hypernuclei,[7],[10] though only their energies are known. The calculated values of the transition rates and energies in $^7_\Lambda$Li and $^8_\Lambda$Be are summarized in Table VII. It is remarkable that all the observed γ-ray energies are in good agreement with the predictions of our three-cluster model.

In Fig. 5 the B(E2; $L \rightarrow L'$) values in e^{2}fm^4 are shown with arrows instead of

$$B(\text{E2}; J \rightarrow J') = [L][J'] W(L' \frac{1}{2} 2J; J'L)^2 B(\text{E2}; L \rightarrow L'), \tag{3.9}$$

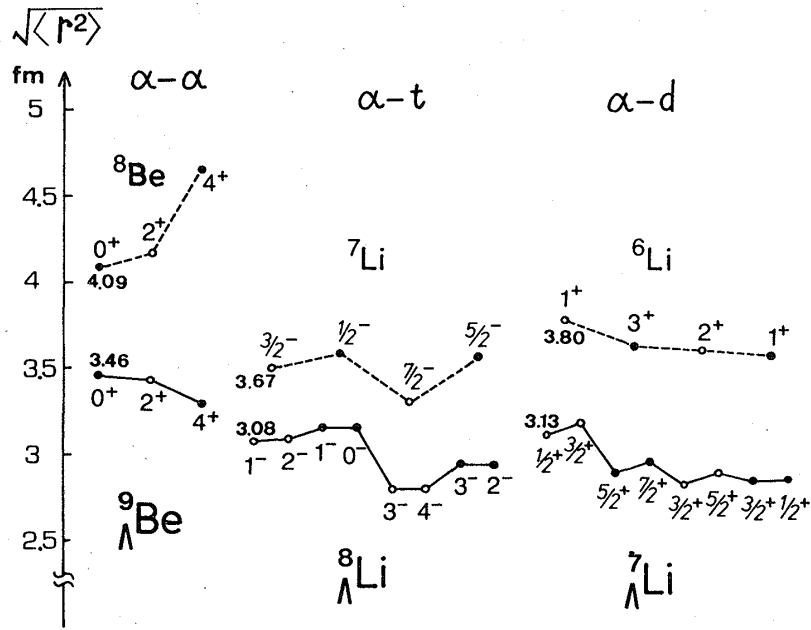where $J = L \pm 1/2$. It should be noted that the intra-band B(E2) values for the $K^\pi = 0^+$

Fig. 9.   Root-mean-square estimates of the α-x inter-cluster distance in the low-lying states (J^π) of the hypernuclei and of the corresponding core nuclei.

band of $^9_\Lambda$Be are reduced to nearly half of the corresponding cascades in the ^{8}Be ground band as shown in Fig. 5.   Such reduction of hypernuclear E2 transition rates is generally recognized in the other forthcoming cases, too.   The reason is because the Λ particle plays a glue-like role and induces a sizable dynamical contraction of the hypernuclear system.   The nuclear responses are displayed in Fig. 9 where the changes of inter-cluster distances before and after the Λ-addition amount to 10 ~ 18 %.   It is predicted that by observing hypernuclear γ-ray strengths one can see the dynamical change of nuclear structure with the Λ particle as a probe.

In spite of this contraction, the estimated B(E2) values remain several times enhanced in comparison with the shell model limit ones, indicating the importance of clustering.   In fact the present B(E2)'s in the K=0$^+$ band (K=0$^-$ and 1$^-$ bands) of $^9_\Lambda$Be are about 6(10) times larger than our shell-model limit values.   Our B(E2) estimates without using additional effective charge are significantly larger than the shell-model predictions by Dalitz and Gal (D-G)[18] who obtained a large splitting between the first doublet; 3/2$^+$ state at 2.09 MeV and 5/2$^+$ state at 3.66 MeV above the ground 1/2$^+$ state:

$$B(\text{E2}; 3/2^+ \to 1/2^+) = 11.26 \text{ e}^2\text{fm}^4 , \quad (\text{D-G: } 3.54 \text{ e}^2\text{fm}^4)$$

$$B(\text{E2}; 5/2^+ \to 1/2^+) = 11.26 \text{ e}^2\text{fm}^4 , \quad (\text{D-G: } 3.49 \text{ e}^2\text{fm}^4)$$

$$B(\text{E2}; 5/2^+ \to 3/2^+) = 3.24 \text{ e}^2\text{fm}^4 .$$

The non-vanishing M1 cascades within the $K=0^+$ band exist for the spin-flip transitions of 5/2$^+$ → 3/2$^+$ and 9/2$^+$ → 7/2$^+$, though the doublets are respectively degenerate in our model:

$$B(\text{M1}; 5/2^+ \to 3/2^+) = 0.28 \text{ nm}^2 , \quad (\text{D-G: } 0.32 \text{ nm}^2)$$

$$B(\text{M1}; 9/2^+ \to 7/2^+) = 0.31 \text{ nm}^2 .$$

The predicted lifetime of the first excited state is now

$$\tau(3/2^+) = 0.27 \text{ psec } [\ 1.61 \text{ psec}], \quad (\text{D-G}: 1.43 \sim 5.81 \text{ psec})$$

where the value in [ ] is our shell-model limit one. The magnetic dipole moment of the ground state is calculated to be

$$\mu(^9_\Lambda\text{Be}; 1/2^+) = -0.610 \text{ nm}$$

for which almost entire contribution comes from the Λ particle magnetic moment of the s-state (cf. Table VIII).

The reduced E1 transition probabilities are also estimated for the negative-parity to positive-parity cascades. Because the Λ particle has no charge, they originate from the recoil of the $\alpha + \alpha$ core nucleus associated with the Λ particle transition mainly from the p-state to the s-state. Table IX lists some $B(\text{E1})$ estimates, which are around the Weisskopf value $B(\text{E1})_{\text{wu}} = 0.055 \text{ e}^2\text{fm}^2$. It is noteworthy that these values will undergo no

Table VIII. Magnetic moments of the hypernuclear ground states and their devided contributions from the orbital and spin parts which are given by Eqs. $(2\cdot46) \sim (2\cdot48c)$.　(nm＝nuclear magneton)

	J^π(g.s.)	(nm)	$\langle \mathcal{M}_l^{ax} \rangle$	$\langle \mathcal{M}_\Lambda^A \rangle$	$\langle \mathcal{M}_s^{ax} \rangle$	$\langle \mathcal{M}_s^A \rangle$	$\langle \text{SUM} \rangle$
$^9_\Lambda$Be	$1/2^+$	-0.610	0.0	0.0	0.0	-0.730	-0.730
$^8_\Lambda$Be	1^-	1.052	0.552	0.0005	0.502	0.204	1.259
$^8_\Lambda$Li	1^-	0.367	0.376	0.0003	-0.141	0.204	0.439
$^7_\Lambda$Li	$1/2^+$	0.791	0.001	-0.0001	0.702	0.245	0.947
$^6_\Lambda$Li	1^-	3.322	0.909	0.0002	2.701	0.367	3.976
$^6_\Lambda$He	1^-	-1.155	0.101	0.0002	-1.850	0.367	-1.382

Table IX.　Estimates of $B(\text{E1}; J_i \rightarrow J_f)$.　(e²fm²)

$^9_\Lambda$Be	$(L^\pi)J_i \longrightarrow (L)J_f$:	$(0)1/2^+$	$(2)3/2^+$	$(2)5/2^+$	$(4)7/2^+$
	$(1^-)1/2^-$	0.081	0.092	—	—
	$3/2^-$	0.081	0.009	0.083	—
	$(3^-)5/2^-$	—	0.103	0.007	0.052
	$(1_2^-)1/2_2^-$	0.019	0.039	—	—
	$3/2_2^-$	0.019	0.004	0.035	—

$^8_\Lambda$Li	$J_i \longrightarrow J_f$	1^-	2^-	1_2^-	0^-
($^8_\Lambda$Be)	0^+	$0.083(0.148)$	—	$0.007(0.013)$	—
	1^+	$0.003(0.005)$	$0.052(0.093)$	$0.028(0.049)$	$0.010(0.018)$
	2^+	$0.056(0.099)$	$0.001(0.002)$	$0.000(0.000)$	—

$^7_\Lambda$Li	$J_i \longrightarrow J_f$:	$1/2^+$	$3/2^+$	$5/2^+$	$7/2^+$	$3/2_2^+$
	$3/2^-$	0.084	0.001	0.019	—	0.002
	$1/2^-$	0.088	0.000	—	—	0.015
	$5/2^-$	—	0.095	0.000	0.012	0.000
	$1/2_2^-$	0.000	0.098	—	—	0.001
	$3/2_2^-$	0.001	0.096	0.001	—	0.001

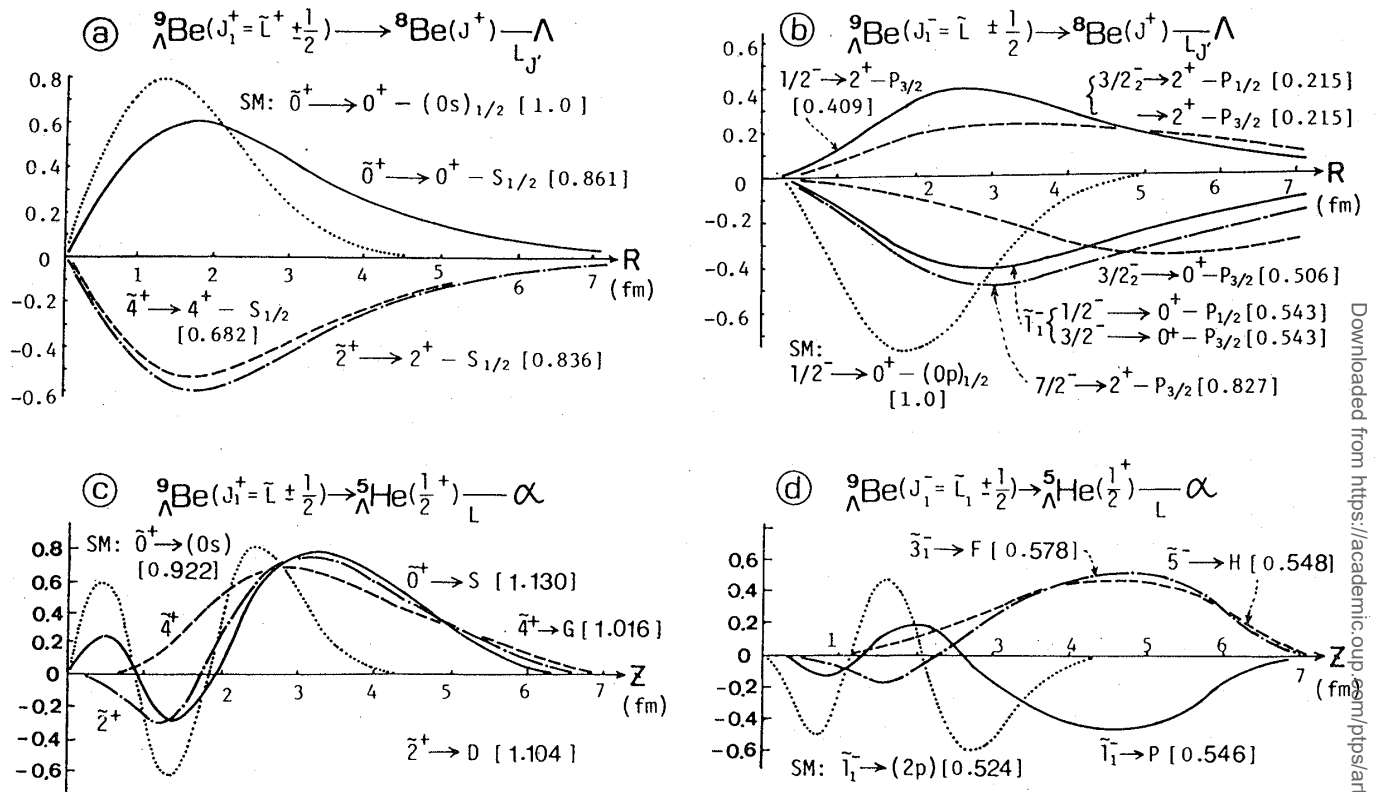| $^6_\Lambda$He	$J_i \longrightarrow J_f$:	1^-	2^-	1_2^-
($^6_\Lambda$Li)	0^+	$0.069(0.155)$	—	$0.004(0.008)$
	1^+	$0.011(0.024)$	$0.057(0.129)$	$0.003(0.006)$
	2^+	$0.057(0.127)$	$0.004(0.004)$	$0.000(0.000)$

Fig. 10   The reduced width amplitudes (RWA) of $^9_\Lambda$Be as a function of the relative distance (R or Z) between the two fragments.   The corresponding spectroscopic factors are given in [ ] after the indicated decay channels.   For comparison the typical shell-model (SM) RWA are drawn by dotted lines.

Table X.   Estimates of partial decay widths Γ_c of the typical resonance states.   The separation energy method is employed.   For definitions see Eqs. (2·49a) and (2·49b).

	J^π	B_Λ $[B_\Lambda^{\exp}]$	decay channels	S-factor	radius a(fm)	P	γ_w^2 (MeV)	θ_L^2	Γ_c (MeV)
$^9_\Lambda$Be	$1/2_1^-$ ($L=1_1^-$)	-0.03 [*]	$^8\text{Be}(0^+)-\Lambda(P_{1/2})$	0.543	3.5	0.23	4.29	0.19	0.42
			$^5_\Lambda\text{He}(1/2^+)-\alpha(^1P_1)$	0.546	5.0	2.81	1.10	0.15	1.86
	$3/2_2^-$ ($L=1_2^-$)	-5.31 [-6.3]	$^8\text{Be}(0^+)-\Lambda(P_{3/2})$	0.506	6.0	3.03	1.67	0.25	2.53
			$^8\text{Be}(2^+)-\Lambda(P_{3/2})$	0.215	4.5	1.37	2.91	0.10	0.80
			$^8\text{Be}(2^+)-\Lambda(P_{1/2})$	0.215	4.5	1.37	2.91	0.10	0.80
			$^5_\Lambda\text{He}(1/2^+)-\alpha(^1P_1)$	0.532	5.0	3.15	1.10	0.15	2.08
$^7_\Lambda$Li	$3/2^-$	-3.10 [-2.7]	$^6\text{Li}(1^+)-\Lambda(P_{3/2})$	0.412	5.5	1.84	2.08	0.17	1.26
			$^6\text{Li}(1^+)-\Lambda(P_{1/2})$	0.441	5.5	1.84	2.08	0.17	1.26
			$^6\text{Li}(3^+)-\Lambda(p_{3/2})$	0.120	4.0	0.52	3.83	0.03	0.12
			$^5_\Lambda\text{He}(1/2^+)-d(^3P_2)$	0.132	5.0	2.53	1.73	0.07	0.58
$^6_\Lambda$Li	1^+	-4.07 [-3.8]	$^5\text{Li}(3/2^-)-\Lambda(P_{3/2})$	0.557	5.5	1.94	2.15	0.23	1.90
			$^5\text{Li}(3/2^-)-\Lambda(P_{1/2})$	0.433	5.5	1.94	2.15	0.12	0.99
			$^5\text{Li}(1/2^-)-\Lambda(P_{3/2})$	0.008	5.0			0.00	0.00
			$^5_\Lambda\text{He}(1/2^+)-p(^2S_2)$	0.058	6.0	3.37	2.06	0.03	0.33

*) Not observed.
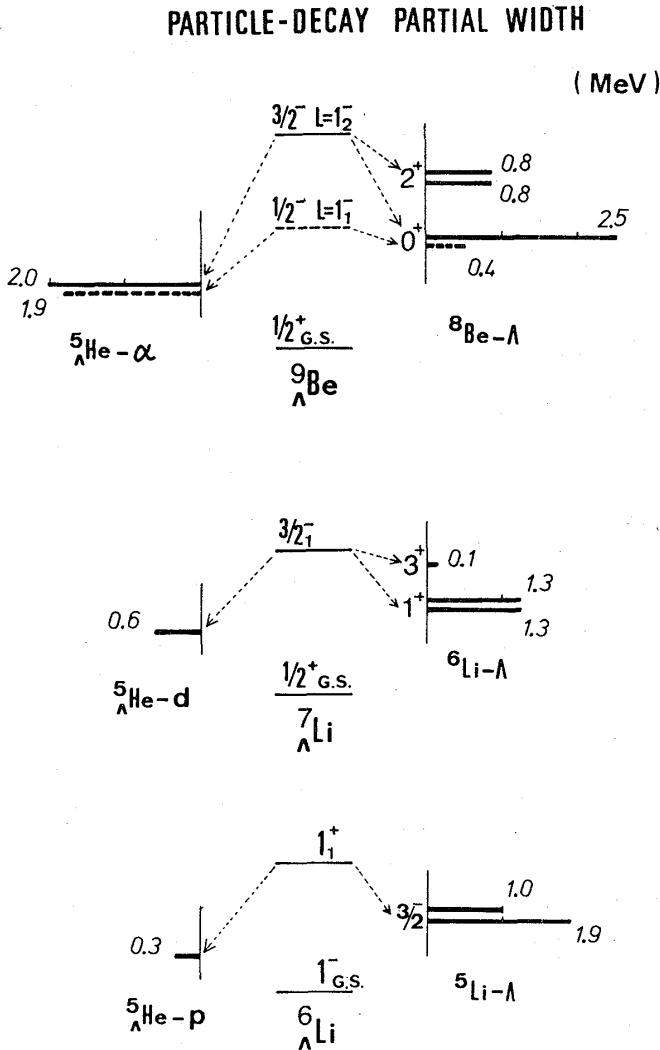
Fig. 11. Estimates of the partial decay widths (MeV) of the typical hypernuclear states.

quenching effects, because the Λ particle with zero isospin cannot excite isovector giant resonances of the core nucleus.

3. 4. Reduced width amplitudes and particle-decay widths

In Fig. 10 are displayed the reduced width amplitudes(RWA) and spectroscopic factors leading to the $^5_\Lambda$He-α and ^{8}Be-Λ channels. Though the cluster-model S-factor does not differ from the corresponding shell-model limit one, the former relative wf naturally extends to much larger distance. From the relevant RWA's, we evaluate the partial decay widths (Γ_c) on the basis of the separation energy method described in §2.5. The results are listed in Table X and displayed also in Fig. 11. From these we have a rough estimate of the total widths by assuming the relation: $\Gamma \cong \sum_c \Gamma_c$.

$$^9_\Lambda\text{Be}(1/2_1^-, L=1_1): \quad \Gamma = 2.28\text{MeV},$$

$$^9_\Lambda\text{Be}(3/2_2^-, L=1_2): \quad \Gamma = 6.21\text{MeV},$$

the latter of which seems to be consistent with the observed width (~ 7 MeV) of the strong peak at $B_\Lambda^{\text{exp}} = -6.3$ MeV.[4] More realistic estimates of the particle-decay widths are achieved by solving the scattering equation, which also gives the same value $\Gamma(3/2_2^-) \cong 6.2$MeV as will be described in §6.

3. 5. Use of the realistic ΛN interaction (YNG)

In this subsection we examine the effect of using the realistic YNG(ΛN) interaction,[38] Eq. (2·30), by comparing the results with those of the one-range Gaussian interaction(ORG) of Eq. (2·29). First we solve the $^5_\Lambda$He$=\alpha+\Lambda$ problem in the GCM framework with the basis wf:

$$\Phi_l(d) = \phi_\alpha^{\text{int}}\varphi_l(r; d) Y_l(\hat{r}), \tag{3·10a}$$

$$\varphi_l(r; d) = 4\pi(\sqrt{\pi}\, b_{\alpha\Lambda})^{-3/2}\exp[-(r^2+d^2)/2b_{\alpha\Lambda}^2]\mathscr{I}_l(rd/b_{\alpha\Lambda}^2), \tag{3·10b}$$

$$b_{\alpha\Lambda} = \sqrt{(4M_N+M_\Lambda)/4M_\Lambda}\ b_N. \tag{3·11}$$

See Appendix A for the expressions of the GCM normalization and energy kernels.

By employing the YNG(ΛN; $k_F=0.9$, $x=0$) interaction with 7 mesh points for the α-Λ distance parameter

Table XI. The even-odd and direct-exchange representations of the parameters of the YNG(ΛN; $k_F=0.9$, $x=0$) interaction. See Eqs. (2·30) and (3·12) for the notations and Chapter II for the details of the interaction. This set is used in §3.5 for the $^5_\Lambda$He and $^9_\Lambda$Be calculations.

β_i	V^0(E)	V^0(O)	V_D^0	V_{ex}^0
1.5 (fm)	-9.93	-7.66 (MeV)	-8.80	-1.13 (MeV)
0.9	-227.73	-82.55	-155.14	-72.59
0.5	1021.17	717.40	869.28	151.89

$$d=0.0,\ 1.0,\ 2.5,\ 4.0,\ 5.5,\ 7.0\ \text{and}\ 8.5\ \text{fm},$$

we obtain a satisfactory value for the Λ-binding energy in $^5_\Lambda$He($1/2^+_{\text{g.s.}}$):

$$^5_\Lambda\text{He}(1/2^+,\ l=0):\quad B_\Lambda^{\text{cal}}=3.08\ \text{MeV(YNG)}\quad \text{vs.}\quad 3.11\ \text{MeV(ORG)},$$

$$(B_\Lambda^{\text{exp}}=3.12\ \text{MeV}).$$

The YNG(ΛN) parameters are listed in Table XI, where the direct and exchange interaction strengths are defined by

$$\begin{cases} V_D^0=[V^0(\text{E})+V^0(\text{O})]/2, \\ V_{ex}^0=[V^0(\text{E})-V^0(\text{O})]/2, \end{cases} \tag{3·12a}$$

$$\begin{cases} V^0(\text{E})=\{v^0(^1\text{E})+3v^0(^3\text{E})\}/4, \\ V^0(\text{O})=\{v^0(^1\text{O})+3v^0(^3\text{O})\}/4. \end{cases} \tag{3·12b}$$

Here we note that, in the $v_{\Lambda N}=V_D+V_{ex}\hat{P}_{\Lambda N}$ form of the YNG interaction, the ΛN exchange operator $\hat{P}_{\Lambda N}$ should be regarded as transforming $r_{\Lambda N}=r_\Lambda-r_N$ to $-r_{\Lambda N}$ without changing the center-of-mass coordinate.

The α-Λ wf ($l=0$) with YNG is found to be cosiderably different from the ORG correspondent, although both interactions are successful in reproducing $B_\Lambda^{\text{exp}}(^5_\Lambda\text{He})$. The bahaviors of the two wf's are compared in Fig. 12. The h.o. components of both wf's are listed in Table XII, where we recognize increased importance of the $n=1$ component $u_{1s}(r;\ b_{\alpha\Lambda})$ in the YNG wf. Figure 12 also shows the α-Λ potentials $V_{\alpha-\Lambda}(r)$ which are obtained by folding the ΛN interactions with $\phi_\alpha^{\text{int}}(b_N=1.358$ fm). In the YNG case, the folding potential obtained by applying the even-state force to both even and odd states is displayed, though, of course, the wf is calculated correctly with the original interaction. It is interesting to note that the YNG $V_{\alpha-\Lambda}(r)$ is repulsive at the short distance, reflecting the presence of
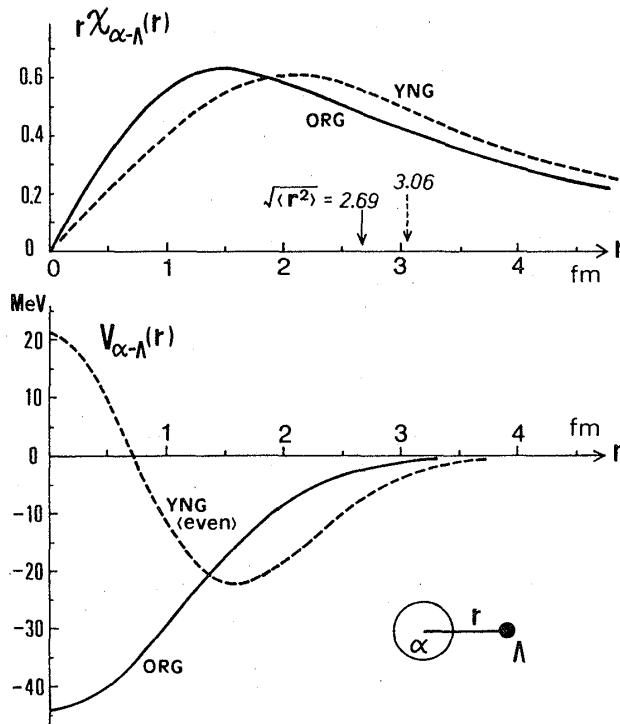

Fig. 12. Comparison of the α-Λ radial wave functions and direct potentials folded by $\phi_\alpha^{\text{int}}(b_N=1.358\text{fm})$ which are calculated from the ORG and YNG (ΛN) interactions.

Table XII. Harmonic oscillator expansions of the a-Λ ground state wave functions obtained with the two ΛN interactions. Note that $N = 2n + l$. The calculated energies and a-Λ root-mean-square distances are listed.

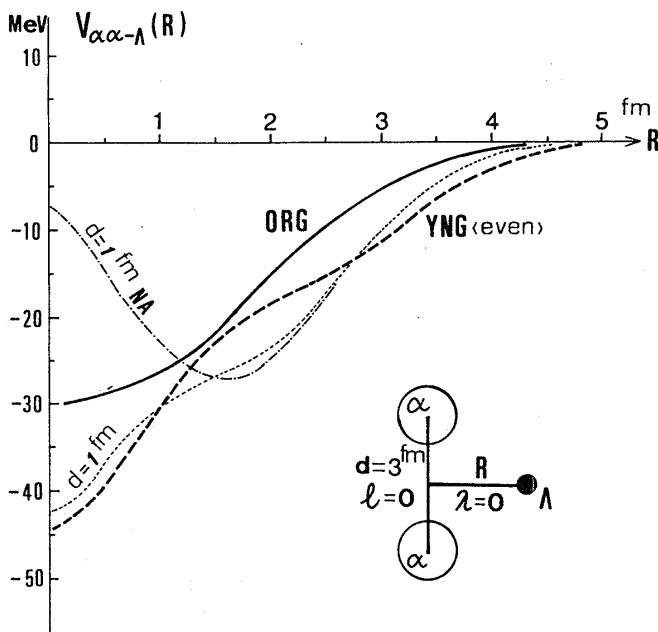|	a-Λ $l=0$ $(1/2^+)$	
	ORG	YNG
$E_\Lambda = -B_\Lambda$	-3.11	-3.08 (MeV)
$\sqrt{\langle r^2 \rangle_{a-\Lambda}}$	2.69	3.06 (fm)
$n=0$	0.917	0.844
1	-0.251	-0.415
2	0.232	0.217
3	-0.132	-0.181
4	0.107	0.123
5	-0.075	-0.086
6	0.060	0.069
7	-0.045	-0.057
$\vdots$	$\vdots$	$\vdots$

Fig. 13. Comparison of the ^{8}Be(l)-Λ folding potentials for the $(l, \lambda) = (0, 0)$ channel calculated from the ORG and YNG(ΛN) interactions. Comments as for Fig. 6.

the repulsive (soft) core in the two-body YNG(ΛN). As a result the YNG wf is pushed away to the outside as seen in Fig. 12. This feature[51] gives rise to a sizable difference between the r.m.s. estimates of the a-Λ distance,

$$\sqrt{\langle r^2 \rangle_{a-\Lambda}} = 3.06 \text{ fm (YNG)} \quad \text{vs.}$$

$$2.69 \text{ fm (ORG)}.$$

One can compare these values with the empirical r.m.s. radius of the a-particle $\sqrt{\langle r^2 \rangle_a} = 1.40$ fm which is consistent with the present choice $\phi_a^{\text{int}}(b_N = 1.358 \text{ fm})$.

In the similar way we solve the $^9_\Lambda$Be $= a + a + \Lambda$ problem in the GCM formalism by which the ΛN exchange interaction in YNG is also taken into account straightforwardly. Instead of the basis of Eq. (2·7), we adopt here the GCM basis function

$$[\Phi^{aa}(l; d) \times \varphi_\lambda^\Lambda(R: D) Y_\lambda(R)]_L , \tag{3·13a}$$

$$\varphi_\lambda^\Lambda(R; D) = 4\pi(\sqrt{\pi} b_R)^{-3/2} \exp[-(R^2 + D^2)/2b_R^2] \mathscr{J}_l(RD/b_R^2), \tag{3·13b}$$

where $\Phi^{aa}(l; d)$ and b_R are given by Eqs. (2·2) and (2·9), respectively $(x=4)$. The expression of the matrix element of ΛN interaction $\sum_{i=1}^8 \{V_D(\Lambda i) + V_{\text{ex}}(\Lambda i)\hat{P}_{\Lambda N}(\Lambda i)\}$ is somewhat lengthy and is given in Appendix B.
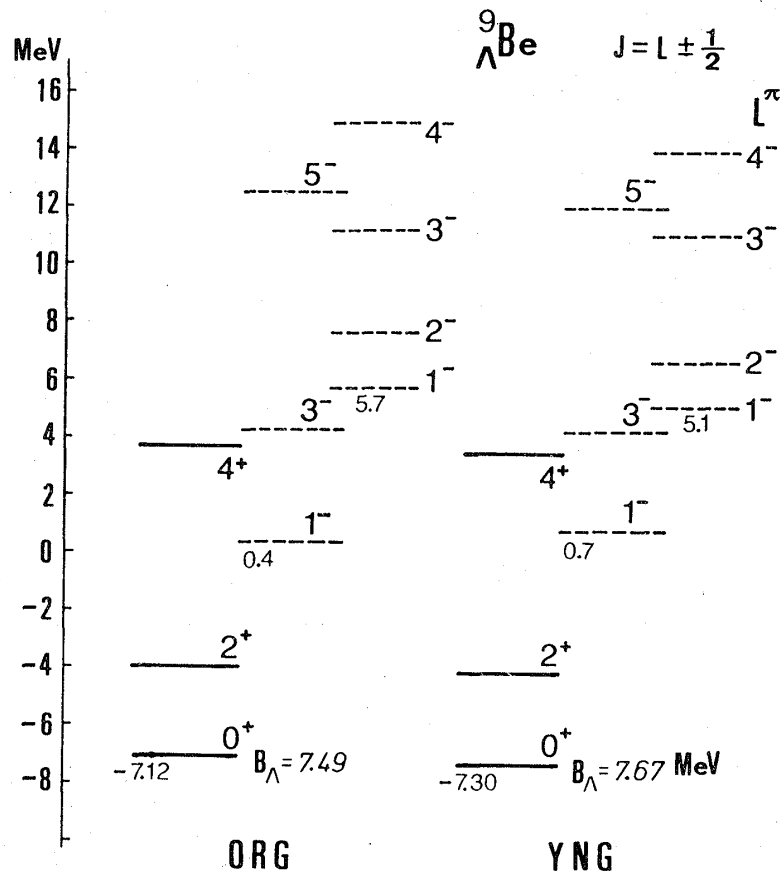
Fig. 14.   Energy levels of $^9_\Lambda$Be calculated from the ORG and YNG(ΛN) interactions.   The inter-cluster correlation energies are shown.

In Fig. 13 we compare the examples of the ORG and YNG potentials for Λ, $V_{\alpha\alpha-\Lambda}(R)$, which are obtained by folding the two-body ΛN force with the di-α basis wf in the case of the representative distance $d_{\alpha-\alpha}=3.0$ fm.   The geometry is shown also in the same figure.   In general the potential $V_{\alpha\alpha-\Lambda}(R)$ is nearly twice as strong as the α-Λ potential $V_{\alpha-\Lambda}$, since the di-α clusterization is well maintained in the case $d_{\alpha-\alpha}=3.0$ fm.   Reflecting the stronger attraction of $V_{\alpha-\Lambda}(r)$ in the distant region, the YNG(even) folding potential $V_{\alpha\alpha-\Lambda}(R)$ is considerably deep and does not show such a simple behavior as the ORG case. The effect of the short-range repulsive core of the YNG interaction can be seen at small R, if we choose a shorter distance parameter $d_{\alpha-\alpha}=1.0$ fm and at the same time employ the basis wf without anti-symmetrization between the nucleons belonging to the different α clusters.   The effect is typically shown by the dotted curve(NA) in Fig. 13, although the raising at small R disappears due to the nucleon antisymmetrization.   It is generally true that the effect of the two-body repulsive core tends to be averaged out and disappear in the Λ-nucleus folding potential as the mass number increases and also because of the nucleon antisymmetrization.

In the calculation of the $^9_\Lambda$Be energy levels, we adopt the following restriction for the model space:

α-α distance parameter: $d=1.0$, 2.25, 3.5, 5.0, 6.5 fm,

^{8}Be-Λ distance parameter: $D=0.5$, 2.5, 4.5, 6.5 fm,

angular momenta:　$l=0, 2, 4.$　and　$\lambda=0, 1, 2.$

The results with the two interactions are compared in Fig. 14 where the ORG result is essentially the same as in Fig. 4. One should note here that the ΛN exchange force in the

Table XIII. (a) Squared channel-amplitudes (in %) of the $^9_\Lambda$Be($L=0^+$) ground state wave functions obtained with ORG and YNG interactions.

	$(l, \lambda)=(0, 0)$	$(2, 2)$	$(4, 4)$
ORG	94.5	5.3	0.2　(%)
YNG	98.0	2.0	0.04

(b) The h.o. components (in %) of the Λ-wf($\lambda=0$) and the r.m.s. distances normalized within the $(l, \lambda)=(0, 0)$ channel of the $^9_\Lambda$Be($L=0^+$) wf. See the caption of Table V.

	ORG	YNG
$\nu=1$	83.8	76.0 (　%)
2	11.3	16.6
3	3.1	4.8
4	1.0	1.5
$\vdots$	$\vdots$	$\vdots$
$\sqrt{\langle R^2 \rangle_\Lambda}$	2.39　(fm)	2.60　(fm)
$\sqrt{\langle r^2 \rangle_{\alpha-\alpha}}$	3.44	3.57

Table XIV. Summary of the Λ-particle binding energies B_Λ, the forward production cross sections $d\sigma(0°)/d\Omega$ and the level widths Γ for the ground state and some excited states strongly populated in the (K^-, π^-) reactions.

		g.s. peak		big peak	big peak
$^9_\Lambda$Be	$B_\Lambda{}^{\text{exp}}$	6.71	*	-6.3	-17.0 [MeV]
	B_Λ(ORG)	7.49($1/2^+$)	$-0.03(1/2^-, 3/2^-)$	$-5.31(3/2^-)$	—
	B_Λ(YNG)	7.67($1/2^+$)	$-0.23(1/2^-, 3/2^-)$	$-5.33(3/2^-)$	—
	B_Λ(§6)		$-0.2\ (1/2^-, 3/2^-)$	$-6.0\ (3/2^-)$	—
	$\dfrac{d\sigma}{d\Omega}(0°)$	0.007	0.04	1.3	4.6 [mb/sr]
	Γ		2.28	6.21	−　[MeV]
	Γ(§6)		2.0	6.2	—
$^8_\Lambda$Be	$B_\Lambda{}^{\text{exp}}$	6.84	*	*	* [MeV]
	B_Λ(ORG)	6.66(1^-)	$-0.09(0^+)$	$(-2.95(2^+))$	
$^8_\Lambda$Li	$B_\Lambda{}^{\text{exp}}$	6.80(1^-)	*	*	* [MeV]
	L_Λ(ORG)	6.77(1^-)	$-0.20(0^+)$	$(-3.04(2^+))$	—
$^7_\Lambda$Li	$B_\Lambda{}^{\text{exp}}$	5.58		-2.7	-14.6 [MeV]
	B_Λ(ORG)	5.59($1/2^+$)		$-3.10(3/2^-)$	—
	$\dfrac{d\sigma}{d\Omega}(0°)$	0.04		3.3	2.1 [mb/sr]
	Γ			3.22	−　[MeV]
$^6_\Lambda$Li	$B_\Lambda{}^{\text{exp}}$	4.5**)		-3.8	-13.8 [MeV]
	B_Λ(ORG)	3.97(1^-)		$-4.07(1^+)$	—
	$\dfrac{d\sigma}{d\Omega}(0°)$	0.007		1.5	2.4 [mb/sr]
	Γ			3.22	−　[MeV]

*) Not observed.　**) 4.25 MeV for $^6_\Lambda$He.

YNG interaction is fully taken into account in the calculation.

The YNG ground band is calculated to be just parallel to the ORG one with almost the same ground state energy, $B_A = E(^8Be) - E(^9_A Be)$:

$$^9_A Be(1/2^+, L=0^+): \quad B_A{}^{cal} = 7.67 \text{ MeV (YNG)} \quad vs. \quad 7.49 \text{ MeV (ORG)}.$$

The YNG negative parity levels are obtained to constitute the two-band structure similar to the ORG result, though some differences in the level energies are seen between the two cases.

As for the wf's, we list in Table XIII the channel amplitudes of the ground state total wf and the h.o. components of A-wf within the dominant angular momentum channel $[(l=0) \times (\lambda=0)]_{L=0}$. Table XIII(b) shows that the share of the $u_{1s}(R)$ component becomes larger in the YNG A-wf than in the ORG one. According to the estimates of the α-α and ^8Be-A distances listed in the same table, we find that the size of the YNG $^9_A Be(L =0^+)$ wf is larger than the ORG correspondent. The difference is evidently due to the inner repulsive core and the relatively long-range property of the YNG interaction.

In spite of the above discussed differences, we conclude that the realistic YNG (AN) interaction does not change the ORG results seriously, hence the structure characteristics clarified in §3.1 should essentially persist.

In Table XIV are summarized the main results of the present calculations for the ground state and two big peaks observed in the (K^-, π^-) reactions.
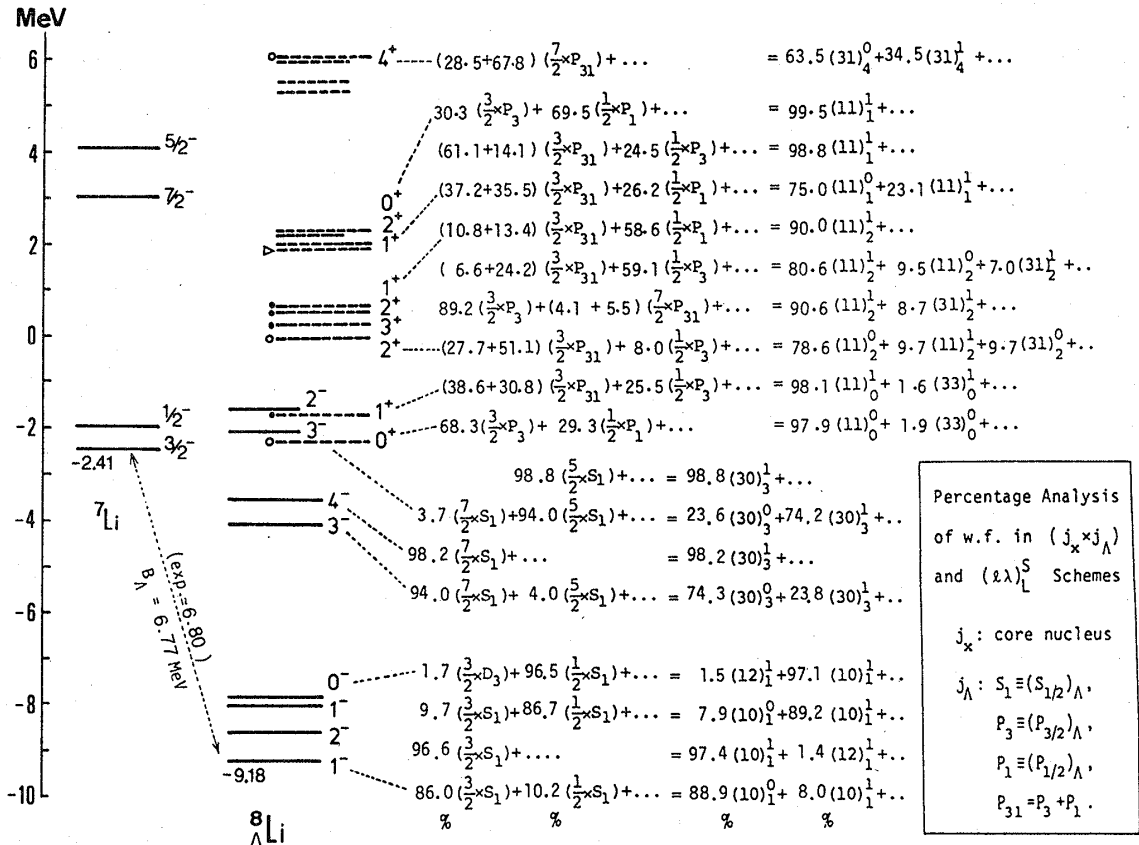

Fig. 15. Calculated energy spectra of ^{7}Li and ^9_ALi. Comments as for Fig. 4 except that the wave functions are given in both the j_x-j_A and L-S coupling schemes.

§ 4. Results and discussion on $^{6,7,8}_{\Lambda}$Li, $^{8}_{\Lambda}$Be and $^{6}_{\Lambda}$He hypernuclei

4. 1. *The hypernuclei $^{8}_{\Lambda}$Li and $^{8}_{\Lambda}$Be*

In most cases of this subsection, the discussion is often restricted to $^{8}_{\Lambda}$Li, since the obtained feature of $^{8}_{\Lambda}$Be is almost parallel to those of $^{8}_{\Lambda}$Li.   Note that the major difference lies in the Coulomb energy between $^{8}_{\Lambda}$Li$=\alpha+t+\Lambda$ and $^{8}_{\Lambda}$Be$=\alpha+{}^{3}$He$+\Lambda$.   Thus, for the $^{8}_{\Lambda}$Be structure, one may replace t by ^{3}He in the following discussion.

4. 1. 1. Structure characteristics

The calculated energy spectra of $^{8}_{\Lambda}$Li are shown in Figs. 15 and 16 and those of $^{8}_{\Lambda}$Be in Fig. 17.   Note that the low-lying states of ^{7}Li $(^{7}$Be$)^{44)}$ are satisfactorily described by the
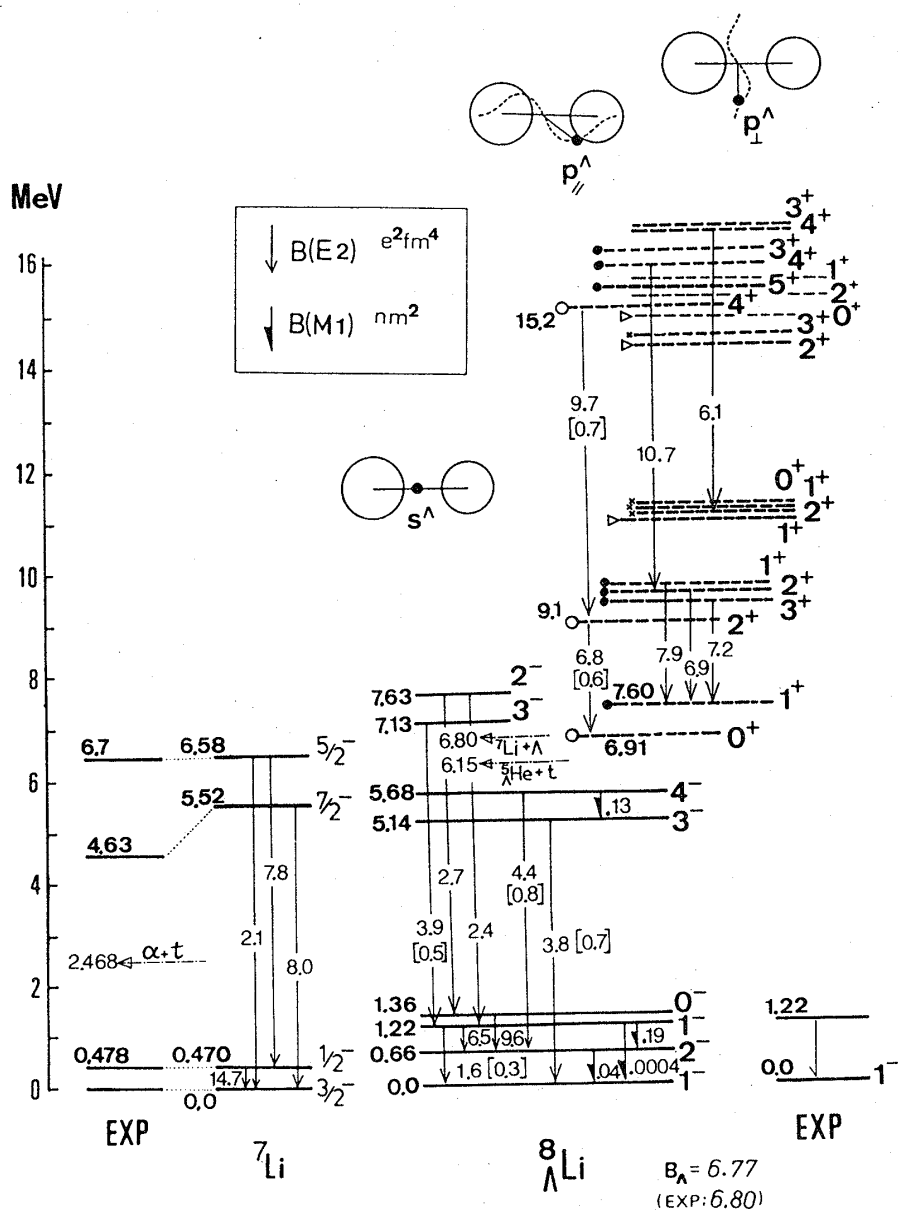

Fig. 16.   Calculated B(E2) and B(M1) in ^{7}Li and $^{8}_{\Lambda}$Li.   The levels with a similar character are indicated by open circle, dot, etc.   The experimental threshold energies are indicated in the $^{8}_{\Lambda}$Li spectrum.   The shell-model limit B(E2) values are in the square brackets.   The observed energies of ^{7}Li are from Ref. 44) and those of $^{8}_{\Lambda}$Li from Refs. 7) and 43).   See the text for more detail.

$\alpha + t$ ($\alpha + {}^3$He) di-cluster structure. Based on the lowest four levels of ^{7}Li, the 8 negative parity states are grouped into four doublets:

$$1^- \text{-} 2^-, 1^- \text{-} 0^-, 3^- \text{-} 4^- \quad \text{and} \quad 3^- \text{-} 2^-.$$

Each has the dominant structure, respectively,

$$[{}^7\text{Li}(lj) \times s^4_{1/2}] \quad \text{with} \quad lj = P_{3/2},\ P_{1/2},\ F_{7/2} \quad \text{and} \quad F_{5/2},$$

where Λ particle in the $j_\Lambda = s_{1/2}$ state weakly couples to one of the α-t di-cluster states. In fact the feature can be seen in the j_x-j_Λ representation of the $^8_\Lambda$Li wf's (cf. Fig. 15). In the L-S coupling we see considerable admixtures of $S = 0$ and $S = 1$ components caused by the $\sigma_\Lambda \cdot \sigma_N$ interaction. The illustration of the intrinsic structure is also given for these negative parity states. The calculated ground state binding energies for $^8_\Lambda$Li and $^8_\Lambda$Be are in good agreement with the observed values, respectively.
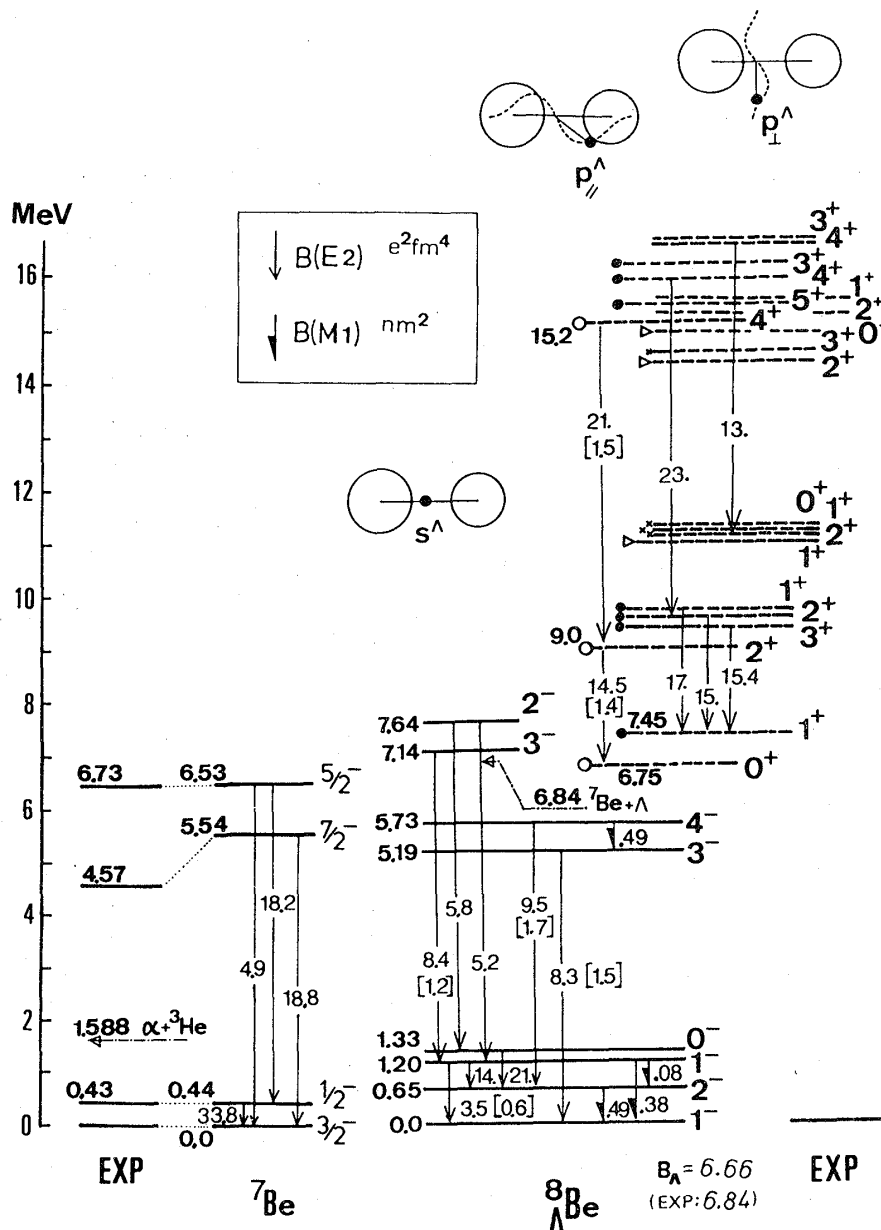
Fig. 17. Calculated energy spectra of ^{7}Be and $^8_\Lambda$Be. Comments as for Fig. 16.

$${}^{8}_{\Lambda}\text{Li}(1^{-}_{g.s.}): \quad B_{\Lambda}{}^{\text{cal}} = 6.77 \text{ MeV} \quad \text{vs.} \quad B_{\Lambda}{}^{\text{exp}} = 6.80 \text{ MeV},{}^{43)}$$

$${}^{8}_{\Lambda}\text{Be}(1^{-}_{g.s.}): \quad B_{\Lambda}{}^{\text{cal}} = 6.66 \text{ MeV} \quad \text{vs.} \quad B_{\Lambda}{}^{\text{exp}} = 6.84 \text{ MeV}.{}^{43)}$$

The first 3 doublets are obtained as particle-stable bound states located below the ${}^{5}_{\Lambda}\text{He} + t$ threshold.

We get many positive parity levels in which the Λ particle mainly occupies the p-state ($\lambda = 1$) with respect to the core nucleus ${}^{7}\text{Li}$. The analyses show that the wf's have large admixtures in the j_x-j_Λ coupling and that the L-S coupling representation is more appropriate for these levels. The spatial symmetry of the states is considerably recovered when the Λ particle participates in the p-state. The $p_{\parallel}$-type and $p_{\perp}$-type intrinsic structures are underlying these levels, hence the spectra are expected to be analogous to those of ${}^{8}\text{Be}(\alpha + \alpha; K = 0)$ and ${}^{8}\text{Li}(\alpha + t + n; K = 1)$.${}^{44)}$ In the hypernuclear $\alpha + t + \Lambda$ system, however, we have two possible spin values ($S = 0$ and 1) with essentially the same spatial structure. Thus, in terms of the strong coupling L-S scheme, we can classify them into four groups, the $S = 0$ and $S = 1$ "bands" with $K = 0(p_{\parallel})$ and $K = 1(p_{\perp})$:

(i) Spin-singlet ($S = 0$) ${}^{8}\text{Be}$-analog: $J = 0^{+}, 2^{+}, 4^{+}$.

(ii) Spin-triplet ($S = 1$) ${}^{8}\text{Be}$-analog: $J = 1^{+}, \{1^{+}, 2^{+}, 3^{+}\}, \{3^{+}, 4^{+}, 5^{+}\}$.

(iii) Spin-singlet ($S = 0$) ${}^{8}\text{Li}$-analog: $J = 1^{+}, 2^{+}, 3^{+}, \cdots$.

(iv) Spin-triplet ($S = 1$) ${}^{8}\text{Li}$-analog: $J = \{0^{+}, 1^{+}, 2^{+}\}, \{1^{+}, 2^{+}, 3^{+}\}, \cdots$.

In fact the first 0^{+}-2^{+}-4^{+} band is realized, as marked by open circle($\bigcirc$) in Fig. 16 (17). The predominant component of each wf's is $(l\lambda)^{S}_{L} = (l1)^{S=0}_{L=0,2,4}$, as

$$|0^{+}\rangle = 97.9\,\%\,(l = 1, \lambda = 1)^{S=0}_{L=0} + 1.9\,\%\,(3, 3)^{0}_{0} + \cdots, \tag{4.1}$$

Table XV. Spectroscopic factors of the ${}^{8}_{\Lambda}\text{Li}$ states leading to the indicated three channels.

$J_i{}^{\pi}({}^{8}_{\Lambda}\text{Li})$	${}^{5}_{\Lambda}\text{He}(1/2^{+}) + t$ (L_J)	$\alpha + {}^{4}_{\Lambda}\text{H}(J_x)$ (l-J_x)	${}^{7}\text{Li} + \Lambda$ (j_x-j_Λ)
1^{-}	0.79 ($P_{3/2}$)	0.62 (P-0^{+})	0.83 ($3/2$-$s_{1/2}$)
	0.08 ($P_{1/2}$)	0.06 (P-1^{+})	0.09 ($1/2$-$s_{1/2}$)
2^{-}	0.87 ($P_{3/2}$)	0.63 (P-1^{+})	0.93 ($3/2$-$s_{1/2}$)
$1_2{}^{-}$	0.79 ($P_{1/2}$)	0.59 (P-1^{+})	0.83 ($1/2$-$s_{1/2}$)
	0.08 ($P_{3/2}$)		0.09 ($3/2$-$s_{1/2}$)
0^{-}	0.88 ($P_{1/2}$)	0.64 (P-1^{+})	0.92 ($1/2$-$s_{1/2}$)
0^{+}	0.28 ($S_{1/2}$)	0.34 (S-0^{+})	0.69 ($3/2$-$p_{3/2}$)
			0.28 ($1/2$-$p_{1/2}$)
1^{+}	0.27 ($S_{1/2}$)	0.31 (S-1^{+})	0.31 ($3/2$-$p_{3/2}$)
			0.24 ($1/2$-$p_{3/2}$)
			0.39 ($3/2$-$p_{3/2}$)
2^{+}	0.23 ($D_{5/2}$)	0.30 (D-0^{+})	0.54 ($3/2$-$p_{1/2}$)
		0.04 (D-1^{+})	0.28 ($3/2$-$p_{3/2}$)
3^{+}	0.25 ($D_{5/2}$)	0.32 (D-1^{+})	0.91 ($3/2$-$p_{3/2}$)
4^{+}	0.27 ($G_{9/2}$)	0.30 (G-0^{+})	0.68 ($7/2$-$p_{1/2}$)
			0.91 ($7/2$-$p_{3/2}$)
shell-model	0.874(J^{-})		1.0
limit	0.343(J^{+})		

$$|2^+\rangle = 78.6\,\%\,(l=1,\ \lambda=1)^{S=0}_{L=2} + 9.7\,\%\,(1,\ 1)^1_2 + 9.7\,\%\,(3,\ 1)^0_2 + \cdots, \tag{4·2}$$

$$|4^+\rangle = 63.5\,\%\,(l=3,\ \lambda=1)^{S=0}_{L=4} + 34.5\,\%\,(3,\ 1)^1_4 + \cdots, \tag{4·3}$$

respectively, and therefore this band might be pictorized by the $\alpha + {}^4_\Lambda H(0^+)$ intrinsic structure as is analogous to ${}^8Be = \alpha + \alpha$. The low-lying levels of the spin-triplet ${}^8Be$-analogs which could be said "genuinely hypernuclear" are indicated by dot (•) in Fig. 16 (17). The intrinsic structure of this band is also the $p_{//}$-type whose wf has the $S=1$ dominant component $(l\lambda)^{S=1}_L = (l1)^{S=1}_{L=0,2,4}$. It is noted, however, that the Λ particle does not always move around the t cluster, but moves in parallel with the α-t deformation axis. Further understanding of this feature can be achieved by comparing two kinds of spectroscopic factors leading to the α-${}^4_\Lambda H$ ad ${}^5_\Lambda He$-t decay channels. From Table XV we see that, in the ${}^8Be$-analog bands($S=0,\ 1$), the S-factor to the α-${}^4_\Lambda H$ channel is larger than the other in spite of the fact: $B^{cal}_\Lambda({}^4_\Lambda H) = 1.08$ MeV vs. $B^{cal}_\Lambda({}^5_\Lambda He) = 3.12$ MeV. Thus the simple picture mentioned above persists to characterize the band structures.

What characterizes the other two bands is the $p_\perp$-type intrinsic structure($K=1$) in which the last odd neutron in ${}^8Li = \alpha + t + n$ is substituted by the Λ particle. In Fig. 16 (17) we label the assigned members of these analog states with $S=0$ by triangle ($\triangle$) and those with $S=1$ by cross ($\times$).

Table V lists the Λ wf's in two typical states of ${}^8_\Lambda Li$.

4.1.2. Electromagnetic properties

Estimates of the reduced E2 transition probabilities $B(E2)$ are summarized in Fig. 16 (17) where some $B(M1)$ predictions are also given. Bedjidian et al.[7] reported the
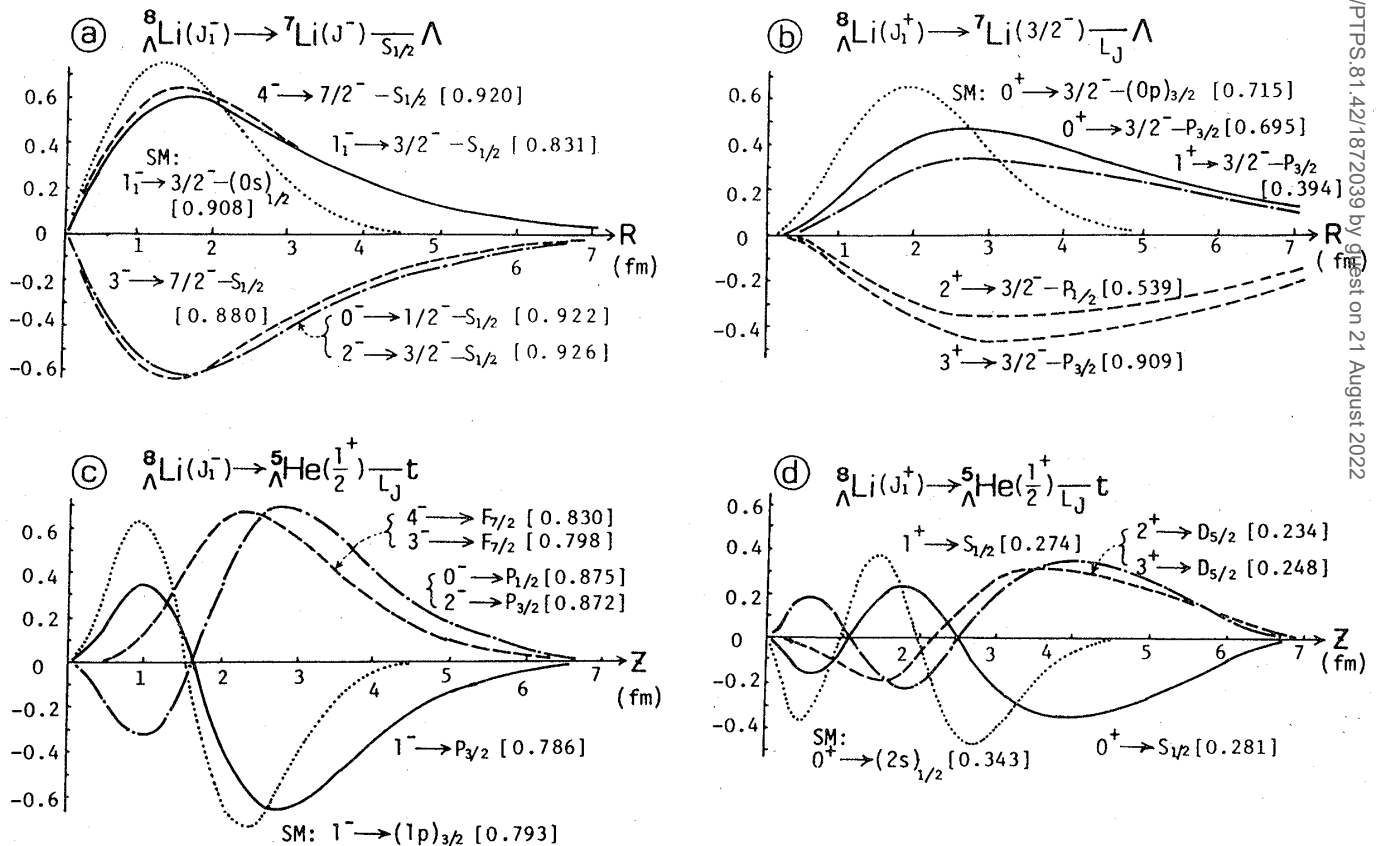

Fig. 18. RWA of ${}^8_\Lambda Li$. Comments as for Fig. 10.

observation of the 1.22 MeV γ ray from $^8_\Lambda$Li, suggesting the M1 transition of $1_2^- \to 1_1^-$. Here we get just the same energy difference 1.22 MeV for the transition. Being consistent with their suggestion, the M1 transition is predicted to occur more than 6 times faster than the E2 transition as listed in Table VII. Another possible transition $1_2^- \to 2^-$ is not likely to be the candidate for the observed γ ray because the energy difference turns out to be too small(0.64 MeV), although the obtained M1 transition rate is much stronger than the former (cf. Table VII). Both strong M1 transitions reflect the spin-flip process. The spin structures of the lowest four states are seen in the L-S coupling representation $(l, \lambda)^S_{\tilde{l}}$ as

$$|1_1^-\rangle = 88.9\%(1, 0)^0_{\tilde{l}} + 8.0\%(1, 0)^1_{\tilde{l}} + \cdots, \tag{4·4}$$

$$|2^-\rangle = 97.4\%(1, 0)^1_{\tilde{l}} + 1.4\%(1, 2)^1_{\tilde{l}} + \cdots, \tag{4·5}$$

$$|1_2^-\rangle = 7.9\%(1, 0)^0_{\tilde{l}} + 89.2\%(1, 0)^1_{\tilde{l}} + \cdots, \tag{4·6}$$

$$|0^-\rangle = 1.5\%(1, 2)^1_{\tilde{l}} + 97.1\%(1, 0)^1_{\tilde{l}} + \cdots. \tag{4·7}$$

See Fig. 15 for the j_x-j_Λ coupling wf's.

Compared with our shell model limit B(E2) values, the cluster model estimates are about 4(8) times enhanced in the negative (positive) parity states. The strong intra-band E2 cascades also support the above classification of the band structures. We also find from Fig. 9 that the α-t r.m.s. distance in each of the negative parity states in $^8_\Lambda$Li is more than 15 % contracted from that in ^{7}Li. This is responsible for the reduction, compared with ^{7}Li, of the B(E2) strengths of the transitions between the low-lying states.

The magnetic dipole moments of the ground states are calculated to be

$$\mu(^8_\Lambda\text{Li}; 1_1^-) = 0.367 \text{ nm} ,$$

$$\mu(^8_\Lambda\text{Be}; 1_1^-) = 1.052 \text{ nm} ,$$

for which the nuclear spin part contributions are opposite in sign (cf. Table VIII). Table IX lists B(E1) values predicted for some $J_i^+ \to J_f^-$ transitions. They do not differ so much from the Weisskopf unit value B(E1, ^{8}Li)$_{\text{wu}} = 0.036$ e^{2}fm^2.

4. 2. The hypernucleus $^7_\Lambda$Li

4. 2. 1. Structure characteristics

The calculated energy spectra of $^7_\Lambda$Li are shown in Fig. 19 with the dominant wf components and also in Fig. 20. As the $^5_\Lambda$He-d threshold energy is experimentally 3.94 MeV[43] above the ground state, we have four particle-stable bound states with B_Λ^{cal}(g.s.) being in good agreement with the experiment:

$$^7_\Lambda\text{Li}(1/2^+_{\text{g.s.}}): \quad B_\Lambda^{\text{cal}} = 5.59 \text{ MeV} \quad \text{vs.} \quad B_\Lambda^{\text{exp}} = 5.58 \text{ MeV}.[43]$$

The coupling

$$[^6\text{Li}(lj) \times s^\Lambda_{1/2}] \quad \text{with} \quad lj = S_1, D_3, D_2 \text{ and } D_1 ,$$

provides low-lying positive parity eight states:

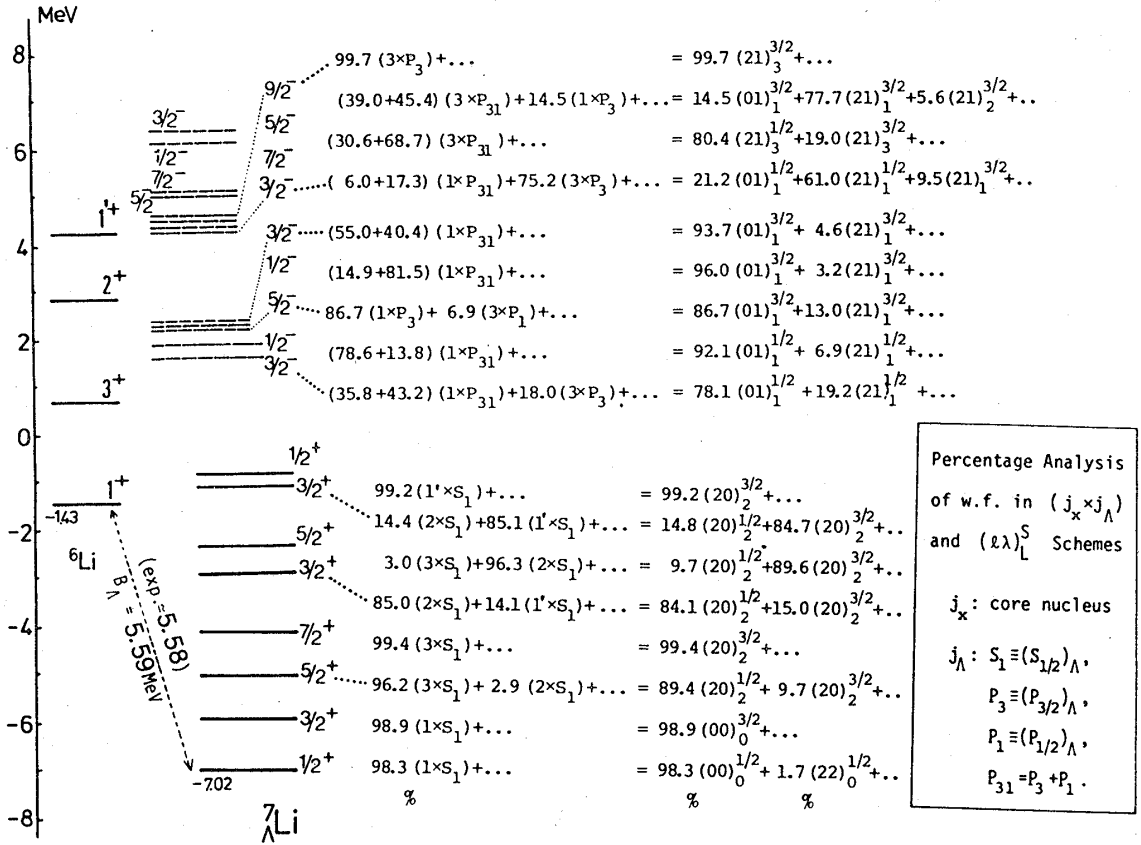$$1/2^+\text{-}3/2^+, 5/2^+\text{-}7/2^+, 3/2^+\text{-}5/2^+ \quad \text{and} \quad 3/2^+\text{-}1/2^+.$$

MeV

$99.7\,(3\times P_3)+\ldots = 99.7\,(21)_3^{3/2}+\ldots$

$(39.0+45.4)\,(3\times P_{31})+14.5\,(1\times P_3)+\ldots = 14.5\,(01)_1^{3/2}+77.7\,(21)_1^{3/2}+5.6\,(21)_2^{3/2}+\ldots$

$(30.6+68.7)\,(3\times P_{31})+\ldots = 80.4\,(21)_3^{1/2}+19.0\,(21)_3^{3/2}+\ldots$

$(6.0+17.3)\,(1\times P_{31})+75.2\,(3\times P_3)+\ldots = 21.2\,(01)_1^{1/2}+61.0\,(21)_1^{1/2}+9.5\,(21)_1^{3/2}+\ldots$

$(55.0+40.4)\,(1\times P_{31})+\ldots = 93.7\,(01)_1^{3/2}+4.6\,(21)_1^{3/2}+\ldots$

$(14.9+81.5)\,(1\times P_{31})+\ldots = 96.0\,(01)_1^{3/2}+3.2\,(21)_1^{3/2}+\ldots$

$86.7\,(1\times P_3)+6.9\,(3\times P_1)+\ldots = 86.7\,(01)_1^{3/2}+13.0\,(21)_1^{3/2}+\ldots$

$(78.6+13.8)\,(1\times P_{31})+\ldots = 92.1\,(01)_1^{1/2}+6.9\,(21)_1^{1/2}+\ldots$

$(35.8+43.2)\,(1\times P_{31})+18.0\,(3\times P_3)+\ldots = 78.1\,(01)_1^{1/2}+19.2\,(21)_1^{1/2}+\ldots$

^{6}Li

$B_\Lambda = 5.59\ \text{MeV}$ (exp=5.58)

-1.43

$99.2\,(1'\times S_1)+\ldots = 99.2\,(20)_2^{3/2}+\ldots$

$14.4\,(2\times S_1)+85.1\,(1'\times S_1)+\ldots = 14.8\,(20)_2^{1/2}+84.7\,(20)_2^{3/2}+\ldots$

$3.0\,(3\times S_1)+96.3\,(2\times S_1)+\ldots = 9.7\,(20)_2^{1/2}+89.6\,(20)_2^{3/2}+\ldots$

$85.0\,(2\times S_1)+14.1\,(1'\times S_1)+\ldots = 84.1\,(20)_2^{1/2}+15.0\,(20)_2^{3/2}+\ldots$

$99.4\,(3\times S_1)+\ldots = 99.4\,(20)_2^{3/2}+\ldots$

$96.2\,(3\times S_1)+2.9\,(2\times S_1)+\ldots = 89.4\,(20)_2^{1/2}+9.7\,(20)_2^{3/2}+\ldots$

$98.9\,(1\times S_1)+\ldots = 98.9\,(00)_0^{3/2}+\ldots$

$98.3\,(1\times S_1)+\ldots = 98.3\,(00)_0^{1/2}+1.7\,(22)_0^{1/2}+\ldots$

% % %

-7.02

$^7_\Lambda$Li

Percentage Analysis of w.f. in $(j_x \times j_\Lambda)$ and $(\ell\lambda)_L^S$ Schemes

j_x: core nucleus

j_Λ: $S_1 \equiv (S_{1/2})_\Lambda$,
$P_3 \equiv (P_{3/2})_\Lambda$,
$P_1 \equiv (P_{1/2})_\Lambda$,
$P_{31} = P_3 + P_1$.

Fig. 19. Calculated energy spectra of ^{6}Li and $^7_\Lambda$Li. Comments as for Fig. 15.

The weak coupling feature in the obtained 6 positive parity states is exhibited in the fact that each of them is well (96~99 %) described by a single configuration in the j_x-j_Λ representation (cf. Fig. 19). This reflects the fact that the energy level splittings in the ^{6}Li core[44] are too large for the ΛN interaction to give rise to sizable $\Delta l = 2$ couplings. In each doublet, the $\sigma_\Lambda \cdot \sigma_N$ interaction makes the member with the dominant $S_< = 1/2$ component lower in energy than the other with $S_> = 3/2$. Note that the sign of the ΛN spin-spin interaction is opposite to that of the NN case. The doublet splittings gradually decrease with their excitation energies, because the loosely bound Λ less feels the $\sigma_\Lambda \cdot \sigma_N$ interaction. The main features of the lowest four state wf's are as follows:

$$|1/2^+\rangle = 98.3\,\%\,(1^+ \times s_{1/2}^\Lambda) + \cdots = 98.3\,\%\,(0,0)_{L=0}^{S=1/2} + 1.7\,\%\,(2,2)_0^{1/2} + \cdots , \qquad (4\cdot8)$$

$$|3/2^+\rangle = 98.9\,\%\,(1^+ \times s_{1/2}^\Lambda) + \cdots = 98.9\,\%\,(0,0)_{L=0}^{S=3/2} + \cdots , \qquad (4\cdot9)$$

$$|5/2^+\rangle = 96.2\,\%\,(3^+ \times s_{1/2}^\Lambda) + 2.9\,\%\,(2^+ \times s_{1/2}^\Lambda) + \cdots$$
$$= 89.4\,\%\,(2,0)_{L=2}^{S=1/2} + 9.7\,\%\,(2,0)_2^{1/2}, \cdots , \qquad (4\cdot10)$$

$$|7/2^+\rangle = 99.4\,\%\,(3^+ \times s_{1/2}^\Lambda) + \cdots = 99.4\,\%\,(2,0)_{L=2}^{S=3/2} + \cdots . \qquad (4\cdot11)$$

For the other wf's see Fig. 19.

Very recently the 2.034 MeV γ ray was observed at BNL[10] and interpreted to come from the $5/2^+ \to 1/2^+$ transition. Our result for the transition energy is 1.99 MeV, which is just in good agreement with the experiment. Note that the present α-d model also reproduces the observed levels of the ^{6}Li core nucleus very well. The $5/2^+$-$1/2^+$ and

$7/2^+$-$3/2^+$ energy splittings are almost parallel to the corresponding nuclear 3^+-1^+ splitting(Cal: 2.13 MeV, Exp: 2.18 MeV[44]) but with a slight compression. This compression (Cal: 2.13→1.99 MeV, Exp: 2.18→2.034 MeV), though being slight, reflects the different responses of the 3^+ and 1^+ a-d wf's against the addition of the Λ particle.

Bunched energy levels are obtained for the negative parity states in which the Λ particle is dominantly in the p-state. The states in the lowest bunch are constructed from the coupling ^{6}Li$(1^+) \times \{p_{1/2}, p_{3/2}\}^{\Lambda}$, and those in the next bunch ^{6}Li$(3^+) \times \{p_{1/2}, p_{3/2}\}^{\Lambda}$, etc. The classification according to the intrinsic cluster structures given in Fig. 20($x = d$) is also approximately valid for these levels. Considering two possible spin values, the wf analysis allows one to rearrange them into the following four groups:

(i)   Spin-doublet $(S = 1/2)$ ^{7}Li-analog: $J = \{1/2^-, 3/2^-\}$, $\{5/2^-, 7/2^-\}$.

(ii) Spin-quartet $(S = 3/2)$ ^{7}Li-analog: $J = \{1/2^-, 3/2^-, 5/2^-\}$, $\{3/2^-, 5/2^-, 7/2^-, 9/2^-\}$.

(iii) Spin-doublet $(S = 1/2)$ ^{7}Li*-analog.

(iv) Spin-quartet $(S = 3/2)$ ^{7}Li*-analog.

Here we use the notation " ^{7}Li-" for the lowest four states in ^{7}Li describable with the $a + t$
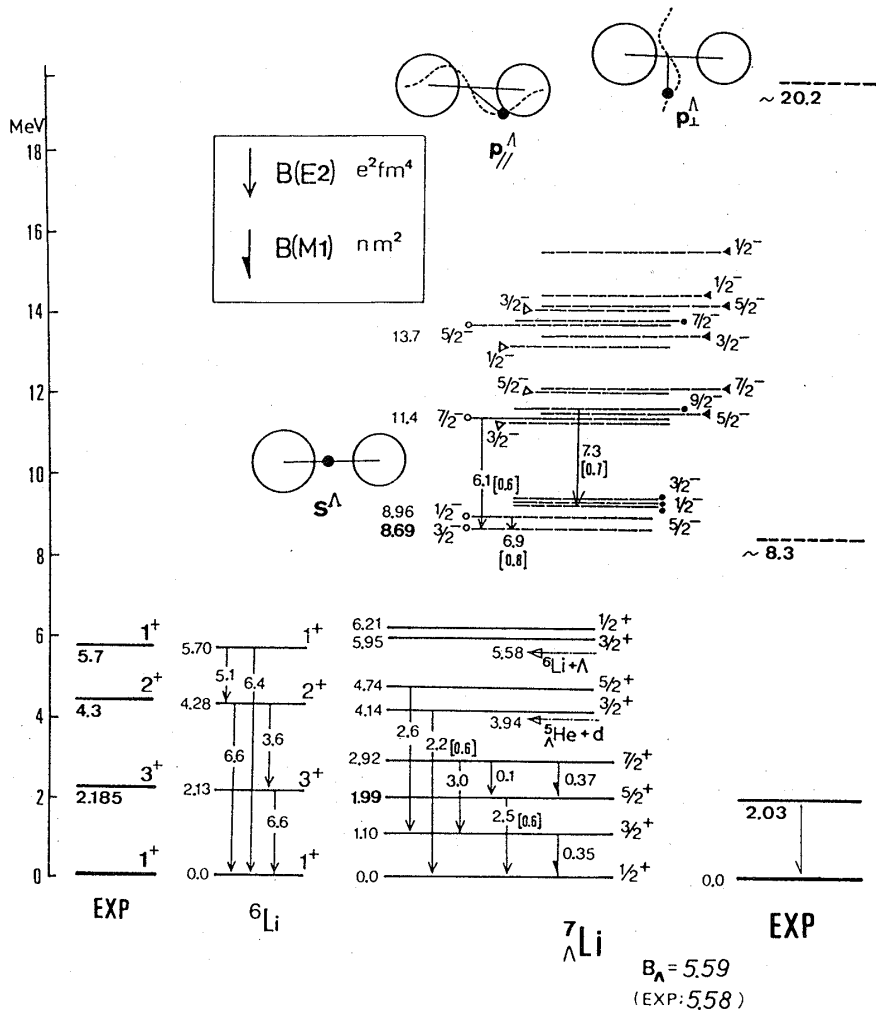
Fig. 20   Calculated B(E2) and B(M1) in ^{6}Li and ${}^{7}_{\Lambda}$Li.   The observed energies of ^{6}Li are from Ref. 44) and those of ^{7}Li from Refs. 4), 10) and 43).   Comments as for Fig. 16.

di-cluster and the notation "^{7}Li*-" for the other excited states having three-body structure such as $\alpha + d + n$. The spectrum of the first group, as marked by open circle($\circ$) in Fig. 20, is in fact analogous to the ^{7}Li $= \alpha + t$ spectrum but with some compression. Thus the spin-doublet ^{7}Li-analog could be simply regarded as having the $p_{//}$-type intrinsic structure. The second spectrum may have the $p_{//}$-type one with the coupling $[(L=1^+\&3^+)\times(S =3/2)]$. They are indicated by dot ($\bullet$) in Fig. 20. It should be remarked that nearly degenerate energies of these two groups having different spin values are one of the characteristics of hypernuclear spectra. The states belonging to the third and fourth groups appear at higher excitation energies.

In Table V are shown the h.o. expansion of the Λ-wf part of each dominant configuration for the $1/2^+_{g.s.}$ and $3/2^-$ (substitutional) states.

4. 2. 2.   (K^-, π^-) production rates

The Heidelberg-Saclay-Strasbourg Collaboration[1]~[6] found two large peaks at $B_\Lambda^{exp} = -2.7$ MeV and -14.6 MeV in the forward ^{7}Li(K^-, π^-)$^7_\Lambda$Li reaction. The other small peak at $B_\Lambda^{exp} = 5.6$ MeV corresponds to the $^7_\Lambda$Li ground state. The two strong peaks[4] have been ascribed to the substitutional configurations, respectively, in the shell-model version,

$$[(p_{3/2})_N^{-1}, (p_{3/2})_\Lambda] \quad \text{and} \quad [(s_{1/2})_N^{-1}, (s_{1/2})_\Lambda]$$

which are generated by the recoilless Λ-production. In the present investigation the large peak at $B_\Lambda^{exp} = -2.7$ MeV is identified with our $3/2_1^-$ level obtained at $B_\Lambda = -3.10$ MeV which is an analog of the target ground state ^{7}Li($3/2^-$g.s.). In fact the calculated excitation spectra $d\sigma(0°)/d\Omega$ shows an exclusively large production rate for the $3/2_1^-$ state, which supports such interpretation (cf. Fig. 21). The $3/2_3^-$ state of the $S=1/2$ ^{7}Li*-analog should be sizably excited, but the corresponding peak has not been identified probably due to the experimental resolution.
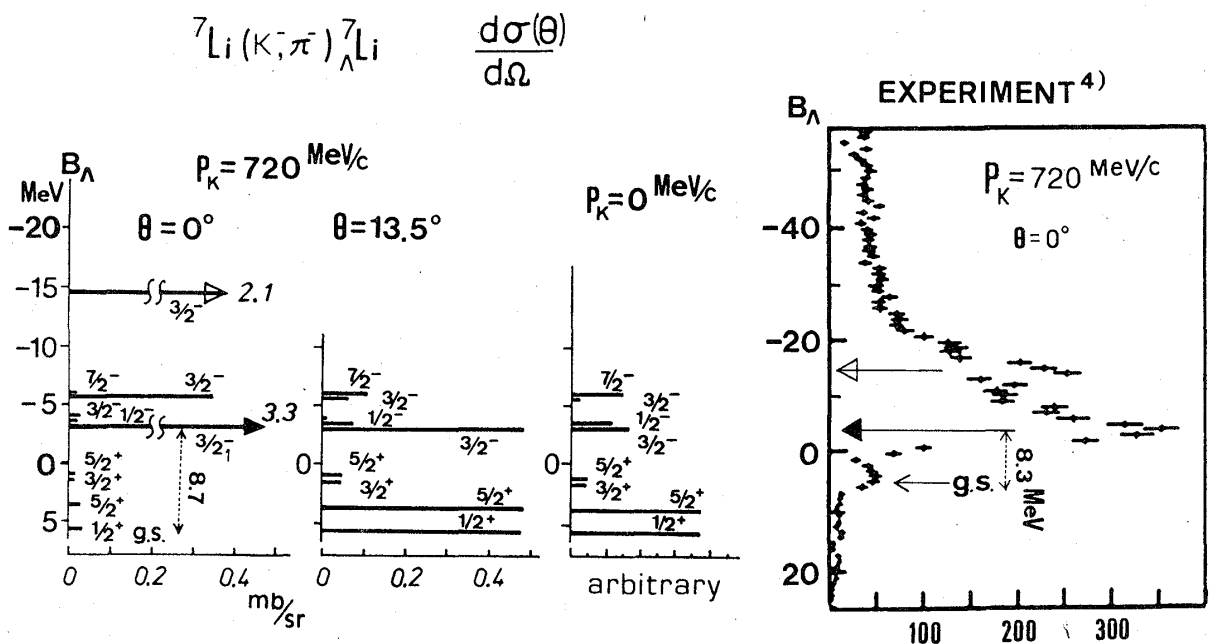

Fig. 21. Calculated excitation spectra $d\sigma(\theta)/d\Omega$ of the ^{7}Li(K^-, π^-)$^7_\Lambda$Li reactions with $p_K = 720$ MeV/c ($\theta = 0°$ & 13.5°) and $p_K = 0$. The $\theta = 0°$ observed spectrum[4] is compared.

Description of the other large peak involves the new configuration with a neutron-hole in the α cluster. For this peak, the effective neutron number ($\theta=0°$) for the substitutional processes $((g)_N \rightarrow (g)_A$ and $(u)_N \rightarrow (u)_A)$ is evaluated with the aid of the molecular orbital model.[50] Including this estimate, the calculated $N_{eff}(0°)$ leading to the main states are listed in Table VI. Thus the production rates for the ground state and the two big peaks are estimated as

$$\frac{7}{\Lambda}\text{Li}: \quad \frac{d\sigma}{d\Omega}(0°) = \begin{cases} 0.04 \text{ mb/sr}, & (1/2^+, B_\Lambda^{exp}=5.58 \text{ MeV}) \\ 3.3 \text{ mb/sr}, & (3/2_1^-, \quad -2.7 \text{ MeV}) \\ 2.1 \text{ mb/sr}, & (3/2^-, \quad -14.6 \text{ MeV}) \end{cases}$$

where the empirical value[48] $(d\sigma(0°)/d\Omega)_{K^- n \rightarrow \Lambda \pi^-} = 3.7$ mb/sr is used for the free space process. The second resonance is populated, theoretically, about 1.5 times as strongly as the third peak, which ratio nicely corresponds to the experimental one.[4]

It should be noted that the $1/2^+$ and $5/2^+$ states are expected to be as strongly populated as the substitutional $3/2_1^-$ state when observed at $\theta=12°-15°$. They are selectively excited in the (K^-, π^-) reaction, since the wf's are dominated by the $S_< = 1/2$ as shown by Eqs. (4·8) and (4·10). Figure 22 displays the overall behaviors of the pion angular distributions. In Fig. 21 is also shown the excitation spectra with $p_K=0$ MeV/c which give the relative ratios of the stopped K^- absorption rates. Therefore several new
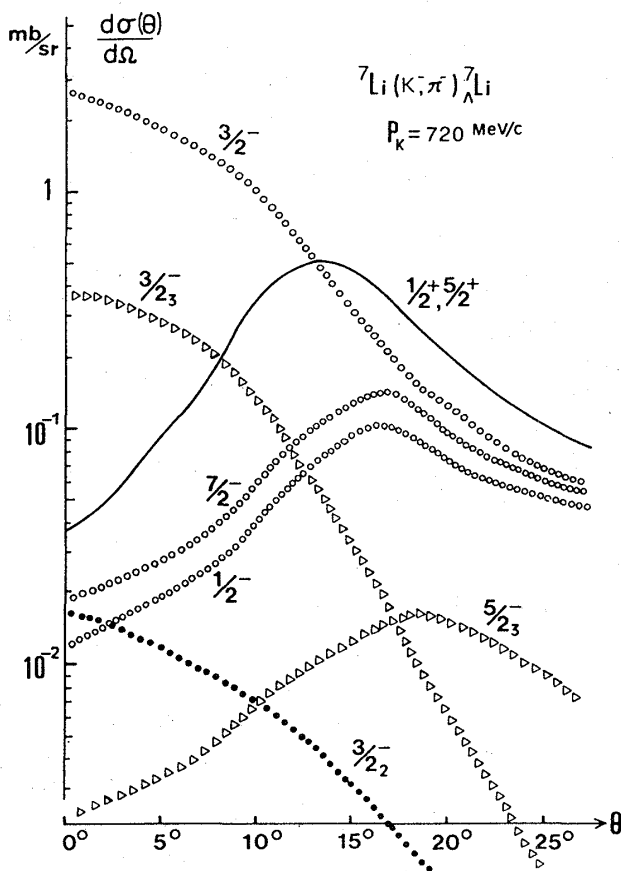

Fig. 22. Calculated angular distributions $d\sigma(\theta)/d\Omega$ (in Lab.) of the pion from the $^7\text{Li}(K^-, \pi^-)^7_\Lambda\text{Li}(J_f)$ reactions.
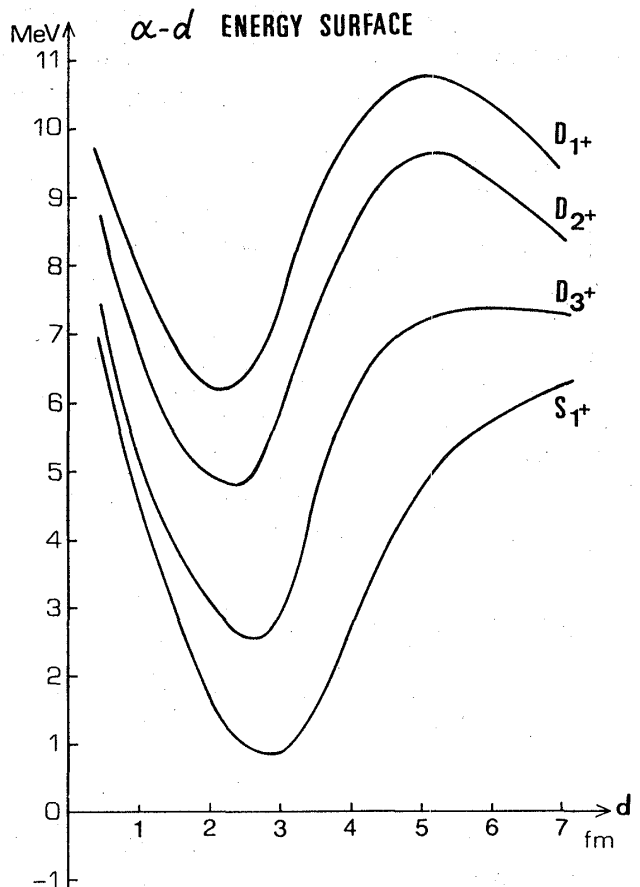

Fig. 23. Calculated energy surfaces for the low-lying states (lj^π) in ^{6}Li. The value $H_{lj}(d, d)$ $/ N_l(d, d)$ of Eq. (2·6) is plotted as a function of the α-d distance d.

states are expected to be observed in appropriate experimental conditions.

4.2.3. Electromagnetic properties

The calculated $B(E2)$ values are displayed in Fig. 20, which support, as a whole, the classification of the spectra discussed above. From typical $B(E2)$ estimates we see that the enhancements with respect to the shell-model limit are about 3(8) times in the positive (negative) parity states. In §4.2.1 we have seen that the γ-ray energy 2.034 MeV agrees remarkably with the calculated energy difference $5/2^+ \rightarrow 1/2^+$ (cf. Table VII).

$$E_\gamma^{cal}(5/2^+ \rightarrow 1/2^+) = 1.99 \text{ MeV} \quad \text{vs.} \quad E_\gamma^{exp} = 2.034 \pm 0.023 \text{ MeV.}^{[10a]}$$

Dalitz and Gal[18] deduced the E2 transition rates for $5/2^+ \rightarrow 3/2^+$ and $5/2^+ \rightarrow 1/2^+$ on the assumption that both uniquely involve the core transition $^6Li(3^+ \rightarrow 1^+)$ observed[44] with the rate $T(E2) = 6.7 \times 10^{11}$ sec. Their values are very large in comparison with ours:

$$B(E2; 5/2^+ \rightarrow 3/2^+) = 0.4 \ e^2fm^4, \quad (\text{D-G:} \quad 3.1 \ e^2fm^4)$$

$$B(E2; 5/2^+ \rightarrow 1/2^+) = 2.5 \ e^2fm^4. \quad (\text{D-G:} \quad 8.6 \ e^2fm^4)$$

This difference arises because the dynamical contraction of the α-d distance due to the addition of the Λ particle is naturally taken into account here. The nuclear response such as the contraction can be explained as the competition between the energy gain due to the ΛN interaction and the energy loss due to deviation from the minimum in the α-d energy surface shown in Fig. 23. The energy compression $(5/2^+$-$1/2^+)$ discussed in §4.2.1 is an example of the state dependence of the nuclear response. The contraction effect, as
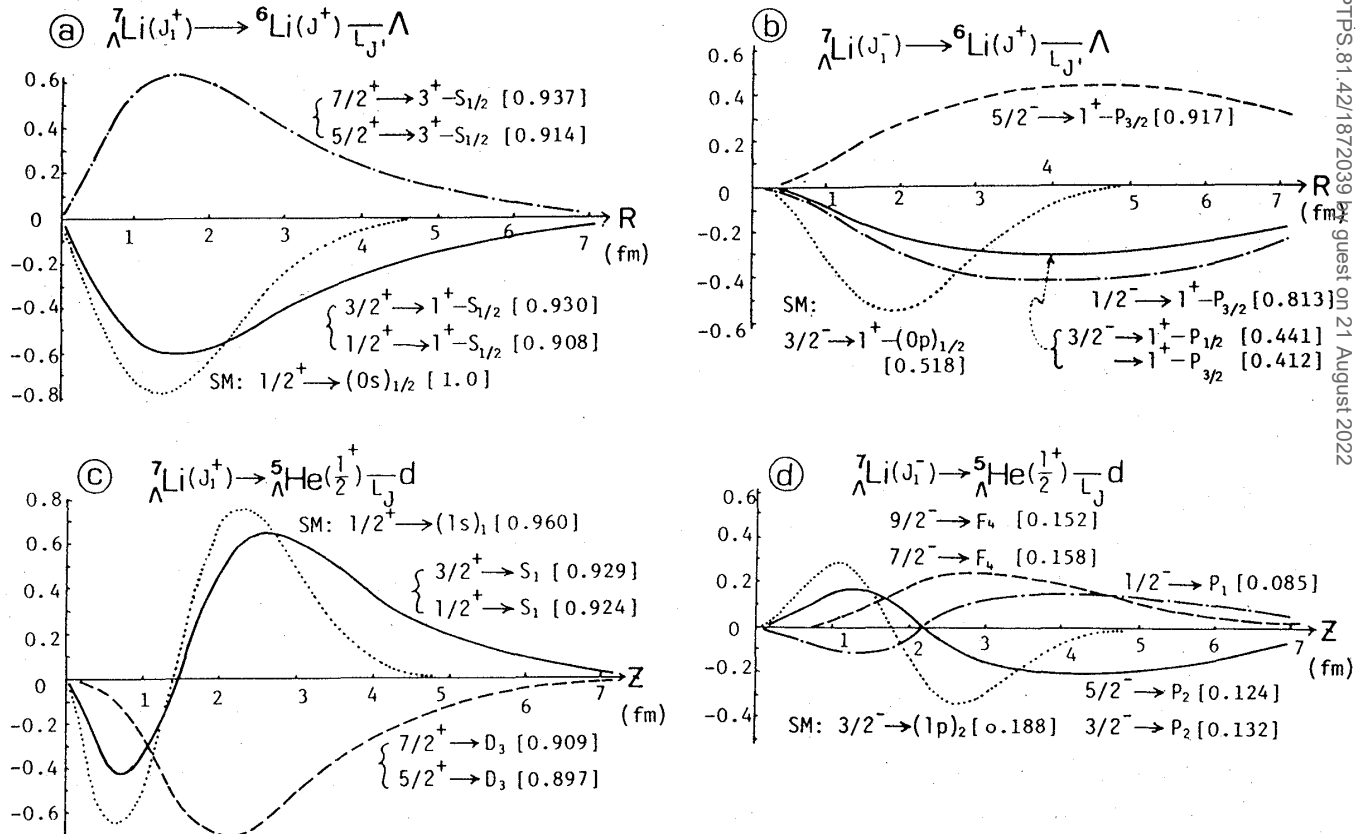
Fig. 24. RWA of $^7_\Lambda$Li. Comments as for Fig. 10.

shown in Fig. 9, is so remarkable as to reduce the hypernuclear B(E2) values to nearly half the core nuclear ones. On the other hand, our B(E2) predictions are underestimated, since the present ^{6}Li wf's yield B(E2; $3^+ \to 1^+$) $=6.6$ e^{2}fm^4 without additional effective charge while 11.0 e^{2}fm^4 experimentally.[44] The additional effective charge 0.27e is necessary for the remedy. Thus the reasonable B(E2) values in $^7_\Lambda$Li should be nearly 1.5 times the values shown in Fig. 20.

For M1 transitions we obtain

$$B(M1; 3/2^+ \to 1/2^+) = 0.352 \text{ nm}^2, \quad (\text{D-G:} \quad 0.364 \text{ nm}^2)$$

$$B(M1; 7/2^+ \to 5/2^+) = 0.365 \text{ nm}^2.$$

Generally these M1 spin-flip transitions are strong. They are possibly observed, for example, through the ^{7}Be(e, e'K$^+$)$^7_\Lambda$Li experiment, because the reaction favors the spin-flip process to populate the $3/2^+$ (and $7/2^+$) state with the $S_> = 3/2$ dominant wf. The magnetic dipole moment of the ground state is calculated to be

$$\mu(^7_\Lambda\text{Li}; 1/2^+) = 0.791 \text{ nm}$$

for which the divided contributions are listed in Table VIII. The present estimates of the electromagnetic transition rates result in the lifetimes:

$$\tau(3/2^+) = 1.2 \times 10^{-13} \text{ sec},$$

$$\tau(5/2^+) = 1.8 \times 10^{-11} \text{ sec},$$

$$\tau(7/2^+) = 1.6 \times 10^{-13} \text{ sec},$$

which are all shorter than the weak decay lifetime of the free Λ particle.

Table IX lists the estimates of B(E1) from the negative parity states of $^7_\Lambda$Li. We see that the E1 transitions occur selectively for the spin-doublet $\{1/2^-, 3/2^-\} \to 1/2^+$ and the spin-quartet $\{1/2^-, 3/2^-, 5/2^-\} \to 3/2^+$ due to their spin characters. A typical magnitude is B(E1; $3/2^- \to 1/2^+$) $=0.084$ e^{2}fm^2.

4.2.4. Reduced width amplitudes and particle-decay widths

The RWA and the spectroscopic factors are calculated for the decay processes $^7_\Lambda$Li $\to$ ^{6}Li-Λ and $^7_\Lambda$Li $\to$ $^5_\Lambda$He-d as shown in Fig. 24. The behaviors of the RWA differ significantly from the corresponding shell model ones, even when the S-factors do not differ so much. The partial decay widths from the substitutional $3/2_1^-$ state are shown in Fig. 11 and Table X, from which we get a rough estimate for the width of the big peak at $B_\Lambda^{\text{exp}} = -2.7$ MeV,[4]

$$^7_\Lambda\text{Li}(3/2_1^-): \quad \Gamma = 3.22 \text{ MeV}.$$

According to the experience on the $^9_\Lambda$Be case (cf. §§3.4 and 6), this may be a reasonable estimate. The experimental width to be compared has not been clearly deduced.[3],[4] Note that the shell model wf gives an extremely small width for the peak.

4.3. *The hypernuclei $^5_\Lambda$He and $^6_\Lambda$Li*

4.3.1. Energy spectra

Calculated energy spectra of $^5_\Lambda$He($^6_\Lambda$Li) are shown in Figs. 25 and 26. Here we simply

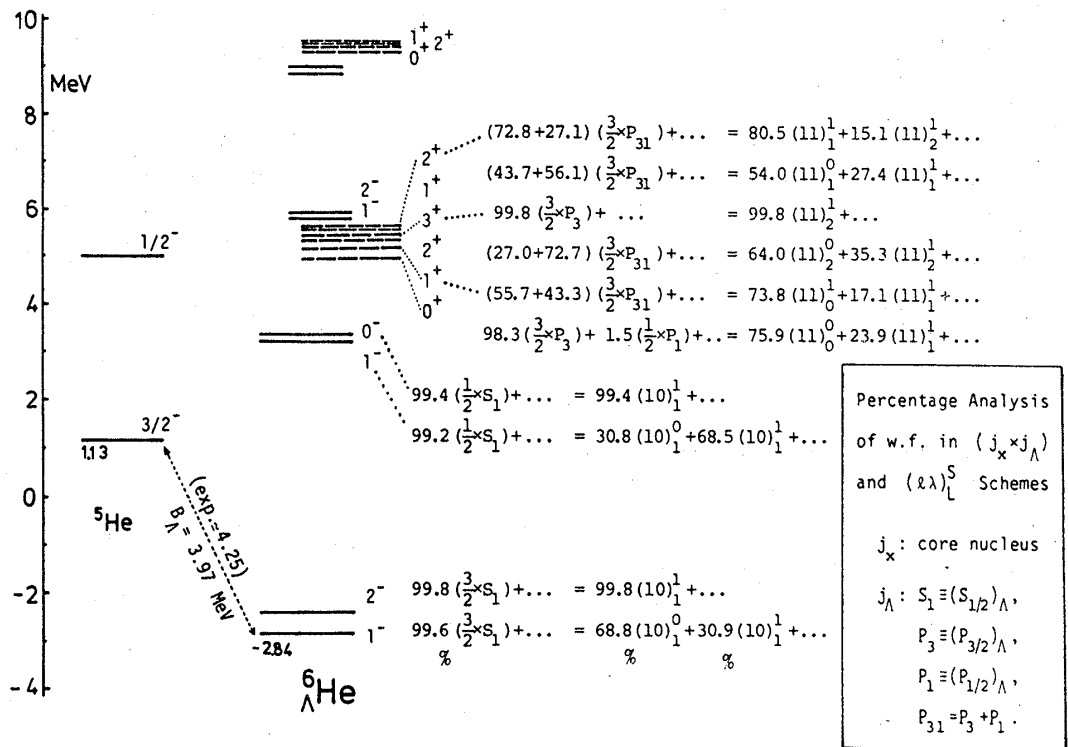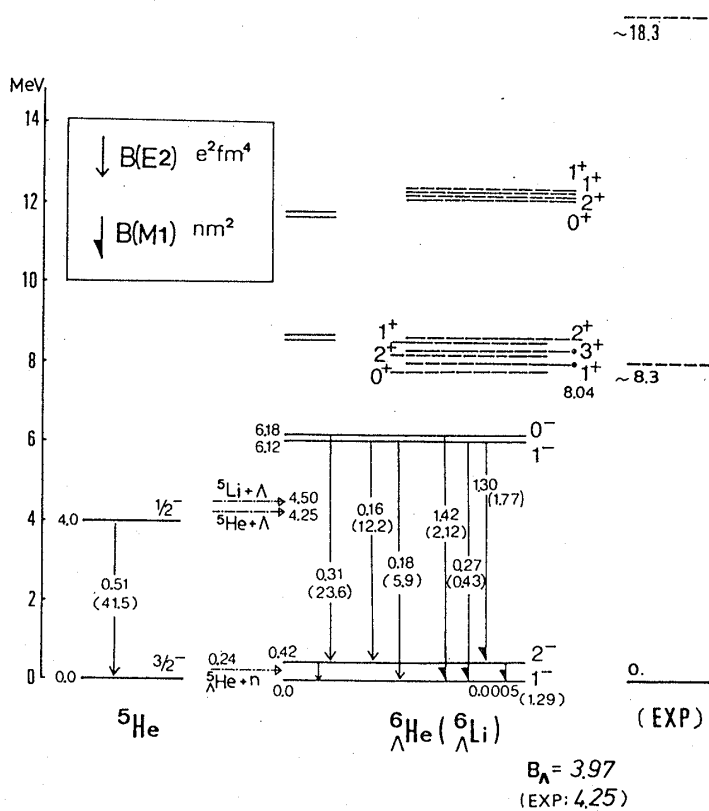Fig. 25. Calculated energy spectra of ^{5}He and $^6_\Lambda$He($^6_\Lambda$Li). Comments as for Fig. 15.

Fig. 26. Calculated B(E2) and B(M1) in ^{5}He(^{5}Li) and $^6_\Lambda$He($^6_\Lambda$Li). Comments as for Fig. 16.

assume the same wf for both $^6_\Lambda$He and $^6_\Lambda$Li, as the present ΛN interaction includes no charge-symmetry-breaking terms.

The lowest states of the core nucleus ^{5}He(^{5}Li) are $3/2^-$ and $1/2^-$, which are both unbound resonances. The addition of the s-state Λ particle generates two negative parity doublets:

$$1^- \text{-} 2^-: \quad [\alpha N(3/2^-) \times s^\Lambda_{1/2}],$$

$$0^- \text{-} 1^-: \quad [\alpha N(1/2^-) \times s^\Lambda_{1/2}],$$

which, according to the calculation, remain almost purely as the eigenstates. The order of the doublet levels is simply determined by their spin structures, because the $\sigma_\Lambda \cdot \sigma_N$ term acts attractively (repulsively) in the $S_< = 0$ ($S_> = 1$) state. See Fig. 25 for the L-S coupling representation of the obtained wf's. In both 1^- states we see considerable admixture of $S_< = 0$ and $S_> = 1$ components. The Λ particle binding energy in the ground state is calculated to be $B_\Lambda = 3.97$ MeV, which is somewhat
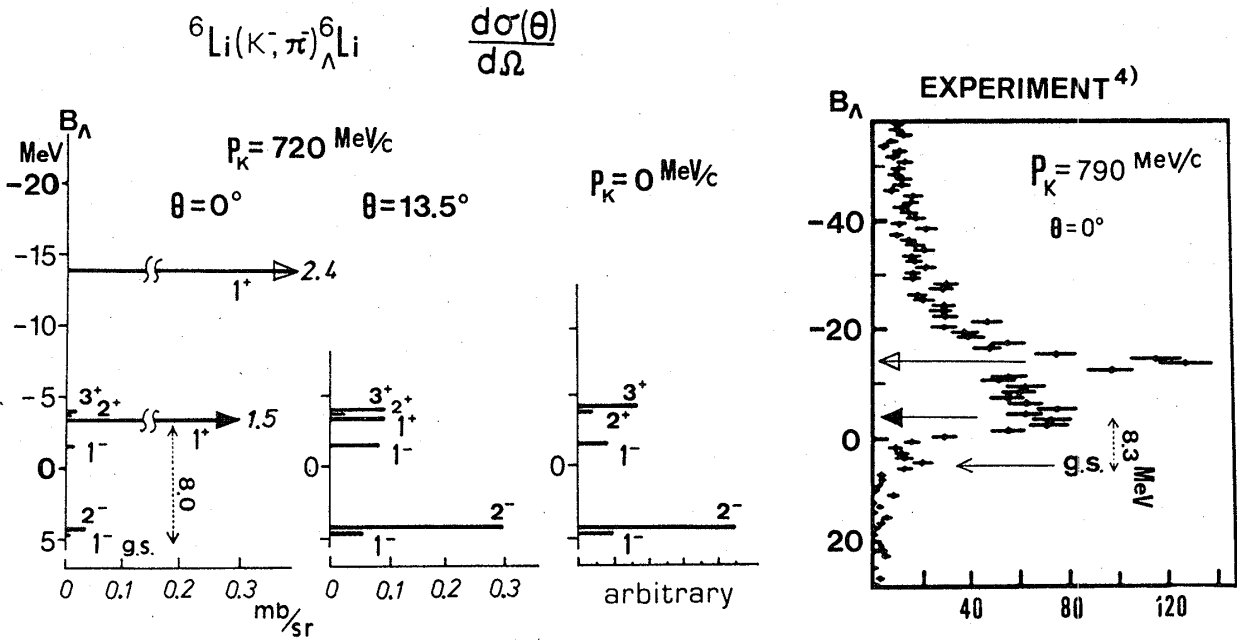
Fig. 27. Calculated excitation spectra $d\sigma(\theta)/d\Omega$ of the $^6\text{Li}(K^-, \pi^-)^6_\Lambda\text{Li}$ reactions with $p_K = 720$ MeV/c ($\theta = 0°$ and $13.5°$) and $p_K = 0$. The $\theta = 0°$ observed spectrum[4] is compared.

underestimated in comparison with the observed value $B_\Lambda^{exp} = 4.25$ MeV in $^5_\Lambda\text{He}$ (4.50 MeV in $^6_\Lambda\text{Li}$).[43] This seems to be due to the limited model space adopted in treating such weakly bound state, since the present "x-cluster" is a nucleon itself and the adopted coordinate in Fig. 2(b) may not always be the best one.
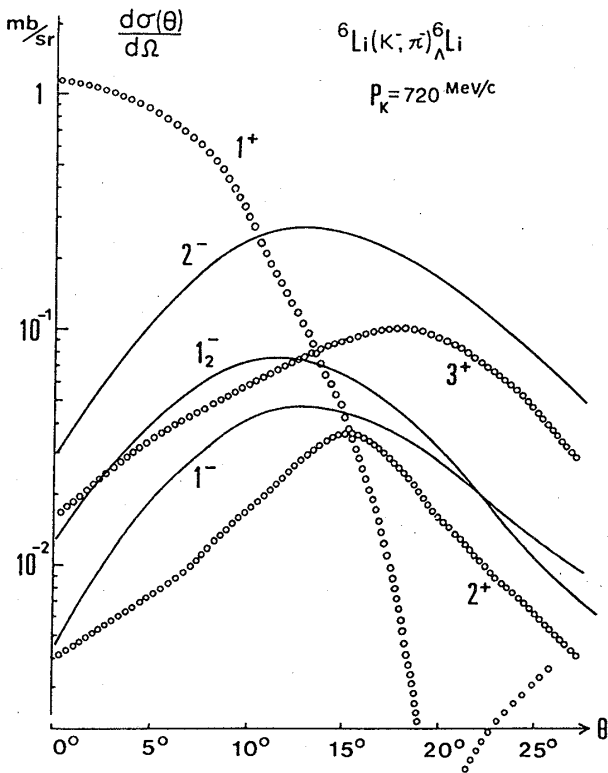

Fig. 28. Calculated angular distributions $d\sigma(\theta)/d\Omega$ (in Lab.) of the pion from the $^6\text{Li}(K^-, \pi^-)^6_\Lambda\text{Li}(J_f)$ reactions.

Available configurations for low-lying positive parity states are, in the L-S coupling,

$$[aN(l=1) \times \Lambda(\lambda=1)]^S_L,$$

which generate two 0^-, four 1^-, three 2^- and one 3^- states. As seen in Fig. 25(or 26), six of them are centered around 8 MeV excitation. Their wf's are fragmented over the possible j_x-j_Λ coupling components, but indicating the recovered spatial symmetries as can be seen from the L-S coupling representation. The correspondents to the $^6\text{He}(0^+, 2^+)$ and $^6\text{Li}(1^+, 3^+)$ states are found in the lower group. However such an analog picture does not always work well in this case. The effect of the large spin-orbit potential in $^5\text{He}(^5\text{Li})$ remains as sizable mixings of different (L, S) components.

4. 3. 2. (K^-, π^-) production rates of $^6_\Lambda\text{Li}$

Figures 27 and 28 show the calculated cross sections for the $^6\text{Li}(K^-, \pi^-)^6_\Lambda\text{Li}$ reac-

tion. The forward cross section is exclusively dominated by the 1^+ state obtained at B_A $=-4.07$ MeV. This is in good correspondence with the lower strong peak (broad resonance) observed at $B_A^{exp}=-3.8$ MeV.[3),4)] Note that this 1^+ state does not have the simple shell-model substitutional structure as $(p_{3/2})_N^{-1}(p_{3/2})_A$ but has the following character in the cluster-model space,

$$|1^+\rangle = 55.7\,\%\,[3/2^-\times p_{3/2}^A] + 43.3\,\%\,[3/2^-\times p_{1/2}^A] + 0.8\,\%\,[1/2^-\times p_{3/2}^A] + \cdots. \qquad (4\cdot12)$$

According to the prediction of the angular distributions, production rates of the other several states, especially 2^-, grow up at $\theta=10°\sim15°$. We see the similar feature in the $p_K=0$ MeV/c excitation function. Another strong, narrow resonance peak at B_A^{exp} $=-13.8$ MeV[3),4)] can be described by breaking the α cluster to produce a neutron hole. The molecular orbital model allows us a rough evaluation of the forward cross section to this peak. Thus the production rates for the ground state and two big resonance states are

$$_A^6\text{Li}: \quad \frac{d\sigma}{d\Omega}(0°) = \begin{cases} 0.007 \text{ mb/sr}, & (\ 1^-, B_A^{exp}=\ \ 4.50 \text{ MeV}) \\ 1.5 \ \ \text{mb/sr}, & (\ 1^+, \qquad\quad -3.8\ \ \text{MeV}) \\ 2.4 \ \ \text{mb/sr}. & ((1^+), \qquad -13.8\ \ \text{MeV}) \end{cases}$$

It should be noted that the latter two theoretical values can well explain the observed production ratio of the two big peaks.[3),4)]
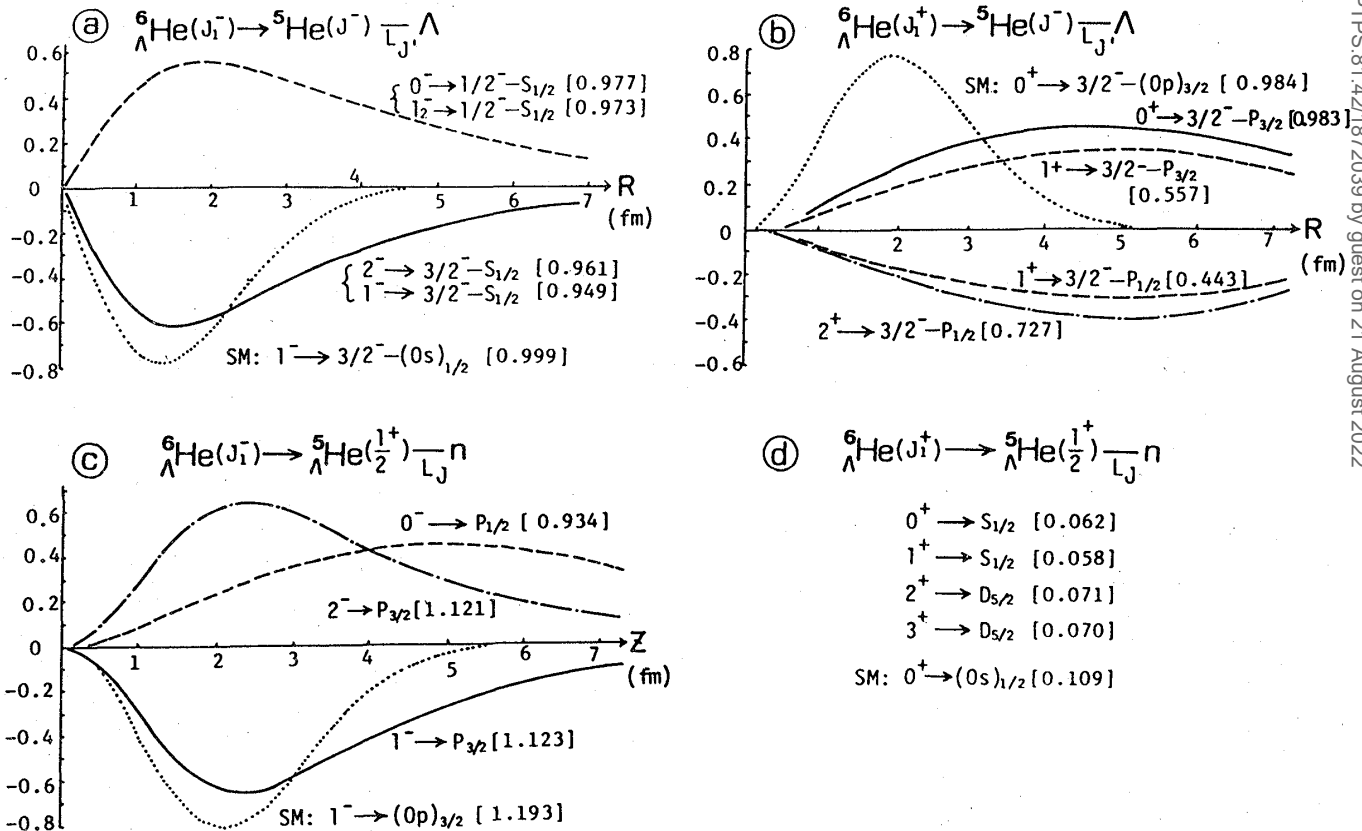
4.3.3. Electromagnetic properties

Fig. 29. RWA of $_A^6$He($_A^6$Li). Comments as for Fig. 10.

In Fig. 26 we summarize the calculated B(E2) and B(M1) values. The transition rates between the lowest two states of $^6_\Lambda$He (in the parenthesis for $^6_\Lambda$Li) are

$$T(\text{E2}; 2^- \to 1^-) = 3.67 \times 10^6 \text{ sec}^{-1} \quad (2.71 \times 10^7 \text{ sec}^{-1}),$$

$$T(\text{M1}; 2^- \to 1^-) = 6.52 \times 10^8 \text{ sec}^{-1} \quad (1.68 \times 10^7 \text{ sec}^{-1}).$$

The theoretical ground state magnetic moment is given in Table VIII. Table IX includes some B(E1) estimates.

4. 3. 4. Reduced width amplitudes and particle-decay width

Figure 29 illustrates the bahaviors of the RWA and spectroscopic factors leading to the indicated two-body decay channels. The calculated partial decay widths are shown in Fig. 11, from which we estimate the total width for the strong peak observed at $B_\Lambda^{\text{exp}} = -3.8$ MeV in the ^{6}Li(K^-, π^-)$^6_\Lambda$Li reaction:[1]~[5]

$$^6_\Lambda\text{Li}(1^+): \quad \Gamma = 3.22 \text{ MeV} .$$

This value is also regarded to give a reasonable estimate of the peak width.

§ 5. The π-mesic decay

The dominant decay modes of the free Λ particle are the non-leptonic processes:

$$\Lambda \longrightarrow \begin{cases} p + \pi^- + 37.8 \text{ MeV} , & (64.2\%) \\ n + \pi^0 + 41.1 \text{ MeV} , & (35.8\%) \end{cases} \tag{5.1}$$

where the experimental branching ratio is in the parentheses. The free Λ lifetime is

$$\tau_\Lambda = 2.63 \times 10^{-10} \text{ sec.} \tag{5.2}$$

In the decay the emerging pion receives about 36 MeV of energy corresponding to the released momentum

$$q_0 \cong 100 \text{ MeV}/c \tag{5.3}$$

in the center-of-mass frame. As the momentum of the recoiling nucleon ($q_N = q_0$) is only about 1/3 of the nuclear Fermi momentum ($k_F \simeq 280$ MeV/c), the π-mesic decay rates are expected to be strongly suppressed in nuclei due to the Pauli exclusion principle.[52],[53] On the other hand, the non-mesic decay which can take place only in the nucleus becomes a dominant mode in heavier hypernuclei,

$$\Lambda + N \longrightarrow N + N + 176 \text{ MeV} \quad (q_N \cong 400 \text{ MeV}/c). \tag{5.4}$$

In this chapter, however, we confine ourselves to the π-mesic decay of the Λ-hypernuclei with an intension of using it as a spectroscopic tool.

First we calculate the partial decay rates leading to the low-lying daughter states:

$$^6_\Lambda\text{Li}(1^-\text{g.s.}) \xrightarrow{\pi^0} {}^6\text{Li}(J_f) , \tag{5.5a}$$

$$^7_\Lambda\mathrm{Li}(1/2^+\mathrm{g.s.}) \xrightarrow{\pi^0} {}^7\mathrm{Li}(J_f), \qquad (5\cdot5\mathrm{b})$$

$$\pi^- \searrow {}^7\mathrm{Be}(J_f), \qquad (5\cdot5\mathrm{c})$$

$$^8_\Lambda\mathrm{Li}(1^-\mathrm{g.s.}) \xrightarrow{\pi^-} {}^8\mathrm{Be}(J_f). \qquad (5\cdot5\mathrm{d})$$

Secondly, in these decays, we predict the angular distributions of the pion emitted from the polarized hypernuclear ground states.

5.1. Expressions

The π-mesic decay Hamiltonian is expressed as[54]

$$H_\pi = s_\pi + p_\pi(\boldsymbol{\sigma}\cdot\boldsymbol{q})/q_0, \qquad (5\cdot6)$$

where $\boldsymbol{\sigma}$ represents the $\Lambda(N)$ spin operator and $\boldsymbol{q}$ the pion momentum. The s_π and p_π denote the parity-violating spin-nonflip and parity-conserving spin-flip interactions, respectively. Here we use the following values:

$$\pi^-\text{-decay}\begin{cases} s_- = 0.96\times10^{-7}, \\ p_- = -0.32\times10^{-7}, \end{cases} \pi^0\text{-decay}\begin{cases} s_0 = s_-/\sqrt{2}, \\ p_0 = p_-/\sqrt{2}. \end{cases} \qquad (5\cdot7)$$

The π-mesic decay probability T_π of a Λ-hypernucleus $(^A_\Lambda Z)$ to a daughter nucleus $(^A Z')$ is defined with the relevant wf's as

$$T_\pi(i,f;q) = \frac{1}{[J_i]}\sum_{M_iM_f}\left|\sqrt{A}\int\Psi(^A Z'; J_fM_fT_f\tau_f)H_\pi\theta_\pi e^{iqx}\Psi(^A_\Lambda Z; J_iM_iT_i\tau_i)d\xi_1\cdots d\xi_{A-1}dx\right|^2_{\mathrm{av}.\hat{q}}, \qquad (5\cdot8)$$

where, averaging over the pion direction, the integration is carried out with respect to all the nucleon and Λ coordinates. The operator θ_π transforms Λ to a nucleon:

$$\theta_\pi|\Lambda\rangle = \begin{cases} |p\rangle \\ |n\rangle \end{cases} \text{for} \begin{cases} \pi^-\text{-decay}, \\ \pi^0\text{-decay}. \end{cases} \qquad (5\cdot9)$$

With the multipole expansion of the sandwitched operator, we get

$$T_\pi(i,f;q) = \frac{4\pi}{[J_i]}\sum_K\left|\sqrt{A}\langle\Psi(^A Z'; J_fT_f\tau_f)\|F_K^{(s)}\theta_\pi + F_K^{(p)}\theta_\pi\|\Psi(^A_\Lambda Z; J_iT_i\tau_i)\rangle\right|^2, \qquad (5\cdot10)$$

$$F_K^{(s)} = s_\pi j_K(qx)Y_K(\hat{x}), \qquad (5\cdot11)$$

$$F_K^{(p)} = -p_\pi(q/q_0)\sum_{k=K\pm1}(-i)^{k-K}(10K0|k0)j_k(qx)[\boldsymbol{\sigma}\times Y_k(\hat{x})], \qquad (5\cdot12)$$

where $j_K(x)$ is the spherical Bessel function. In the $\alpha+x+\Lambda$ microscopic cluster model, the initial hypernuclear wf is represented by Eq. (2·18) where the isospin quantum numbers $(T_i\tau_i)$ are implicit in $\hat{\Phi}^{\alpha x}(Nl)$. On the other hand, the final state wf of the $\alpha+(x+1)$ nucleus is given in the form of Eq. (2·35). The expressions of the matrix elements of F_K with these wf's are given in Appendix C. Thus the decay probability of Eq. (5·10) is divided into the s-wave and p-wave contributions and can be expressed in the form

$$T_\pi = s_\pi^2 S(s) + p_\pi^2 S(p). \qquad (5\cdot13)$$

Note that the $i\to f$ transitions with (without) parity-change are induced by the odd (even)-

K terms of $F_K^{(s)}$ and the even(odd)-K terms of $F_K^{(p)}$.

With the $T_\pi(i, f; q)$ of Eq. (5·10) the decay rate R_π is expressed by

$$R_\pi = \frac{2q}{1+(\omega_q/M_A)} T_\pi(i, f; q) , \tag{5·14}$$

$$\omega_q = \sqrt{m^2 + q^2} . \tag{5·15}$$

Here the pion energy ω_q and momentum q are determined by the energy conservation condition as

$$M_A + \varepsilon_A = M_N + \varepsilon_N + \frac{q^2}{2M_A} + \omega_q , \tag{5·16}$$

$$\varepsilon_A = E(^A_A Z; \text{ g.s.}) - E(^{A-1}Z; \text{ g.s.}) , \tag{5·17}$$

$$\varepsilon_N = E(^A Z'; J_f) - E(^{A-1}Z; \text{ g.s.}) . \tag{5·18}$$

The π-mesic decay rate of the free Λ is analogously expressed by

$$\text{free } \Lambda: \quad R_\pi^0 = \frac{2q_0}{1+(\omega_{q_0}/M_N)}(s_\pi^2 + p_\pi^2) , \tag{5·19}$$

$$R_\Lambda^{\text{free}} = R_{\pi^-}^0 + R_{\pi^0}^0 = 1/\tau_\Lambda = 3.8 \times 10^9 \text{ decays/ sec} . \tag{5·20}$$

By comparing Eqs. (5·13) and (5·14) with Eq. (5·19), $S(s)$ and $S(p)$ are interpreted as the suppression factors[52],[53] which reflect the effect of the Pauli principle, kinematical selection rules and structure differences between parent and daughter systems.

Another interesting quantity is the angular distribution of the pion emitted from the polarized hypernuclear ground state. Choosing a particular intial state $|J_i M_i T_i \tau_i\rangle$ without M_i-averaging in Eq. (5·8), we define the transition probability $T_\pi(J_i M_i, J_f; \boldsymbol{q})$ which depends on the angle Ω_q of the emitted pion,

$$T_\pi(J_i M_i, J_f; \boldsymbol{q}) = \frac{4\pi}{\sqrt{[J_i]}}(-)^{J_f - J_i} \Bigg[\sum_{K+K'=\text{even}} (-)^{(K-K')/2}\sqrt{[K][K']}$$

$$\times \{\langle J_f\|F_K^{(s)}\|J_i\rangle\langle J_f\|F_{K'}^{(s)}\|J_i\rangle + \langle J_f\|F_K^{(p)}\|J_i\rangle\langle J_f\|F_{K'}^{(p)}\|J_i\rangle\}\mathscr{P}(K,K'; \hat{\boldsymbol{q}})$$

$$- \sum_{K+K'=\text{odd}} (-)^{(K-K'+1)/2}\sqrt{[K][K']}$$

$$\times \{\langle J_f\|F_K^{(s)}\|J_i\rangle\langle J_f\|F_{K'}^{(p)}\|J_i\rangle - \langle J_f\|F_K^{(p)}\|J_i\rangle\langle J_f\|F_{K'}^{(s)}\|J_i\rangle\}\mathscr{P}(K, K'; \hat{\boldsymbol{q}})\Bigg] , \tag{5·21}$$

where

$$\mathscr{P}(K, K'; \hat{\boldsymbol{q}}) = \sum_Q [Q](K'0K0|Q0) W(J_i K' J_i K; J_f Q)(J_i M_i Q0|J_i M_i) P_Q(\hat{\boldsymbol{q}}) . \tag{5·22}$$

By definition the following relation holds:

$$\frac{1}{[J_i]}\sum_{M_i} T_\pi(J_i M_i, J_f; \boldsymbol{q}) = \frac{1}{4\pi}\int T_\pi(J_i M_i, J_f; \boldsymbol{q}) d\Omega_q$$

$$= T(J_i, J_f; q) \text{ of Eq. (5·8)} . \tag{5·23}$$

Finally we can rewrite the above expression, Eqs. (5·22) ~ (5·23), in the form of the linear

Table XVI. The estimates of the hypernuclear π-mesic decay rate R_π in units of the free one R_Λ^{free}. See Eq. (5·13) for the S's and Eq. (5·14) for R_π. The q denotes the pion momentum in MeV/c.

| $^A_\Lambda Z(J_i) \to {}^A Z'$	(J_f)	q	$S(s)$	$S(p)$	R_π/R_Λ^{free}
$^6_\Lambda \mathrm{Li}(1^-_{g.s.}) \to {}^6\mathrm{Li}$	1^+	108.6	0.0086	0.029	0.0045
	3^+	105.2	0.000005	0.10	0.0044
	$0^+_{T=1}$	103.2	0.019	0.0	0.0064
	2^+	101.9	0.021	0.00007	0.0071
	$2^+_{T=1}$	100.2	0.049	0.0067	0.016
	1_2^+	99.6	0.0052	0.0049	0.0019
$^7_\Lambda \mathrm{Li}(1/2^+_{g.s.}) \to {}^7\mathrm{Li}$	$3/2^-$	110.0	0.15	0.016	0.055
	$1/2^-$	108.9	0.071	0.0079	0.026
	$7/2^-$	101.4	0.00006	0.000006	0.00002
	$5/2^-$	99.0	0.00004	0.000005	0.00002
$^8_\Lambda \mathrm{Li}(1^-_{g.s.}) \to {}^8\mathrm{Be}$	0^+	123.5	0.15	0.0	0.13
	2^+	118.7	0.39	0.011	0.31
	4^+	107.7	0.0003	0.000008	0.00022
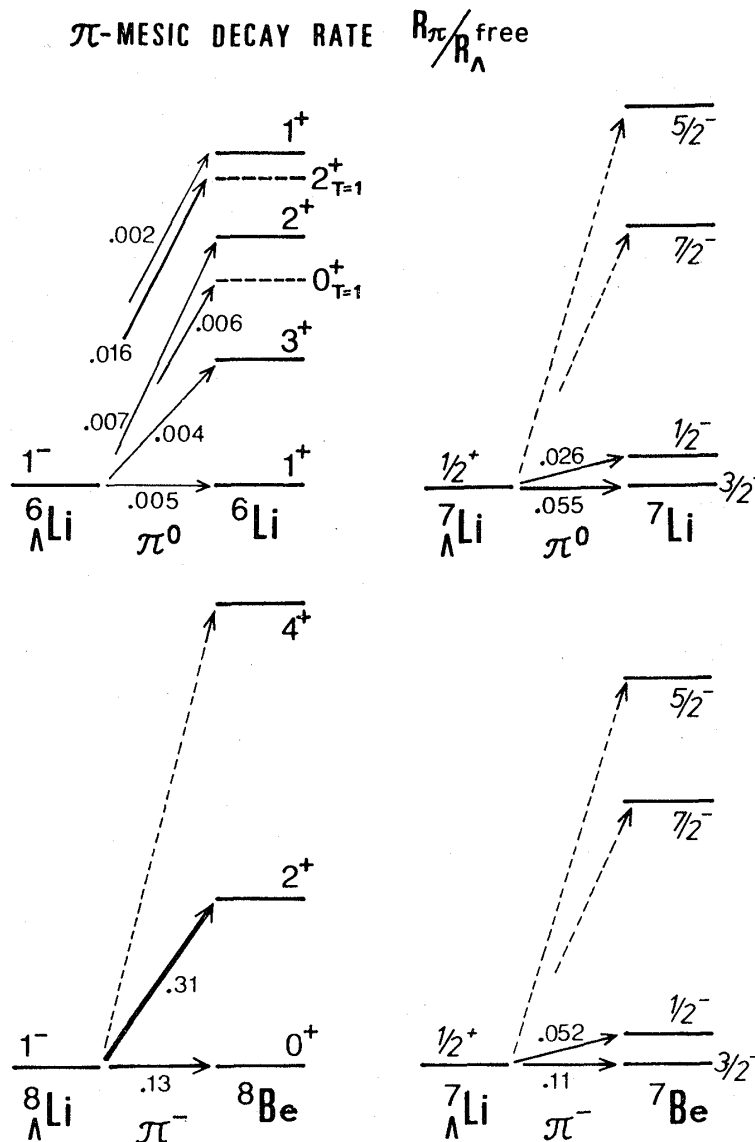
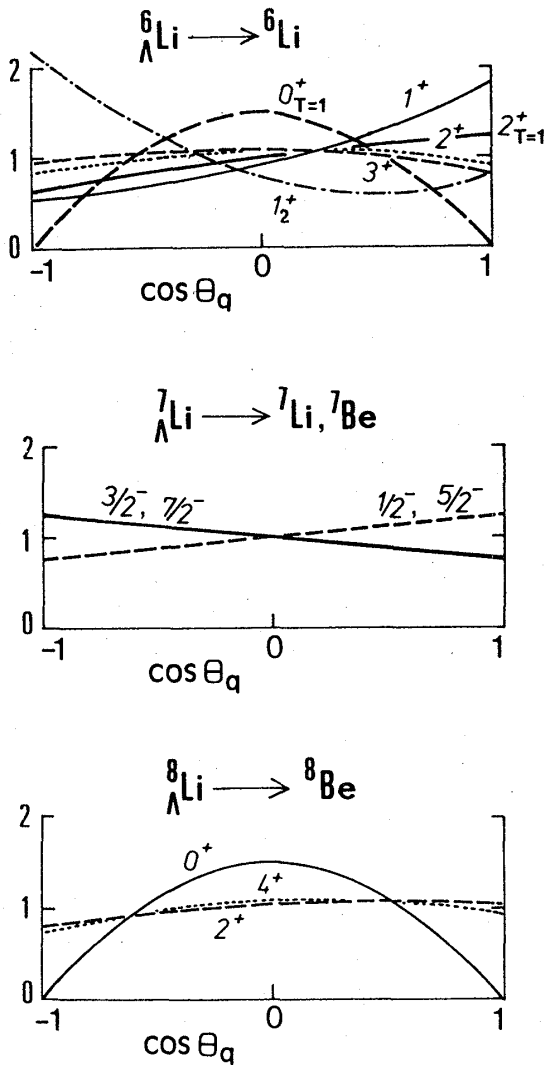Fig. 30. Calculated π-mesic decay rates in units of the free R_Λ^{free} of Eq. (5·20).

Fig. 31. Predictions of the pion angular distributions of the π-mesic decays from the polarized hyper-nuclear ground state.

combination of Legendre polynomials:

$$T_\pi(J_iM_i, J_f; \boldsymbol{q}) = \sum_Q T_\pi^Q(J_iM_i, J_f; q)P_Q(\hat{q}) .$$

$$(5 \cdot 24)$$

The identity $T_\pi^{Q=0}(J_iM_i, J_f; q) = T_\pi(J_i, J_f; q)$ is evident from Eq. (5·23).

5.2. Numerical results and discussion

In Fig. 30 are displayed the estimated decay rates for $^{6,7,8}_\Lambda$Li relative to the free Λ decay rate R_Λ^{free}, and in Table XVI the s-wave and p-wave contributions defined by Eq. (5·13) are separately listed with the involved pion momentum. In the π^0 decay of $^6_\Lambda$Li, the $2^+_{T=1}$ state is predicted to be most easily populated via the s-wave transition. Table XVI shows that the p-wave component with spin-flip mainly contributes to the decay $^6_\Lambda$Li($1^-_{\text{g.s.}}$) $\to$ ^{6}Li(1^+, 3^+). Note that the 1^+ and 3^+ daughter states have the $S=1$ wf's, while in the parent state the $S=0$ component dominates over the $S=1$ one:

$$|^6_\Lambda\text{Li}; 1^-\rangle = 68\%\,(l=1, \lambda=0)^{S=0}_{L=1}$$

$$+30.9\%\,(l=1, \lambda=0)^{S=1}_{L=1}+\cdots .$$

$$(5 \cdot 25)$$

The calculated results suggest that the lowest four states of ^{6}Li are nearly equally populated.

Table XVII. Relative contributions of Legendre polynomials, $T^Q/T^{Q=0}$, to the pion angular distributions. For definition see Eq. (5·24).

$^A_\Lambda Z(J_iM_i) \to {}^A Z'(J_f)$	J_f	$Q=0$	$Q=1$	$Q=2$
	1^+	1.	0.622	0.170
$^6_\Lambda$Li(1^-1) $\to$ ^{6}Li	3^+	1.	-0.038	-0.134
	$0^+_{T=1}$	1.	0.0	-1.0
	2^+	1.	0.038	-0.120
	$2^+_{T=1}$	1.	0.241	-0.052
	$1_2{}^+$	1.	-0.689	0.486
	$3/2^-$	1.	-0.245	—
$^7_\Lambda$Li($1/2^+1/2$) $\to$ ^{7}Li	$1/2^-$	1.	0.244	—
	$7/2^-$	1.	-0.225	—
	$5/2^-$	1.	0.228	—
	0^+	1.	0.0	-1.0
$^8_\Lambda$Li(1^-1) $\to$ ^{8}Be	2^+	1.	0.133	-0.060
	4^+	1.	0.107	-0.149

It is notable that the momentum of the emitted pion is higher than the free Λ decay case ($q_0 \cong 100$ MeV/c), because in most cases under consideration the Λ binding energy in a hypernuclear ground state is comparable to or less than that of the converted nucleon.

The $\pi^0(\pi^-)$ decay of $^7_\Lambda$Li is predicted to feed the lowest two states of ^{7}Li (^{7}Be), where the s-wave transition without spin-flip is dominant. See Fig. 30 and Table XVI. The $5/2^-$ and $7/2^-$ states can hardly be populated, because of high angular momentum transfer. The π^- decay rates leading to ^{7}Be is twice as large as the π^0 decay to ^{7}Li, which is just a consequence of the $\Delta I = 1/2$ rule Eq. (5·7).

The π^- decay of $^8_\Lambda$Li ($1^-_{\text{g.s.}}$) populates the lowest two states (0^+ and 2^+) of ^{8}Be with much greater rate than the other cases mentioned above. It is interesting to note that the 2^+ state is excited 2.5 times as strongly as the 0^+ state. This prediction may be tested by measuring the correlation with the subsequent α-decay of ^{8}Be (0^+, 2^+).

The pion angular distributions $T_\pi(J_iM_i, J_f; \boldsymbol{q})$ of Eq. (5·22) are evaluated for the case of the polarized hypernuclear state $|J_iM_i = J_i\rangle$. Table XVII shows the relative contributions of the Q-th Legendre, $T^Q/T^{Q=0}$, which is defined with Eq. (5·24). The results $R_\pi(\theta_q)$ are displayed in Fig. 31. It is interesting to note that strong angular dependences are predicted for the decays $^6_\Lambda$Li$\rightarrow ^6$Li($1^+_{1,2}$, $0^+_{T=1}$) and $^8_\Lambda$Li$\rightarrow ^8$Be(0^+). In the decays $^7_\Lambda$Li$\rightarrow ^7$Li & ^{7}Be(J_f) where the $P_{Q=1}$ contribution is essential, the sizable asymmetry is also expected (cf. Fig. 31). These observables will serve as a spectroscopic tool to study the hypernuclear structures.

§ 6. Particle-decay widths of $^9_\Lambda$Be by an advanced treatment

In §§ 3 and 4, we evaluated the widths of the typical resonance states in $^9_\Lambda$Be and $^{6,7}_\Lambda$Li on the basis of the reduced-width amplitudes which are deduced from the wf's obtained within the bound state approximation (BSA).[21),23),55)] In this section, by solving the channel-coupled scattering equation, we present the results of an advanced treatment for the $^9_\Lambda$Be system.

Here we are interested in the big peak observed in the forward ^{9}Be(K$^-$,π^-)$^9_\Lambda$Be reaction[1)~5)] at

$$E_\Lambda^{\text{exp}} = -B_\Lambda^{\text{exp}} = 6.3 \text{ MeV} \quad \text{with} \quad \Gamma^{\text{exp}} \cong 7 \text{ MeV.}^{3),4)} \qquad (6\cdot1)$$

According to the $\alpha + \alpha + \Lambda$ cluster model (cf. § 3), this peak corresponds to the $J^\pi = 3/2_2^-(L = 1_2^-)$ substitutional state obtained at $B_\Lambda^{\text{cal}} = -5.31$ MeV. The height of centrifugal barrier for the Λ particle in $L^\pi = 1^-$ state is only about 3 MeV. Thus, there arises a question why such a resonance, although broad, can exist at as high as $E_\Lambda = 6.3$ MeV. A key to solve this question is expected to exist in the fact that, in this energy region, three channels, $^5_\Lambda$He$+\alpha$, ^{8}Be(0^+)$+\Lambda$ and ^{8}Be(2^+)$+\Lambda$, are open and $E_\Lambda = 6.3$ MeV is not very high from the ^{8}Be(2^+)$+\Lambda$ threshold. With this in mind we investigate the energies and widths of the $L^\pi = 1^-$ states by solving a channel-coupled scattering problem, in which the above three channels are taken into account. The mechanism underlying the obtained resonances is discussed.

6.1. Formulation of the channel-coupled scattering equation

Throughout this section, the Λ particle is treated as if it were spinless for the same reason as in § 3. The trial wf with the orbital angular momentum L and its projection M

is defined using the numberred three channel wf's:

$$\Psi_{LM}(^9_\Lambda\text{Be}) = \Psi^{(1)}_{LM} + \Psi^{(2)}_{LM} + \Psi^{(3)}_{LM} , \tag{6·2}$$

$$^5_\Lambda\text{He}+\alpha: \qquad \Psi^{(1)}_{LM} = \sqrt{\frac{4!4!}{8!}}\mathcal{A}'\{\phi_{^5_\Lambda\text{He}}\phi_\alpha\chi^{(1)}_L(R_1)\,Y_L(\hat{\boldsymbol{R}}_1)\}_{LM} , \tag{6·3}$$

$$^8\text{Be}(0^+)+\Lambda: \qquad \Psi^{(2)}_{LM} = [\Phi(^8\text{Be};l=0)\times\chi^{(2)}_L(R_2)\,Y_L(\hat{\boldsymbol{R}}_2)]_{LM} , \tag{6·4}$$

$$^8\text{Be}(2^+)+\Lambda: \qquad \Psi^{(3)}_{LM} = \sum_\lambda[\Phi(^8\text{Be};l=2)\times\chi^{(3)}_\lambda(R_3)\,Y_\lambda(\hat{\boldsymbol{R}}_3)]_{LM} , \tag{6·5}$$

where $\chi^{(i)}(R)(i=1,2,3)$ denotes the relative wf between the relevant clusters. The ϕ_α represents the intrinsic wf of the α cluster with $(0s)^4$ h.o. configuration and the operator $\mathcal{A}'$ antisymmetrizes the nucleons belonging to the different clusters. The internal wf's, $\phi_{^5_\Lambda\text{He}}$ and $\Phi(^8\text{Be};l)$ are expressed by Eqs. (2·52) and (2·1)~(2·4), respectively. Their relative wf's are given by solving the $\alpha+\Lambda$ problem with the folding model and the microscopic $\alpha+\alpha$ problem, respectively, on the expansion basis of the locally peaked Gaussian function of the same type as Eq. (2·3).

Each relative wf $\chi^{(i)}(R)$ is similarly expanded in terms of the Gaussian wave packet $\{\varphi_L(R;D)\}$ with the appropriate size parameter:

$$\chi^{(i)}_L(R) = \sum_D f^{(i)}_L(D)\varphi_L(R;D) , \qquad R < R_i{}^c , \tag{6·6a}$$

$$= \delta_{ij}\chi^{(-)}_L(k_i;R) - S_{ji}\chi^{(+)}_L(k_i;R) , \qquad R > R_i{}^c , \tag{6·6b}$$

where the generator coordinate D specifies the inter-cluster distance. The $\chi^{(\pm)}_L(k_i;R)$ represent the incoming $(-)$/outgoing$(+)$ wf with the channel wave number k_i and S_{ji} the S-matrix element for the $i \to j$ transition. The wf $\chi^{(i)}_L$ is smoothly connected at the channel radius $R_i{}^c$.

The total Hamiltonian H is given by the kinetic energy T and the two-body NN and ΛN interactions,

$$H = T + V_{NN} + V_{\Lambda N} , \tag{6·7}$$

$$T = \sum_{k=1}^8 t_k{}^N + t^\Lambda - T_{CM} , \tag{6·8}$$

$$V_{NN} = \sum_{k>l=1}^8 v_{NN}(k,l), \qquad V_{\Lambda N} = \sum_{k=1}^8 v_{\Lambda N}(\Lambda,k) , \tag{6·9}$$

where the center-of-mass kinetic energy T_{CM} is subtracted. From the variational principle

$$\langle\delta\Psi^{(i)}|H-E|\Psi\rangle = 0 , \tag{6·10}$$

we get a set of coupled integro-differential equations to determine $f^{(i)}_L(D)$ and S_{ji} of the relative wf $\chi^{(i)}(R_i)$ $(i=1,2,3)$. Here we follow the variational method developed by Kamimura et al.[56] For the expressions of the GCM overlap and Hamiltonian kernels one can refer to the Appendix of Ref. 57).

From the S-matrix the cross section is given by

$$\sigma_L(i \to j) = \frac{3}{k_i{}^2}|\delta_{ji} - S_{ji}| . \tag{6·11}$$

6.2. Interactions and the model space

As the two-body NN interaction we employ the Volkov No. $2^{58)}$ with the Majorana parameter $M_{NN}=0.56$. The Coulomb interaction is also taken into account. This choice of parameters along with the size $b_N=1.358$ fm leads to a successful reproduction of the α-α scattering data for the ^{8}Be ground band ($l=0^+$, 2^+, 4^+).$^{59)}$ For the ΛN part we use the ORG interaction of Eq. (2·29) which reproduces $B_\Lambda^{\mathrm{exp}}(^5_\Lambda \mathrm{He})=3.12$ MeV.

The calculations are carried out within the following model space:

(I)   the three channel states for the $L=1$ scattering:

channel-1: $^5_\Lambda \mathrm{He}+\alpha$,
channel-2: $^8\mathrm{Be}(0^+)+\Lambda(\lambda=1)$,
channel-3: $^8\mathrm{Be}(2^+)+\Lambda(\lambda=1)$.

(II)   the generator coordinate mesh points:

$D_1=2.5$, 3.0, $\cdots$, 6.5, 7.0 fm   (10 points) ,
$D_2(D_3)=0.5$, 1.5, $\cdots$, 5.5, 6.5 fm   (7 points) .

(III)   the channel radii:

$R_1=7.5$ fm , $R_2(R_3)=7.0$ fm .

As for the angular momentum, the $\lambda=3$ component was found to be negligible. It should be noted that essentially important is the reproduction of the experimental threshold energies involved in the coupled channel scattering problem. The adopted parameters and internal wf's are quite satisfactory in this respect.

6.3. The BSA results of the $L^\pi=1^-$ structure characteristics

In order to facilitate understanding of the meaning of scattering solutions, first we solve the channel-coupled equation under the BSA and see the structure characteristics of the obtained eigenstates with $L^\pi=1^-$. We define the channel probability which is the squared overlap between the total wf, Eq. (6·2), and each single-channel wf:

$$P_N^{(i)}(L_n) = \langle \Psi_{\mathrm{BSA}}^{\mathrm{total}}(L_N) | \Psi_{\mathrm{BSA}}^{(i)}(L_n)\rangle^2 , \quad i=1, 2, 3. \qquad (6·12)$$

Table XVIII. Squared overlaps $P_N^{(i)}(L_n)$ between the channel-coupled total wave function and the channel wf solved within the indicated channel (s), respectively. The definition is given by Eq. (6·12)

Channel wf $\Psi_{\mathrm{BSA}}^{(i)}(L_n)$	$(E_\Lambda=-B_\Lambda)$ MeV	Channel-coupled wf $\Psi_{\mathrm{BSA}}^{\mathrm{total}}(L_N)$		
		$L_N=1_{\overline{\mathrm{I}}}$ (-0.5 MeV)	$L_N=1_{\overline{\mathrm{II}}}$ (3.7 MeV)	$L_N=1_{\overline{\mathrm{III}}}$ (5.0 MeV)
$\Psi_{\mathrm{BSA}}^{(1)}:[^5_\Lambda \mathrm{He}+\alpha]$	$L_n=1_1{}^-(-0.3)$	0.980	0.003	0.004
	$1_2{}^-(\ \ 3.9)$	0.001	0.941	0.053
$\Psi_{\mathrm{BSA}}^{(2)}:[^8\mathrm{Be}(0^+)+\Lambda]$	$1_1{}^-(\ \ 3.1)$	0.387	0.119	0.447
	$1_2{}^-(\ \ 9.2)$	0.053	0.008	0.145
$\Psi_{\mathrm{BSA}}^{(3)}:[^8\mathrm{Be}(2^+)+\Lambda]$	$1_1{}^-(\ \ 4.8)$	0.338	0.000	0.341
	$1_2{}^-(\ 10.9)$	0.029	0.018	0.000
$\Psi_{\mathrm{BSA}}^{(2+3)}:[^8\mathrm{Be}(0^+, 2^+)+\Lambda]$	$1_1{}^-(\ \ 1.5)$	0.795	0.093	0.012
	$1_2{}^-(\ \ 5.2)$	0.014	0.035	0.920

The values are summarized in Table XVIII where the overlaps with the two-channel solution $\Psi^{(2+3)}$ are also listed.
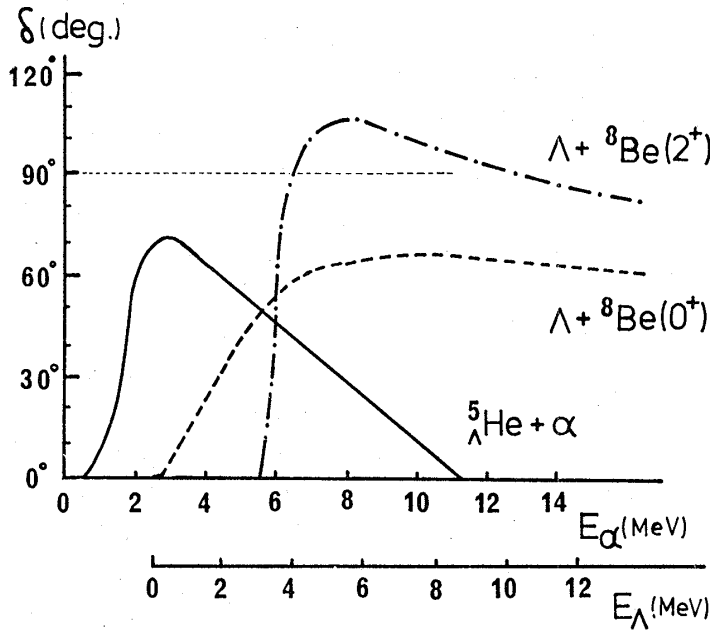
Fig. 32. Phase shifts for the $L^\pi = 1^-$ partial waves calculated independently in the $^5_\Lambda$He$+\alpha$, ^{8}Be(0^+) $+\Lambda$ and ^{8}Be$(2^+)+\Lambda$ channels respectively.

Table XVIII shows that the $L_N = 1_{\mathrm{I}}^-$ solution obtained at $E_\Lambda^{\mathrm{cal}} = -0.5$ MeV has a very nice two-cluster ($^5_\Lambda$He $+\alpha$) structure as $P_1^{(1)}(1_1^-) = 0.980$. At the same time, however, it has a large overlap with $\Psi^{(2+3)}(1_1^-)$. This fact indicates that the three channels are not fully independent. This state 1_{I}^- is expected to have a sizable α-decay width, since it appears at 2.3 MeV above the $^5_\Lambda$He$+\alpha$ threshold, which is just at the top of the Coulomb plus centrifugal barrier.

The second solution $L_N = 1_{\mathrm{II}}$ at $E_\Lambda^{\mathrm{cal}} = 3.7$ MeV has a large overlap with the higher nodal wf $\Psi^{(1)}(1_2^-)$ of the $^5_\Lambda$He$+\alpha$ single channel. However, because the energy of the higher nodal
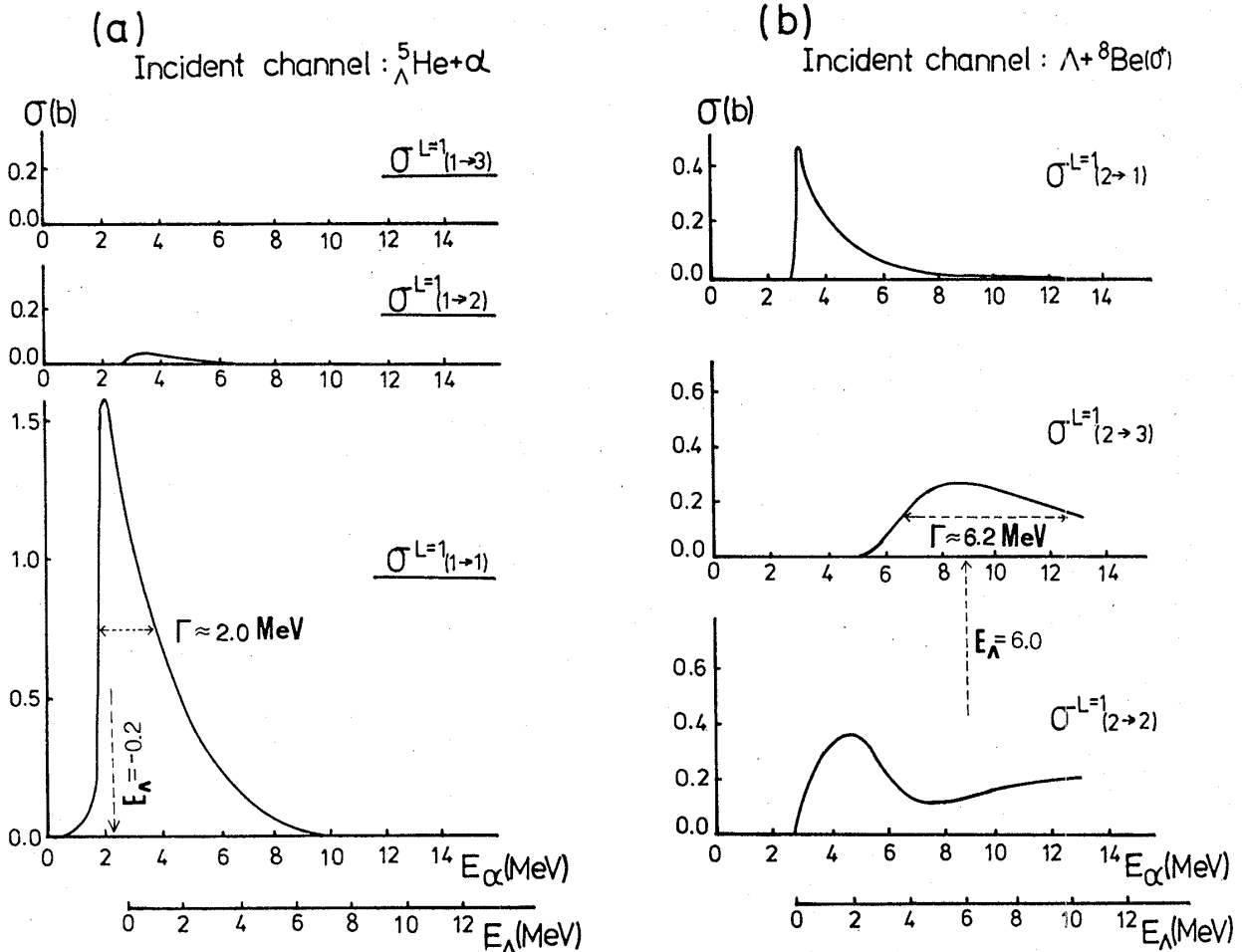
(a)

Incident channel : $^5_\Lambda$He$+\alpha$

(b)

Incident channel : $\Lambda + {}^8$Be(0^+)

Fig. 33. Calculated cross sections as a function of the $\Lambda(\alpha)$ incident energy in the CM frame.

state is too high above the $^5_\Lambda$He $+\alpha$ threshold, this BSA $1_{\overline{\mathrm{II}}}$ solution does not seem to remain as a resonance when the problem is treated under the correct scattering boundary condition.

The BSA third solution $L_N = 1_{\overline{\mathrm{III}}}$ obtained at $E_\Lambda^{\mathrm{cal}} = 5.0$ MeV has a structure very similar to the $\Psi^{(2+3)}(1_2{}^-)$ of the two-channel calculation. It is notable, as already discussed in § 3, that this $1_{\overline{\mathrm{III}}}$ wf shares a considerable amount of the ^{8}Be $(2^+) + \Lambda$ component and moreover that the energy is not very high from the corresponding threshold. From these facts this state is expected to show a resonance-like structure. Thus we learn here that there can be two 1^- states ($1_{\overline{\mathrm{I}}}$ and $1_{\overline{\mathrm{III}}}$) which will persist in the scattering treatment.

6.4. Results and discussion on the $L^\pi = 1^-$ resonance states

First we calculate the phase shift of the $L^\pi = 1^-$ partial wave by solving independently the scattering equation for each channel. Figure 32 shows that the channel-1 ($^5_\Lambda$He $+\alpha$) phase shift does not reach $90°$, although we find a broad resonance in the cross section at $E_\Lambda = 3.0$ MeV, since it is located around the top of the Coulomb plus centrifugal barrier. Only the channel-3 phase shift goes over $90°$ to show a clear resonance. The reason is bacause the ^{8}Be$(2^+) + \Lambda$ folding potential is strong enough to make a quasi-bound state, while the ^{8}Be$(0^+) + \Lambda$ potential (channel-2) is weaker. (See Fig. 6.) Note that the difference between their potential depths makes the two channels close in energy.

Let us switch on the couplings among the three channels. The calculated results of the cross sections $\sigma(i \to j)$ are displayed in Fig. 33 and the S-matrix elements $|S_{ji}|$ in Fig. 34 as a function of the $\alpha(\Lambda)$ incident energy $E_\alpha(E_\Lambda)$ in the center-of-mass frame (E_α^{cal}
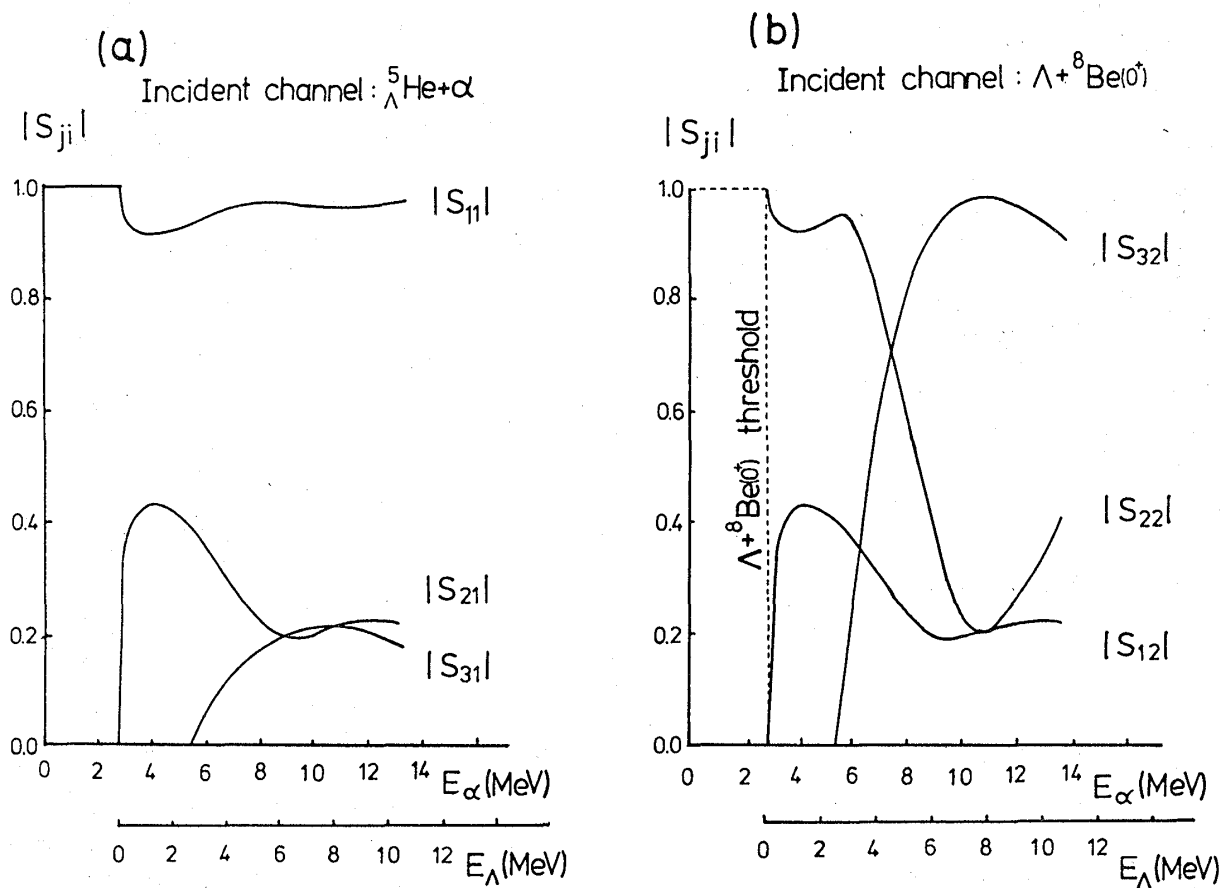

Fig. 34. Behaviors of the S-matrix elements as a function of the $\Lambda(\alpha)$ incident energy in the CM frame.

$=E_\Lambda^{cal}+2.5\,\mathrm{MeV}$). In the $^5_\Lambda\mathrm{He}+\alpha$ elastic cross section, as seen in Fig. 33(a), we find a rather broad resonance state at

$$^9_\Lambda\mathrm{Be}(L=1_1^-): \qquad E_\Lambda^{cal}=-B_\Lambda=-0.2 \quad (E_\alpha=2.3)\,\mathrm{MeV} \quad \text{with} \quad \Gamma\cong2.0\,\mathrm{MeV}.$$

In view of the preceding consideration, this resonance state corresponds to the $K^\pi=0^-$ band head: $L=1_1^-$ in Fig. 5 or $L_N=1_I^-$ in Table XVIII. We also see some structures in both $\sigma(1\to2)$ and $|S_{21}|$ when the channel-2 is open at $E_\Lambda\geqq0\,\mathrm{MeV}$. These behaviors are due to the effect of the channel couplings. In the $^9\mathrm{Be}(K^-,\pi^-)^9_\Lambda\mathrm{Be}$ experiment,[3],[4] the corresponding peak has not yet been observed, because the state is not easily excited from the $^9\mathrm{Be}$ target as already discussed in § 3. It is expected to be observed, however, if the coincidence experiments such as $^9\mathrm{Be}(K^-,\pi^-a)^5_\Lambda\mathrm{He}$ reaction are carried out in future.

In the inelastic cross section $\sigma(2\to3)$ for the $^8\mathrm{Be}(0^+)+\Lambda$ to $^8\mathrm{Be}(2^+)+\Lambda$ transition, there appears a broad resonance at

$$^9_\Lambda\mathrm{Be}(L=1_2^-): \qquad E_\Lambda^{cal}=-B_\Lambda=6.0\,\mathrm{MeV} \quad \text{with} \quad \Gamma\cong6.2\,\mathrm{MeV}.$$

The strong channel coupling between the two are also recognized from the interferent behaviors of the $|S_{22}|$ and $|S_{32}|$ in the resonance region (Fig. 34(b)). This resonance state corresponds to the $K^\pi=1^-$ band head: $L=1_2^-$ in Fig. 5 or $L_N=1_{III}^-$ in Table XVIII. Thus the characteristics predicted in the BSA treatment are confirmed. The effect of this resonance is also seen in Figs. 33(a) and 34(a). It is remarkable that the observed big
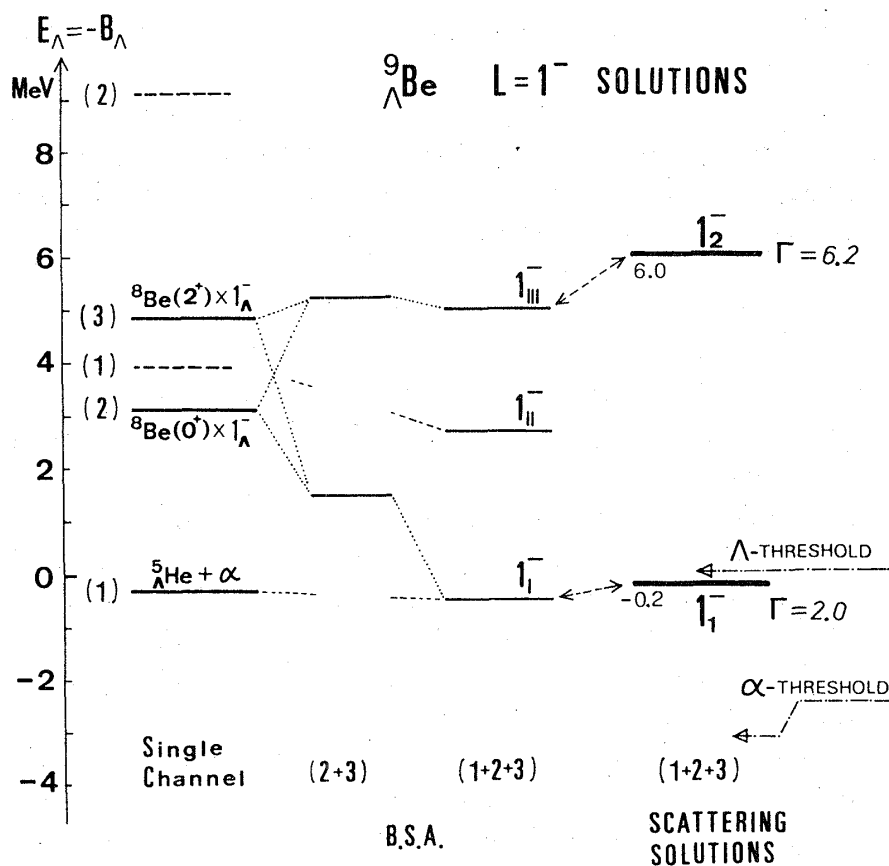

Fig. 35. The solutions of the $L^\pi=1$ states of $^9_\Lambda\mathrm{Be}(J=L\pm1/2)$ obtained by introducing the channel coupling. The BSA denotes the treatment within the framework of the bound state approximation.

·peak[3),4)] under consideration, Eq.(6·1), can be nicely explained by the present resonance solution.

An important point is the fact that there can be a resonance state at such an energy region as much higher than the Coulomb plus centrifugal barrier, although the width itself is 'broad'. The mechanism can be summarized as follows:

(i)   For the $L=1^-$ states the two channels, $(l,\lambda)_L = (0,1)_{1^-}$ and $(2,1)_{1^-}$, are almost degenerate in energy as shown by the microscopic $\alpha + \alpha + \Lambda$ cluster model with the BSA treatment.

(ii)   The strong channel coupling pushes down the 1_1^- state just below the top of the $_{\Lambda}^5$He$+\alpha$ barrier (near the ^{8}Be$(0^+)+\Lambda$ threshold) and correspondingly pushes the other 1_2^- state up to such a 'high' energy.

(iii) As the result the 1_2^- state carries a sizable amount of the $(l,\lambda) = (2,1)$ component in which there exists a sharp resonance. It is this component that contributes to forming the obtained 'broad' resonance.

(iv)   The lower 1_1^- state is predicted to be just near the Λ-threshold (bound or quasi-bound, considering possible uncertainties in the calculation). It is notable, however, that this "genuinely hypernuclear" state should be observed in the coincidence experiment in the α-decay channel, ^{9}Be$(K^-,\pi^-\alpha)_{\Lambda}^5$He, as it is to show a resonance-like structure with $\Gamma_\alpha \cong 2$ MeV.

The situation is depicted in Fig. 35.

A few words may be necessary here because, strictly speaking, the present evaluation of the width does not directly correspond to the actual width in the (K^-,π^-) reaction. It can be expected, however, that the calculated width is quite similar to that of the (K^-,π^-) experiment due to the following reason: The wf of the outgoing pion is not largely distorted, as its energy is high ($p_\pi \approx 600$ MeV$/c$, $T_\pi \approx 480$ MeV). Therefore the observed pions have rather honest information of the $_{\Lambda}^9$Be hypernuclear structure which is just generated by the recoilless conversion of a neutron to Λ. A more realistic evaluation of the ^{9}Be$(K^-, \pi^-)_{\Lambda}^9$Be reaction excitation function is in progress.[60)]

§7. Summary

We have systematically studied the production, structure and decay of the light p-shell Λ-hypernuclei, $_{\Lambda}^5$He, $_{\Lambda}^6$Li, $_{\Lambda}^7$Li, $_{\Lambda}^8$Li, $_{\Lambda}^8$Be and $_{\Lambda}^9$Be, standing on the cluster-model point of view. In order to incorporate both the shell-model and cluster-model aspects, these hypernuclei have been described as the microscopic $\alpha + x + \Lambda$ three cluster system ($x = n$, $p,d,t,^3$He or α). The model space covers a variety of high-lying as well as important low-lying shell-model bases for the Λ particle and/ or the core nucleus. We have explained the existing data quite successfully and also given an extensive prediction of various physical observables, which exhibit rich aspects of the hypernuclear dynamics. Main results of this chapter are summarized as follows.

(a)   The positive and negative parity states up to about 20 MeV excitation are presented for each of these hypernuclei and found to be in good agreement with all the existing experimental data. It is noteworthy that our wave functions can reproduce not only the energy positions but also the relative production rates for the ground-state small peak and the substitutional two big peaks observed in the forward (K^-,π^-) reactions leading to $_{\Lambda}^6$Li, $_{\Lambda}^7$Li and $_{\Lambda}^9$Be. Some other excited states are predicted to come into

observation under the appropriate conditions such as the measurement of pion angular distributions, stopped-K^- absorptions and various coincidence experiments.

(b) The energy levels are classified into several characteristic bands (or groups) according to the underlying intrinsic structures. The addition of the $s_{1/2}$-state Λ particle to a core nucleus ($l + S_x = j_x$) generates the corresponding doublet which can be well described with a single weak-coupling configuration $[(j_x) \times s_{1/2}^A]$. The member carrying a larger $S_< = |S_x - 1/2|$ component appears lower in energy than the other of the doublet because of the adopted positive ΛN spin-spin interaction. The different parity excited states with the Λ particle being dominantly in the p-state can be divided into four (two for ${}^9_\Lambda$Be) groups in good approximation, since, in addition to the spin $S_<$ or $S_>$, the Λ particle can move parallel (orbital $K = 0$; $p_{//}$) or perpendicular ($K = 1$; $p_\perp$) to the α-x deformation axis. Thus, in the L-S coupling picture, they may be called as $S_<$(or $S_>$)-analogs of the corresponding ordinary nuclear levels. Among others, "genuinely hypernuclear" groups are realized by virtue of the inaction of the Pauli exclusion principle on Λ and are particularly intriguing because of the new symmetries they carry.

(c) In the ${}^5_\Lambda$He and ${}^9_\Lambda$Be cases, we have used the realistic YNG(ΛN) interaction to examine the effects in the structure calculations. The repulsive soft core and the exchange component existing in the YNG interaction give rise to some significant features in the hypernuclear cluster problem. We have found, however, that the net effect of the use of this interaction does not change the principal aspect obtained by using the simple one-range Gaussian force employed throughout this chapter.

(d) The hypernuclear γ-transition probabilities and magnetic dipole moments have been theoretically estimated. The existing data of the γ transition energies in ${}^7_\Lambda$Li, ${}^8_\Lambda$Li and ${}^9_\Lambda$Be are in good correspondence to our predictions of E2($5/2^+ \to 1/2^+$) and M1($1_2^- \to 1_1^-$) and E2($3/2^+, 5/2^+ \to 1/2^+$), respectively. The most interesting feature regarding the γ-transitions is the drastic reduction of the intra-band B(E2) values, which can be nearly half the corresponding ones of the core nucleus. This effect is a manifestation of the stabilization and contraction of hypernuclear system due to the glue-like role of the Λ particle. In spite of this fact, the B(E2) values remain several times enhanced in comparison with the shell-model limit values, indicating the importance of properly taking into account the clustering aspect in light hypernuclei.

(e) The particle decay widths of the resonance peaks are evaluated by the separation energy method and, in addition, for ${}^9_\Lambda$Be by solving the channel-coupled scattering equation. The latter treatment clarifies the mechanism of the existence of the high-lying resonance and nicely explains the observed peak width.

The relative π-mesic decay rates of these hypernuclei are also predicted including the pion angular distributions, which will serve as a spectroscopic tool to study the structures.

(f) The hypernuclear spectroscopy, which has just started with the development of (K^-, π) type reaction experiments, is already disclosing new and interesting aspects of the hypernuclear system. Different types of reactions such as (π, K^+), (K^-, K^+), $(e, e'K^+)$, (p, K^+) and/or various coincidence experiments could be fully exploited in future and respectively shed light on the characteristic feature of hypernuclei. Such multi-sided approach will add up to the construction of the unified picture of hypernuclei. Through the present work, we have tried to have qualitative physical pictures of the hypernuclear dynamics as well as quantitative explanations and predictions of data. We have paid attention to the question of what really new in hypernuclear system, that is, what is

"genuinely hypernuclear". The present investigation will be hopefully useful to understand and stimulate the existing and coming experimental information on hypernuclear physics.

Acknowledgements

Appendix A

—— The $\alpha + \Lambda$ GCM Kernels for the Direct/Exchange ΛN Interaction ——

The realistic ΛN interaction of Eq. (2·30) employed in § 3.5 consists of the direct and exchange parts: $v_{\Lambda N}(x) = V_D(x) + V_{ex}(x)\hat{P}_x$. Here the matrix elements are given for the Gaussian ΛN interaction (range $\beta = \beta_1$, β_2, or β_3),

$$V_{\Lambda N} = \sum_{i_N} v_{\Lambda N}(x) \left\{ \begin{matrix} 1 \\ \hat{P}_x \end{matrix} \right\} = \sum_{i_N} v_{\Lambda N}^0 e^{-x^2/\beta^2} \left\{ \begin{matrix} 1 \\ \hat{P}_x \end{matrix} \right\} , \tag{A·1}$$

where $x = r_\Lambda - r_N$ and the exchange operator $\hat{P}_x$ transforms x to $-x$ with the ΛN center-of-mass rest.

The intrinsic wave function (wf) of ${}_\Lambda^5\text{He} = \alpha + \Lambda$ is given by

$$\begin{aligned} \Phi^{\alpha\Lambda}(d) &= \phi_\alpha(\nu_4 d) \cdot \phi_\Lambda(-\nu_1 d) \\ &= \frac{1}{\sqrt{4!}} \mathcal{A}\{\phi_N(\nu_4 d)^4\} \cdot (\sqrt{\pi} b_\Lambda)^{-3/2} \exp[-(r_\Lambda + \nu_1 d)^2/2b_\Lambda^2] , \end{aligned} \tag{A·2}$$

$$\phi_N(\nu_4 d) = (\sqrt{\pi} b_N)^{-3/2} \exp[-(r_N - \nu_4 d)^2/2b_N^2] , \tag{A·3}$$

where the generator coordinate d specifies the $\alpha - \Lambda$ distance, and the parameters are defined as

$$\nu_4 = \frac{M_\Lambda}{4M_N + M_\Lambda} , \quad \nu_1 = \frac{4M_N}{4M_N + M_\Lambda} , \tag{A·4}$$

$$\mu_{\Lambda\alpha} b_{\Lambda\alpha}^2 \equiv \frac{4M_N M_\Lambda}{4M_N + M_\Lambda} b_{\Lambda\alpha}^2 = M_\Lambda b_\Lambda^2 = M_N b_N^2 = \hbar\Omega^{-1} . \tag{A·5}$$

Then the wf of Eq. (A·2) is expressed as

$$\Phi^{\alpha\Lambda}(d) = \phi_\alpha^{int} \cdot (\sqrt{\pi} b_{\Lambda\alpha})^{-3/2} \exp[-(r-d)^2/2b_{\Lambda\alpha}^2] \cdot \phi_G(R_G) , \tag{A·6}$$

from which the angular momentum projection leads to the GCM basis wf $\Phi_l(d)$ given by Eqs. (3·10) and (3·11). With this basis, the normalization, kinetic energy and ΛN interaction kernels of the $\alpha + \Lambda$ system are given as follows:

$$\langle \Phi_l(d_1) | \Phi_l(d_2) \rangle = 4\pi \exp[-(d_1^2 + d_2^2)/4b_{\Lambda\alpha}^2] \mathcal{I}_l(d_1 d_2/2b_{\Lambda\alpha}^2) , \tag{A·7}$$

$$\langle \Phi_l(d_1) | -\frac{\hbar^2}{2\mu_{\Lambda\alpha}} \nabla^2 | \Phi_l(d_2) \rangle = 4\pi \frac{\hbar^2}{\mu_{\Lambda\alpha} b_{\Lambda\alpha}^2} \exp[-(d_1^2 + d_2^2)/4b_{\Lambda\alpha}^2]$$

$$\times \left\{ \left(\frac{3}{4} - \frac{d_1{}^2 + d_2{}^2}{8 b_{Aa}^2} \right) \mathcal{G}_l(d_1 d_2 / 2 b_{Aa}^2) + \frac{d_1 d_2}{4 b_{Aa}^2} \mathcal{G}_l{}'(d_1 d_2 / 2 b_{Aa}^2) \right\} , \qquad (\text{A} \cdot 8)$$

$$\langle \Phi_l(d_1) | V_{AN} | \Phi_l(d_2) \rangle = 16 \pi v_{AN}^0 \left(\frac{\nu_{AN}}{\nu_{AN} + \mu} \right)^{3/2} \exp[-\Gamma(d_1{}^2 + d_2{}^2)] \mathcal{G}_l(\gamma_\pm d_1 d_2) . \quad (\text{A} \cdot 9)$$

Here the $\mathcal{G}_l(z)$ is the spherical Bessel function with an imaginary argument, and the relation holds,

$$\mathcal{G}_l{}'(z) = \frac{l}{z} \mathcal{G}_l(z) + \mathcal{G}_{l+1}(z) . \qquad (\text{A} \cdot 10)$$

The notations used above are defined as

$$\mu = \beta^{-2} , \quad \nu_N = b_N^{-2} , \quad \nu_A = b_A^{-2} , \qquad (\text{A} \cdot 11)$$

$$\nu_{AN} = \frac{\nu_N \nu_A}{\nu_N + \nu_A} , \quad \nu_{Aa} = \frac{4 \nu_N \nu_A}{4 \nu_N + \nu_A} = b_{Aa}^{-2} , \qquad (\text{A} \cdot 12)$$

$$\Gamma = \frac{1}{4} \left(\nu_{Aa} + \frac{\nu_{AN} \mu}{\nu_{AN} + \mu} \right) , \qquad (\text{A} \cdot 13)$$

$$\gamma_\pm = \frac{1}{2} \left\{ \nu_{Aa} - \frac{\nu_{AN} \mu + (1 \mp 1) \nu_{AN}^2}{\nu_{AN} + \mu} \right\} , \qquad (\text{A} \cdot 14)$$

where the upper/lower sign corresponds to the direct/exchange interaction case.

Appendix B

—— *The $\alpha + \alpha + \Lambda$ GCM Kernels for the Direct/Exchange ΛN Interaction* ——

The $_\Lambda^9\text{Be} = \alpha + \alpha + \Lambda$ wave function before angular momentum projection is given by

$$\Psi(\boldsymbol{d}, \boldsymbol{D}) = \psi_{\alpha\alpha}(\boldsymbol{d}, \boldsymbol{D}) \cdot \phi_A(-\chi_A \boldsymbol{D})$$

$$= \frac{1}{\sqrt{8!}} \mathcal{A}' \left\{ \phi_N \left(\chi_N \boldsymbol{D} + \frac{\boldsymbol{d}}{2} \right)^4 \phi_N \left(\chi_N \boldsymbol{D} - \frac{\boldsymbol{d}}{2} \right)^4 \right\} \cdot \phi_A(-\chi_A \boldsymbol{D}) , \qquad (\text{B} \cdot 1)$$

$$\chi_N = \frac{M_A}{8 M_N + M_A} , \quad \chi_A = \frac{8 M_N}{8 M_N + M_A} , \qquad (\text{B} \cdot 2)$$

where ϕ_i means the s-orbit wf with respect to the indicated center and is defined analogously by Eq. (A·3). The generator coordinates $\boldsymbol{d}$ and $\boldsymbol{D}$ specify the α-α and $(\alpha\alpha)$-Λ distances, respectively.

The matrix element of the direct/exchange ΛN interaction, Eq. (A·1) ($i_N = 1, 2, \cdots 8$), is calculated according to the Brink method[61] as

$$\langle \Psi(\boldsymbol{d}_1, \boldsymbol{D}_1) | V_{AN} | \Psi(\boldsymbol{d}_2, \boldsymbol{D}_2) \rangle$$

$$= \langle \psi_{\alpha\alpha}(\boldsymbol{d}_1, \boldsymbol{D}_1) | \psi_{\alpha\alpha}(\boldsymbol{d}_2, \boldsymbol{D}_2) \rangle \sum_{i,j=1}^{8} \langle \phi_{N,i} \phi_A | v_{AN}(x) \left\{ \begin{matrix} 1 \\ \hat{P}_x \end{matrix} \right\} | \phi_{N,j} \phi_A \rangle (B^{-1})_{ji} , \qquad (\text{B} \cdot 3)$$

$$= 4 v_{AN}^0 \left(1 + \frac{\mu}{\nu_{AN}} \right)^{-3/2} \exp[-\alpha_1(D_1{}^2 + D_2{}^2)] \cdot \exp[-\alpha_2(d_1{}^2 + d_2{}^2)] \cdot \exp[\alpha_3 \boldsymbol{D}_1 \boldsymbol{D}_2]$$

$$\times \sum_{m=0}^{3} \binom{3}{m}(-)^{m+1}\Big[\exp[\alpha_4(m)\,\boldsymbol{d}_1\boldsymbol{d}_2]\big\{\exp[\alpha_5(\boldsymbol{D}_1\boldsymbol{d}_1+\boldsymbol{D}_2\boldsymbol{d}_2)+\alpha_6(\boldsymbol{D}_1\boldsymbol{d}_2+\boldsymbol{D}_2\boldsymbol{d}_1)]$$

$$+\exp[-\alpha_5(\boldsymbol{D}_1\boldsymbol{d}_1+\boldsymbol{D}_2\boldsymbol{d}_2)-\alpha_6(\boldsymbol{D}_1\boldsymbol{d}_2+\boldsymbol{D}_2\boldsymbol{d}_1]\big\}$$

$$+\exp[-\alpha_4(m)\,\boldsymbol{d}_1\boldsymbol{d}_2]\big\{\exp[\alpha_5(\boldsymbol{D}_1\boldsymbol{d}_1-\boldsymbol{D}_2\boldsymbol{d}_2)-\alpha_6(\boldsymbol{D}_1\boldsymbol{d}_2-\boldsymbol{D}_2\boldsymbol{d}_1)]$$

$$+\exp[-\alpha_5(\boldsymbol{D}_1\boldsymbol{d}_1-\boldsymbol{D}_2\boldsymbol{d}_2)+\alpha_6(\boldsymbol{D}_1\boldsymbol{d}_2-\boldsymbol{D}_2\boldsymbol{d}_1)]\big\}\Big].$$

$$(B\cdot 4)$$

The notations used here are defined by

$$\alpha_1=\frac{1}{4}\Big(8\nu_N\chi_N{}^2+\nu_A\chi_A^2+\frac{\mu\nu_{AN}}{\mu+\nu_{AN}}\Big),\tag{B·5a}$$

$$\alpha_2=\frac{1}{16}\Big(8\nu_N+\frac{\mu\nu_{AN}}{\mu+\nu_{AN}}\Big),\tag{B·5b}$$

$$\alpha_3=\frac{1}{2}\Big\{8\nu_N\chi_N{}^2+\nu_A\chi_A^2-\nu_{AN}\pm\frac{\nu_{AN}^2}{\mu+\nu_{AN}}\Big\},\tag{B·5c}$$

$$\alpha_4(m)=\frac{2m-3}{4}\nu_N+\frac{1}{8}\Big\{2\nu_N-\nu_{AN}\pm\frac{\nu_{AN}^2}{\mu+\nu_{AN}}\Big\},\tag{B·5d}$$

$$\alpha_5=-\frac{1}{4}\frac{\mu\nu_{AN}}{\mu+\nu_{AN}},\tag{B·5e}$$

$$\alpha_6=\frac{1}{4}\Big\{-\nu_{AN}\pm\frac{\nu_{AN}^2}{\mu+\nu_{AN}}\Big\}.\tag{B·5f}$$

On the other hand, we divide the wf of Eq. (B·1) into the internal ($\alpha\alpha$) and relative parts,

$$\Psi(\boldsymbol{d},\boldsymbol{D})=\Phi_{\alpha\alpha}^{\mathrm{int}}(\boldsymbol{d})\cdot\varphi^A(\boldsymbol{R};\boldsymbol{D}),\tag{B·6}$$

$$\varphi^A(\boldsymbol{R};\boldsymbol{D})=(\sqrt{\pi}\,b_R)^{-3/2}\exp[-(\boldsymbol{R}-\boldsymbol{D})^2/2b_R{}^2],\tag{B·7}$$

which can be expressed in the angular momentum coupled form as

$$\Psi(\boldsymbol{d},\boldsymbol{D})=\sum_{l\lambda L}(-)^{l+\lambda}\sqrt{[L]}\Big[[\Phi^{\alpha\alpha}(l;d)\times\varphi_\lambda(R;D)\,Y_\lambda(\hat{\boldsymbol{R}})]_L[Y_l(\hat{\boldsymbol{d}})\times Y_\lambda(\hat{\boldsymbol{D}})]_L\Big]_0\tag{B·8}$$

with the $\Phi^{\alpha\alpha}(l;d)$ being defined by Eqs. (2·2)~(2·4). By making the multipole expansion of the r.h.s. of Eq. (B·4), the final expression with the GCM basis of Eq. (3·13) is obtained as

$$\langle[\Phi^{\alpha\alpha}(l_1;\,d_1)\times\varphi_{\lambda_1}(R;\,D_1)\,Y_{\lambda_1}(\hat{\boldsymbol{R}})]_L|\,V_{AN}|[\Phi^{\alpha\alpha}(l_2;\,d_2)\times\varphi_{\lambda_2}(R;\,D_2)\,Y_{\lambda_2}(\hat{\boldsymbol{R}})]_L\rangle$$

$$=16v_{AN}^0\Big(1+\frac{\mu}{\nu_{AN}}\Big)^{-3/2}(4\pi)^2\exp[-\alpha_1(D_1{}^2+D_2{}^2)-\alpha_2(d_1{}^2+d_2{}^2)]$$

$$\times(-)^{l_1+\lambda_1}\sum_{m=0}^{3}\binom{3}{m}(-)^{m+1}$$

$$\times \sum_{k_1 \sim k_6} (-)^{k_1 + \cdots + k_6} [k_1] \cdots [k_6] \mathcal{J}_{k_1}(\alpha_4(m) d_1 d_2) \mathcal{J}_{k_2}(\alpha_3 D_1 D_2) \mathcal{J}_{k_3}(\alpha_6 d_1 D_2)$$

$$\times \mathcal{J}_{k_4}(\alpha_6 D_1 d_2) \mathcal{J}_{k_5}(\alpha_5 d_1 D_1) \mathcal{J}_{k_6}(\alpha_5 d_2 D_2)$$

$$\times \sum_{K_1 \sim K_4} \sqrt{[K_1] \cdots [K_4]} \, C_1(K_1 \cdots K_4, \, k_5 k_6, \, l_1 \lambda_1 l_2 \lambda_2 L) C_2(K_1 \cdots K_4, \, k_1 \cdots k_4, \, L) , \qquad \text{(B·9)}$$

where the C_1 and C_2 coefficients are defined by

$$C_1(K_1 \cdots K_4, \, k_5 k_6, \, l_1 \lambda_1 l_2 \lambda_2 L) = W(K_1 K_2 l_1 \lambda_1; \, L k_5) W(K_3 K_4 l_2 \lambda_2; \, L k_6)$$

$$\times (k_5 0 K_1 0 | l_1 0)(k_5 0 K_2 0 | \lambda_1 0)(k_6 0 K_3 0 | l_2 0)(k_6 0 K_4 0 | \lambda_2 0) , \qquad \text{(B·10)}$$

$$C_2(K_1 \cdots K_4, \, k_1 \cdots k_4, \, L)$$

$$= (k_1 0 k_2 0 | K_1 0)(k_2 0 k_4 0 | K_2 0)(k_1 0 k_4 0 | K_3 0)(k_3 0 k_2 0 | K_4 0) \begin{pmatrix} k_1 & k_3 & K_1 \\ k_4 & k_2 & K_2 \\ K_3 & K_4 & L \end{pmatrix} . \qquad \text{(B·11)}$$

The double signs in α_3, $\alpha_4(m)$ and α_6 mean the direct (upper) or exchange (lower) case.

Appendix C

——*The Matrix Elements of $F_K^{(s)}$ and $F_K^{(p)}$ in § 5*——

The initial hypernuclear wave function $\Psi(^A_\Lambda Z; J_i T_i \tau_i)$ and the final nuclear wf $\Psi(^A Z'; J_f T_f \tau_f)$ used in Eq. (5·10) are represented by Eqs. (2·18) and (2·35), respectively. The matrix elements involved in the π-mesic decay rate are expressed as follows ($A = 4 + x + 1$):

$$\sqrt{4+x+1} \langle \Psi(^A Z'; J_f T_f \tau_f) \| F_K^{(s)} \theta_\pi \| \Psi(^A_\Lambda Z; J_i T_i \tau_i) \rangle$$

$$= s_\pi \sum_{N_f} a_{N_f}^{(L_f J_f)} \sum_{c_i N_i K_i} A_{c_i}(N_i K_i) \sum_{K_1 \lambda_1} \mu^\pi(N_f L_f T_f \tau_f S_f; \, [N_i l_i K_1 \lambda_1]_{N_f L_f} T_x \tau_x [S_x \times \tfrac{1}{2}]_{S_f})$$

$$\times \delta(S_i, \, S_f) \sqrt{[L_f][J_f][L_i][J_i]} \, W(J_i K S_f L_f; \, J_f L_i) W(\lambda_1 K l_i L_f; \, \lambda_1 L_i)$$

$$\times \langle u_{K_1 \lambda_1}(R_1) \| j_K(qx) \| u_{K_i \lambda_i}(R_\Lambda) \rangle \langle Y_{\lambda_1} \| Y_K \| Y_{\lambda_i} \rangle , \qquad \text{(C·1)}$$

$$N_f = 2n_f + l_f, \quad c_i \equiv \{l_i \lambda_i L_i S_i\},$$

$$N_i = 2n_i + l_i, \quad K_i = 2\nu_i + \lambda_i, \quad K_1 = 2\nu_1 + \lambda_1 = N_f - N_i ,$$

$$\sqrt{4+x+1} \langle \Psi(^A Z'; J_f T_f \tau_f) \| F_K^{(p)} \theta_\pi \| \Psi(^A_\Lambda Z; J_i T_i \tau_i) \rangle$$

$$= (-i) p_\pi \left(\frac{q}{q_0} \right) \sum_{k=K\pm 1} (10K0|k0)(k-K) \sum_{N_f} a_{N_f}^{(L_f J_f)}$$

$$\times \sum_{c_i N_i K_i} A_{c_i}(N_i K_i) \sum_{K_1 \lambda_1} \mu^\pi(N_f L_f T_f \tau_f S_f; \, [N_i l_i K_1 \lambda_1]_{N_f L_f} T_x \tau_x [S_x \times \tfrac{1}{2}]_{S_f})$$

$$\times \sqrt{[L_f][S_f][J_f][K][L_i][S_i]} \begin{pmatrix} L_f & S_f & J_f \\ L_i & S_i & J_i \\ k & 1 & K \end{pmatrix} W(S_x \tfrac{1}{2} S_f 1; \, S_i \tfrac{1}{2}) \langle \tfrac{1}{2} \| \sigma \| \tfrac{1}{2} \rangle$$

$$\times W(l_i\lambda_i L_f k; L_i\lambda_1)\langle u_{K_1\lambda_1}(R_1)\|j_k(qx)\|u_{K_i\lambda_i}(R_\Lambda)\rangle\langle Y_{\lambda_1}\|Y_k\|Y_{\lambda_i}\rangle. \tag{C·2}$$

Here the coefficient μ^π is defined by Eqs. (2·36) and (2·37),

$$\mu^\pi = \Omega_x(N_fL_f; N_il_i, K_1\lambda_1)\omega_x{}^\pi(T_f\tau_fS_f; T_x\tau_xS_x). \tag{C·3}$$

References

1) W. Brückner et al. (Heidelberg-Saclay-Strasbourg Collaboration), Phys. Lett. **55B** (1975), 107; **62B** (1976), 481; **79B** (1978), 157.
2) R. Bertini et al. (H-S-S Collaboration), Phys. Lett. **83B** (1979), 306; **90B** (1980), 375.
3) R. Bertini et al. (H-S-S Collaboration), Nucl. Phys. **A360** (1981), 315.
4) R. Bertini et al. (H-S-S Collaboration), Nucl. Phys. **A368** (1981), 365.
   W. Brückner et al., *Proc. Kaon Factory Workshop*, ed. M. K. Craddock (Triumf, Vancouver, 1979), p. 124.
5) B. Povh, Rep. Prog. Phys. **39** (1976), 824; Ann. Rev. Nucl. Part. Sci., eds. J. D. Jackson et al. (1978, Annual Reviews Inc., Palo Alto), p. 1; J. Phys. Soc. Jpn. **44** (1978), Suppl. p. 775; Nucl. Phys. **A335** (1980), 233.
6) B. Povh, Prog. Part. Nucl. Phys. **5** (1981), 245.
7) M. Bedjidian et al. (CERN-Lyon-Warsaw Collaboration), Phys. Lett. **94B** (1980),480.
8) R. E. Chrien, M. May, H. Palevsky, R. Sutter, P. Barnes, S. Dytman, D. Marlow, F. Takeuchi, M. Deutch, R. Cester, S. Bart, E. Hungerford, T. M. Williams, L. S. Pinsky, B. W. Mayes and R. L. Stears, Phys. Lett. **89B** (1979), 31.
9) M. May et al., Phys. Rev. Lett. **47** (1981),1106.
10a) M. May, *Proc. Inter. Conf. on Hypernuclear and Kaon Physics* (Heidelberg, 1982), ed. B. Povh, p. 63.
   H. Piekarz, ibid, p. 73.
  b) M. May et al., Phys. Rev. Lett. **51** (1983), 2085.
11) T. Yamazaki and T. Ishikawa, *Proc. Workshop Hypernuclear Physics* (KEK, 1982), p. 66.
   T. Yamazaki, T. Ishikawa, K. Yazaki and A. Matsuyama, Phys. Lett. **144B** (1984), 177.
   T. Yamazaki et al., Phys. Rev. Lett. **54** (1985), 102.
12) D. H. Davis and J. Sacton, in *High Energy Physics*, Vol. II, ed. E. H. S. Burhop (1967, Academic Press), p. 365.
13) *Proc. Inter. Conf. on Hypernuclear and Kaon Physics* (Heidelberg, 1982), ed. B. Povh.
   Proc. Third LAMPF II Workshop, Los Alamos National Laboratory (1983), eds. J. C. Allred, T. S. Bhartia, K. Ruminer and B. Talley.
14) A. Gal, J. M. Soper and R. H. Dalitz, Ann. of Phys. **63** (1971), 53; **72** (1972), 445; **113** (1978), 79.
15) J. Hüfner, S. Y. Lee and H. A. Weidenmuller, Nucl. Phys. **A234** (1974), 429; Phys. Lett. **49B** (1974), 409.
16) A. Bouyssy, Nucl. Phys. **A290** (1977), 324.
17) A. Gal, *Advances in Nucl. Phys.*, eds. M. Baranger and E. Vogt, Vol. 8 (1975, Plenum, New York), p. 1.
18) R. H. Dalitz and A. Gal, Ann. of Phys. **116** (1978), 167.
19) R. H. Dalitz and A. Gal, Phys. Rev. Lett. **36** (1976), 362; Ann. of Phys. **131** (1981), 314.
20) R. H. Dalitz, *Proc. Int. Conf. Nuclear Structure* (1980, Berkeley), Nucl. Phys. **A354** (1981), 101c.
21) H. Bandō, M. Seki and Y. Shono, Prog. Theor. Phys. **66** (1981), 2118; **68** (1982), 364 Errata.
22) H. Bandō, INS-PT-31 (1982), INS, University of Tokyo; Chapter I of this issue;
   Proc. Inter. Summer School on Nucleon-Nucleon Interaction and Nuclear Many-Body Problems (1982, Changchun, China), eds. S. S. Wu and T. T. S. Kuo (1984, World Scientific Pub.), p. 262.
23) T. Motoba, H. Bandō and K. Ikeda, Prog. Theor. Phys. **79** (1983), 189; **81** (1984), 222; *Proc. Inter. Conf. on Hypernuclear and Kaon Physics* (Heidelberg, 1982), ed. B. Povh, p. 129; *Proc. Inter. Symp. Electromagnetic Properties of Atomic Nuclei*, Tokyo Institute of Technology, eds. H. Horie and T. Oda (1984), p. 482.
24) C. B. Dover, L. Ludeking and G. E. Walker, Phys. Rev. **C22** (1980), 2073.
   C. B. Dover, *Proc. 9th Int. Conf. High Energy Physics and Nuclear Structure* (1981, Varsailles), Nucl. Phys. **A374** (1982), 359c.
   C. B. Dover and G. E. Walker, Phys. Rep. **89**, No. 1 (1982), 1.
25a) E. H. Auerbach, A. J. Baltz, C. B. Dover, A. Gal, S. H. Kahana, L. Ludeking and D. J. Millener, Phys. Rev. Lett. **47** (1981), 1110; Ann. of Phys. **148** (1983), 381.
  b) D. J. Millener, A. Gal, C. B. Dover and R. H. Dalitz, Preprint BNL-35309 (1984).
26) K. Ikeda et al., Prog. Theor. Phys. Suppl. No. 52 (1972); No, 68 (1980).

27) For example, *Proc. Int. Conf. Clustering Aspects of Nuclear Structure and Nuclear Reactions* (Winnipeg, 1978) ed. W. T. H. Van Oers et al. (AIP Conf. Proc. No. 47).

28) L. Majling, M. Sotona, J. Zofka, V. N. Fetisov and R. A. Eramzhyan, Phys. Lett. **92B** (1980), 256.
J. Zofka et al., *Proc. Inter. Conf. on Hypernuclear and Kaon Physics* (Heidelberg, 1982), ed. B. Povh, p. 85, p. 91.
L. Majling, J. Zofka, V. N. Fetisov and R. A. Eramzhyan, Phys. Lett. **130B** (1983), 235; Preprint No. 66, P. N. Lebedev Physical Institute, Moscow (1983).

29) J. Revai and J. Zofka, Phys. Lett. **101B** (1981), 228.

30) Zhang Zong-ye, Li Guang-lie and Shen Jian-ping, Transactions of the New York Academy of Sciences **II-40** (1980), 274.
Zhang Zong-ye, Li Guang-lie and Yu You-wen, Phys. Lett. **108B** (1982), 261.

31) A. R. Bodmer and Q. N. Usumani and J. Carlson, Nucl. Phys. **A422** (1984), 510; Phys. Rev. **C29** (1984), 684.

32) R. H. Dalitz and G. Rajasekaran, Nucl. Phys. **50** (1964), 450.

33) A. R. Bodmer and S. Ali, Nucl. Phys. **56** (1964), 657.
A. R. Bodmer and J. W. Murphy, Nucl. Phys. **64** (1965), 593; **73** (1965), 664.

34) Y. C. Tang and R. C. Herndon, Phys. Rev. **138** (1965), B637; Nuovo Cim. **66** (1966), 117.

35) H. Bandō, K. Ikeda and T. Motoba, Prog. Theor. Phys. **69** (1983), 918.

36) D. Helderson, Phys. Rev. **C30** (1984), 941.

37) M. M. Nagels, T. A. Rijken and J. J. de Swart, Phys. Rev. **D12** (1975), 744; **D15** (1977), 2547; **D20** (1979), 1633.

38) Y. Yamamoto and H. Bandō, Chapter II of this issue.

39) D. L. Hill and J. A. Wheeler, Phys. Rev. **89** (1953), 1106.
J. J. Griffin and J. A. Wheeler, Phys. Rev **108** (1957), 311.
H. Horiuchi, Prog. Theor. Phys. Suppl. No. 62 (1977), 90.

40) S. Saito, Prog, Theor. Phys. Suppl. No. 62 (1977), 11.

41) S. Saito, Prog. Theor. Phys. **40** (1968), 893; **41** (1969), 705.

42) H. Nishioka, S. Saito and M. Yasuno, Prog. Theor. Phys. **62** (1979), 424.

43) The compilations quoted in Ref. 17).

44) F. Ajzenberg-Selove, Nucl. Phys. **A413** (1984), 1 and references cited therein.
Table of Isotopes, eds C. M. Lederer and V.S. Shirley (Wiley-Interscience)

45) R. H. Dalitz and A. Gal, Phys. Lett. **64B** (1976), 154.

46) A. Bouyssy, Phys. Lett. **84B** (1979), 41; **99B** (1981), 373.

47) S. Okabe, Y. Abe and H. Tanaka, Prog. Theor. Phys. **57** (1977), 866.

48) G. P. Gopal et al., Nucl. Phys. **B119** (1977), 362.

49) For example, N. K. Glendenning, Phys. Rev. **137** (1965), B102.
H. Horiuchi, K. Ikeda and Y. Suzuki, Prog. Theor. Phys. Suppl. No. 52 (1972), Chapter III, p. 89.

50) K. Ikeda, H. Bandō and T. Motoba, Chapter V of this issue.

51) Y. Kurihara, Y. Akaishi and H. Tanaka, Prog. Theor. Phys. **71** (1984), 561.

52) R. H. Dalitz, *Proc. Inter. Conf. Hyperfragments* (St. Cergue, 1964), CERN Report 64-1, p. 147.

53) H. Bandō and H. Takaki, Prog. Theor. Phys. **72** (1984), 106; Phys. Lett., to be published.

54) R. H. Dalitz, Phys. Rev. **112** (1958), 605.
R. H. Dalitz and L. Liu, Phys. Rev. **116** (1959), 1312.

55) See §§ 3 and 4 of this chapter.

56) Y. Mito and M. Kamimura, Prog. Theor. Phys. **56** (1970), 583.
M. Kamimura, Prog. Theor. Phys. Suppl. No. 62 (1977), 236.

57) T. Yamada, K. Ikeda, H. Bandō and T. Motoba, Prog. Theor. Phys. **73** (1985), 397.

58) A. B. Volkov. Nucl. Phys. **74** (1965), 33.

59) J. Hiura and R. Tamagaki, Prog. Theor. Phys. Suppl. No. 52 (1972), 25.

60) T. Yamada, K. Ikeda, H. Bandō and T. Motoba, to be submitted.

61) D. M. Brink, *Proc. Int. School of Physics "Enrico Fermi" 1965,* Course XXXVI, ed. C. Bloch (Academic Press, 1966), p. 247.